2007

Discrimination Of Forensic Trace Evidence Using Laser Induced Breakdown Spectroscopy

Candice Bridge
University of Central Florida

DISCRIMINATION OF FORENSIC TRACE EVIDENCE USING LASER INDUCED BREAKDOWN SPECTROSCOPY

by

CANDICE MAE BRIDGE
B.S. Howard University, 2004

A dissertation submitted in partial fulfillment of the requirements
for the degree of Doctor of Philosophy
in the Department of Chemistry
in the College of Sciences
at the University of Central Florida
Orlando, Florida

Fall Term
2007

Major Advisor: Michael E. Sigman

ABSTRACT

Elemental analysis in forensic laboratories can be tedious and many trace evidence items are not analyzed to determine their elemental composition. Presently, scanning electron microscopy-energy dispersive x-ray spectroscopy (SEM-EDS) is the primary analytical tool for determining the elemental composition of trace evidence items. However, due to the time it takes to obtain the required vacuum and the limited number of samples that can be analyzed at any one time, SEM-EDS can be impractical for a high volume of evidence items. An alternative instrument that can be used for this type of analysis is laser ablation inductively coupled plasma mass spectrometry (LA-ICP-MS). While LA-ICP-MS is a very precise and quantitative analytical method that determines elemental composition based on isotopic mass measurements; however, the instrumentation is relatively expensive and therefore is budgetarily prohibitive for many forensic laboratories. It is the purpose of this research to evaluate an inexpensive instrument that can potentially provide rapid elemental analysis for many forensic laboratories. Laser induced breakdown spectroscopy (LIBS) is an analytical method that meets these requirements and offers information about the elemental composition based on ionic, atomic and diatomic molecular emissions.

ACKNOWLEDGMENTS

To my Mommy and Daddy, I want to thank you so much for you guidance that kept me focused and grounded while pursuing this path in my life. I would like to dedicate this dissertation to the two of you. To my Auntie Janet, Auntie Mavis, Auntie Betty and my Uncle Earl, thanks for your spiritual words that also kept me grounded. I would also to extend my gratitude to my other aunties and uncles, my brother, my sister, cousins, extended family and best friends. There are way too many to name individually, but you know who you are; your support was always appreciated. Thank you so much for the encouraging words. Lest I forget my late uncle/god-father, Kenneth Bridges; whose memory was with me while I wrote this dissertation. You will never be forgotten. I miss you.

I would like to express my thanks to my committee members for their expertise and assistance with writing this dissertation. I would especially like to thank my committee chair and research advisor, Dr. Sigman, for all of his guidance and encouraging words throughout my graduate studies. As for my fellow graduate students and National Center of Forensic Science (NCFS) co-workers, of which there are too many to name, I appreciate all of the great experiences we had at UCF. However, there are two individuals in particular that I need to express my gratitude. To Stephan, thanks for the wonderful friendship that we have formed and all the late night studying. To Katie, thanks for all of the laughs and trips into the "black and white" world that you lead.

I love you all. God bless and keep you.

TABLE OF CONTENTS

LIST OF FIGURES

LIST OF TABLES

CHAPTER ONE:
INTRODUCTION

Laser induced breakdown spectroscopy (LIBS) is a fast method of elemental analysis that has recently become a valuable analytical instrument in research laboratories. Determination of a sample's elemental composition is obtained through laser ablation followed by atomic, ionic and molecular emission. These emissions are recorded as a high resolution emission spectrum. LIBS is an analytical technique that provides good qualitative analysis through the use of elemental emission ratios. Quantitative analysis of the matrix elements has been achieved with LIBS and is presented in several publications.[1-6] Recent advances in instrumentation have produced commercially available LIBS spectrometers that are inexpensive compared to instrumentation required for inductively coupled plasma-atomic emission spectrometry (ICP-AES), inductively coupled plasma-mass spectrometry (ICP-MS) and laser ablation inductively coupled plasma-mass spectrometry (LA-ICP-MS). Characteristics of LIBS, including rapid analysis time, lack of required sample preparation, potential for field portability, and cost effectiveness, make this relatively non-destructive method of analysis very attractive for many analytical applications, including those in the forensic and security fields.

Elemental analysis is quite useful for glass trace evidence, in which refractive index (RI) has historically been the only information used for sample discrimination. By utilizing

elemental analysis, more information is available for discriminating between an unknown and a known sample. LA-ICP-MS can discriminate automobile side glass samples to nearly 100% due to its precise measurements. Similar discrimination can be attained from LIBS in combination with RI measurements, which may make it a cost-effective alternative for forensic laboratories.

Automobile paint analysis is another common type of trace evidence studied in this work. Paint samples generally have three to four layers. The first layer, a clear coat layer, is comprised of a polymer and presently the limited information that can be acquired from this layer is obtained by Fourier transform infrared spectrometry. While LIBS provides a wealth of information about the elemental composition of the sample via the atomic and ionic emission intensities; diatomic species emissions from polymeric layers can be observed as well. Based on the intensities from these diatomic emissions, more information about the polymeric layer can be attained. Due to the large amount of information obtained from LIBS spectra, it may be possible to identify a relationship between the LIBS spectra and the polymer structure.

In this study, the forensic application of LIBS is evaluated as a method for the analyses of glass (automobile float glass, automobile side mirror glass, automobile headlamp glass and brown container glass), automobile paint and trace levels of explosives and energetic materials. In each case, elemental composition can provide valuable discriminating information. Other discriminating analytical instrumentation, such as LA-

ICP-MS or XRF, are relatively more expensive than the smaller commercial LIBS instrument and hence are not widely available to many forensic laboratories. The objective of the research has been to determine if LIBS is of sufficient discriminating power to be useful in forensic investigations.

CHAPTER TWO:
BACKGROUND

LIBS is an analytical technique that is only now finding it's way out of the research laboratory with the aid of recently available commercial instruments. The accessibility of LIBS parallels advances in the use of elemental composition for the discrimination of glass and other trace evidence samples. LIBS has several potential advantages over conventional spectrochemical techniques, such as inductively coupled plasma-atomic emission spectrometry (ICP-AES), inductively coupled plasma-mass spectrometry (ICP-MS), and atomic absorption spectrometry (AA). Primary among these advantages are the lack of sample preparation required for LIBS and the small sample size required. These advantages are shared by laser ablation inductively coupled plasma mass spectrometry (LA-ICP-MS); however, the low cost and the field-portability of new LIBS instruments is not shared by LA-ICP-MS systems. LA-ICP-MS and LIBS both rely on ablation of a sample surface by the focused output of a laser, but are dissimilar in the manner in which the laser-induced plasma is utilized.

For LIBS, ablation occurs when a high power laser pulse (generally > 1-10 MW/cm^2) impinges on the surface of a solid sample, a plasma composed of elemental and molecular fragments from the sample's surface is produced.[7] As the plasma cools, the excited atoms emit light at characteristic wavelengths in the 200 – 900 nm spectral region. The emission lines are spectrally resolved and recorded, typically about 1

micro-second after the laser pulse, to give information on the elemental composition of the sample. Several reviews of recent developments in the field of LIBS research address the multitude of applications for which this technique has been used, from trace levels of explosives to bacterial spores to human tissue.[8-15]

Despite its many advantages, applications of LIBS have been hindered by several limitations, including a high background continuum, line-broadening, and self-absorption of the peaks.[9] These limitations may be minimized to some extent through variations in the experimental geometry, time-resolved data collection and sampling in an inert atmosphere.[9] In addition, Kuzuya et al. have shown that background noise can often be reduced by collecting the LIBS data under an inert atmosphere and at reduced pressure.[16] The precision of the data was not addressed by Kuzuya, but shot-to-shot laser fluctuations (typically 1 – 5%) were known to lead to experimental variations in atomic emission intensity. Optimizing the precision of the LIBS instrumental method is critical.

LIBS is best suited for qualitative analysis or the determination of relative element concentrations in a sample, rather than absolute concentration determination.[9] Absolute concentration determination is complicated by laser shot-to-shot variations and the interaction of the laser with the matrix, both physical and chemical.[17] Physical effects stem from how the matrix affects the amount of an element that is ablated. Chemical effects arise from how the presence of one element can affect the emission of

another element. The difficulties associated with determining the absolute concentration of elements in a glass sample by LIBS do not prohibit the use of this analytical technique for discrimination of trace evidence samples, since a comparison of samples from questioned and known origins requires only knowledge of the relative elemental concentrations or emission intensities associated with each sample.[18]

Quantitation of analyte concentrations using LIBS has many challenges but there are publications that report quantitative analysis with LIBS.[19] The ratios of spectral line intensities can be directly compared for questioned and known samples as a simple method of common source determination or sample discrimination. One factor that complicates the use of LIBS for quantitative analysis is that the line intensity ratios differ from the concentration ratios primarily due to differences in state-to-state transition probabilities and state populations (neutral and ionized) for each element. This phenomenon, referred to as fractionation, is a problem for other laser ablation techniques as well as for LIBS.[20] Recent work has also shown that the LIBS signal intensity is affected by the depth of the crater in the target matrix ("confinement effect").[21, 22]

In characterizing the type of plasma produced, it is important to know if the plasma is in thermodynamic equilibrium (TE), which requires the knowledge of the plasma temperature and its electron density. Concentration of the species located in the plasma can be determined from these parameters as well. The electron density,

plasma temperature and element concentration can be calculated from the spectral data with the aid of tabulated spectral constants for the elements.[23] Plasma temperatures are typically in the range of 6,000 K. Detection limits have been determined for few elements through quantitative analysis with LIBS. The lowest detection limit observed is as low as 0.22 ppm for Be with a precision of 8.2%.[5, 24]

CHAPTER THREE:
INSTRUMENTAL METHODS

Instrumentation Background

Laser induced breakdown spectroscopy is a relatively non-destructive, fast method of elemental analysis. During the creation of a LIBS plasma event a high intensity Neodymium: Yttrium Aluminum Garnet (Nd:YAG, 1064 nm) laser is focused on the surface and through dielectric breakdown all elements present in the sample are excited and subsequently emit light at unique wavelengths. The emitted light is collected by a bifurcated seven fiber optic cables, with each fiber optic connected to one of seven charge-couple device (CCD) spectrometers, thereby achieving a high resolution spectrum that spans 200 – 900 nm. The instrumentation can analyze solid, liquid and gaseous samples.

A second method of elemental analysis used in this research is laser ablation inductively coupled plasma mass spectrometry (LA-ICP-MS). LA-ICP-MS is a precise method of measuring the abundance of selected isotopes. A 213 nm laser is focused onto the sample's surface where it is absorbed by the glass. Particles of the sample's matrix are ablated into the vacuum and transported to the ICP-MS by an argon flow. In the inductively coupled plasma, these particles are ionized and atomized and the isotopes

are subsequently measured by a mass spectrometer. This technique is a destructive method; however, only a few milligrams of a sample are required for analysis.

Fourier transform infrared – attenuated total reflectance (FTIR-ATR) is another non-destructive method used for discrimination in this study. The surface layer of the sample is interrogated by infrared light through an ATR silicon crystal. The evanescent light is absorbed by molecular vibrations and then is reflected back through the crystal into the detector. There is little to no sample preparation necessary to use the ATR attachment for solid and/or liquid samples.

Another method of elemental analysis used in this study is x-ray fluorescence (XRF). This instrument measures the intensity of k-lines, l-lines and m-lines of fluorescence emitted from the "falling" of an electron in a higher orbital to fill a hole in a lower orbital left by an electron removed under x-ray irradiation. This method is non-destructive and generally gives good forensic discrimination. Little to no sample preparation is necessary for sampling with this instrument; however, if the sample is multi-layered or a mixture then separation needs to be achieved for individual component layer analysis. Otherwise, more than one component layer may be analyzed simultaneously.

Scanning electron microscopy – energy dispersive x-ray spectrometry (SEM-EDX) was used to not only obtain images of samples but to determine the elemental characterization of a sample in a manner similar to XRF. This technique is a destructive

method; however, samples do not need to be separated into its components due to the high magnification obtained by the SEM.

Laser Induced Breakdown Spectroscopy (LIBS)

The LIBS instrument used in this research was an Ocean Optics (Dunedin, Fl, USA), model LIBS2000+. This instrument was equipped with an Nd-YAG, 1064 nm wavelength, Q-switched, pulsed laser (Big Sky Lasers, model CFR200, Bozeman, Montana, USA), with a pulse width of 9 ns. Spectra reported here were collected with a laser output energy of 98 mJ/pulse, and the detector delay was adjusted depending on the sample. The glass samples were analyzed at a detector delay time of 15 μs and the paint and explosive samples were analyzed at a 2.5 μs detector delay time. The spectrometer gate time was fixed at 2 ms. The laser was focused onto the sample by a focusing lens with a focal length of 7.5 cm. The plasma-generated emission intensities (200 – 900 nm) were collected by a bifurcated seven fiber optic each connected to seven arrayed linear CCD spectrometers. The resolution in the first six spectrometers is approximately 0.51 Å/channel on average; whereas, the seventh spectrometer has a resolution of approximately 0.8 Å on average.

Laser Ablation Inductively Coupled Plasma Mass Spectrometer (LA-ICP-MS)

The LA-ICP-MS system used in this study was equipped with a laser ablation unit (New Wave Research/Mechantek Fremont, CA, USA) model LUV 213 and an ICP-MS (Agilent

Technologies, Palo Alto, CA, USA) model 7500s. The laser unit uses the 213-nm output of an Nd-YAG Q-switched laser (pulse width of 3-5 ns). The laser spot size is adjustable from 5 μm^2 to 400 μm^2. Maximum laser energy output of 3 mJ/pulse was used for ablation.

Glass Refractive Index Measurement (GRIM3)

The GRIM3 instrument (Foster and Freeman, Evesham, Worcestershire, UK) utilizes the refractive index-temperature variation method. The instrument uses a 589-nm lamp and Mettler hot stage to determine the refractive index of each glass sample.

X-Ray Micro-Fluorescence (XRMF)

An EDAX Eagle III microprobe was used for X-ray fluorescence analysis. The software used to perform the analysis was Vision 32. The samples were analyzed in a vacuum chamber. Glass samples were analyzed with a 100 μm spot size and the paint samples were analyzed with a 300 μm spot size. A Rhodium (Rh) anode x-ray tube was used for analysis measurement and was operated at an energy of 40 kV and the current (μA) was adjusted per sample to maintain a deadtime less than 40%. Counts per second (cps) were maintained at approximately 2000.

Scanning Electron Microscope – Energy Dispersive Spectrometer (SEM-EDX)

A scanning electron microscope (LEO 1450 VP, Thornwood, N.Y., USA) with variable pressure secondary electron detector and energy dispersive spectrometer operating at 30 kV (Oxford INCA software, High Wycombe, U.K.) were used for SEM-EDX analysis. Copper was used as an external standard for EDX calibration. This microscope operates with a tungsten lamp.

The second and third scanning electron microscopes used (JOEL JSM-5900LV and JOEL JSM-6490LV, Tokyo, Japan) were equipped with variable pressure secondary electron and backscatter electron detectors. Both microscopes were equipped with energy dispersive spectrometers operating at 25 kV (Oxford INCA software, High Wycombe, U.K.). Copper and cobalt were used as external standards for EDX calibration of each system. Calibration occurred between each sample analyzed. Both microscopes operate with tungsten lamps. Each sample was analyzed for a lifetime of 200 seconds and the deadtime was keep below 40%.

The signals used for capturing an image of the sample were secondary electron (SEI), backscatter electron – shadow (BES), backscatter electron – tempo (BET) and backscatter electron – compo (BEC). Secondary electron shows a representative picture of the sample itself; whereas, the BES and the BEC show a representation of

elemental differences within the sample (i.e. heavier elements appear lighter in the SEM image). The BET signal shows the topography of the sample's surface.

Fourier Transform Infrared – Attenuated Total Reflectance (FTIR-ATR)

An ATI Mattson Infinity Series FTIR in conjunction with a Spectratech Infrared (IR) Plan Advantage IR Microscope was used for ATR measurements. This instrument was operated in IR and reflective modes using a Si 207 crystal attachment.

CHAPTER FOUR:
DATA ANALYSIS

Analysis performed by the following methods was evaluated at three confidence levels: 90%, 95% and 99%. The calculation was performed at three confidence levels to determine how the type II errors varies and is affected by the confidence level. A type I error occurs when two samples are concluded to be from different sources when they are in fact from the same source (False Rejection). A type II error occurs when two samples are concluded to be from the same source when they are in fact of different sources (False Inclusion).[25] In the nature of forensic science, type II errors are of the major concern when comparing a known to an unknown sample. The significance level most commonly used for accessing the risk of error of an analytical method is α = 0.05 or 95% confidence; however, the α value can be modified to guard against the error with the highest social consequence. If a type I error is of more consequence then α can be set at either 0.01 (99%) or 0.001 (99.9%). However, if the type II error is of more consequence, then α can be either 0.05 (95%) or 0.10 (90%).[26]

ANOVA with a Tukey HSD Post Test

The initial method used to evaluate the discrimination capability of the LIBS instrument utilized an analysis of variance (ANOVA) test followed by a Tukey honestly significant difference (HSD) post test. The ANOVA test calculates an F-statistic value; in which

significant F-statistic values give an approximation of the discrimination capability of elemental ratios. The F value is the ratio of the variance between the different samples divided by the variance within a set of single sample measurements. In this approach the discriminating parameters are elemental emission ratios from LIBS, XRF or EDX spectra and the LA-ICP-MS discriminating ratios are based on isotopic abundance ratios.

The elemental ratios were further analyzed by a Pearson product moment correlation coefficient matrix to choose those ratios with the lowest correlation in order to maximize the information content provided by the ratios. To determine if the variables (emission line ratios, isotopic ratios and the RI values) used for the discrimination of the glass samples were linearly correlated, the Pearson product-moment correlation was calculated.[25] Two variables were deemed independent if the absolute value of the correlation coefficient (r) was less than the criteria $r < 0.8$. The Pearson correlation value is calculated by equation 1[27]:

$$r = \frac{\sum_i \{(x_i - \bar{x})(y_i - \bar{y})\}}{\{[\sum_i (x_i - \bar{x})^2][\sum_i (y_i - \bar{y})^2]\}^{1/2}} \quad \textbf{(1)}$$

This approached was followed by a Tukey honestly significant difference (HSD) post test to determine the overall discriminating power of the analytical methods. The Tukey HSD test was utilized to ensure that the probability of making a type I error was held at the specified level.[25] The ANOVA test followed by the Tukey HSD post test was

performed in SAS/STAT (SAS Institute Inc., Cary, NC, USA) and Microsoft Excel (Microsoft Corp., Redmond, WA, USA). The SAS/STAT software calculates the critical studentized range distribution (Q), which is used to determine if two samples are significantly different (equation 2). Two samples are considered significantly different if their mean difference is larger than the HSD interval.[28]

$$\left|Avg_1 - Avg_2\right| \geq \sqrt{\frac{MS_{wg}}{N}} * Q(\alpha, P, df) \quad \textbf{(2)}$$

The mean square of the error within the group (MS_{wg}) is divided by the number of measurements (N), the quotient is otherwise known as the standard mean of the error, Q (α, P, d.f.) is the critical studentized range distribution at the alpha percentage (α), for the number of samples (P) and the degrees of freedom within the sample set (d.f.). The total number of samples can be calculated as the number of samples (P) times the number of measurements (N).

The "discrimination percentage" for each elemental ratio was calculated as the fraction of the total number of pairwise comparisons (i.e. 23 samples yields 253 pairwise comparisons) that were "distinguishable". The overall determination of discrimination of the samples was based on either a specified number of emission or isotope ratios for the LIBS or the LA-ICP-MS data, respectively. Discrimination was performed in conjunction both with the RI data and without the RI data for the same sample set.

Student's t-Test

When comparing a known sample to an unknown sample, the primary goal is to determine if the two samples could have come from the same source, or the same population. To determine if the null hypothesis, that the samples come from the same source, can be accepted, 5 replicate analyses (i.e. LIBS spectra) are taken for the known and the unknown sample. The discriminating metric (Euclidean distance, Correlation, Sorenson, etc…) is calculated between the replicate analyses on each sample and between the analyses on the two samples (comparative analysis). The results of these comparisons are recorded in a matrix similar to the matrices illustrated below (Figure 1). The reproducibility of the analysis is measured from the replicate discrimination, which provides the precision of the analytical method.

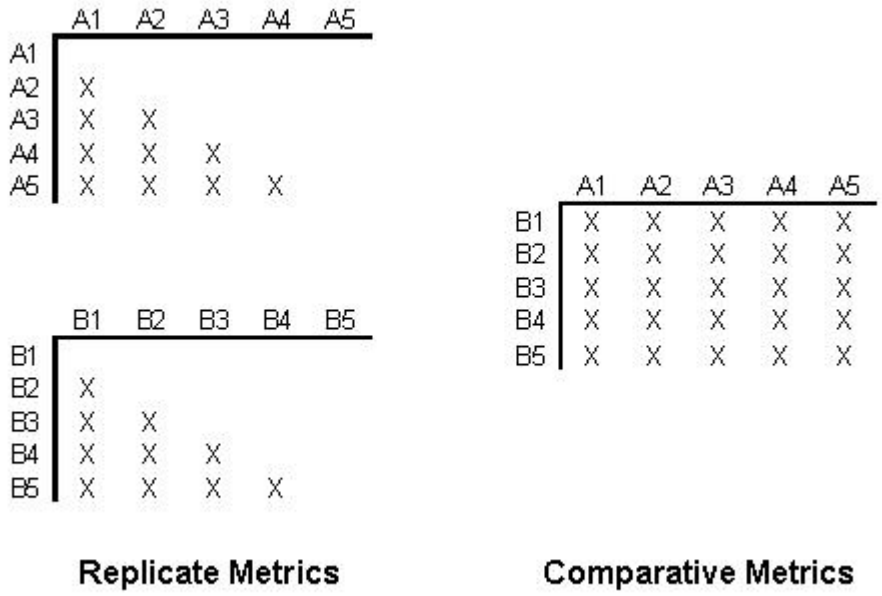

Figure 1: Matrices used to calculate the degrees of freedom and t' value for the *t*-test

The replicate metrics for the known and the unknown samples were consolidated to one average and standard deviation for total replicate metric, since both sets of values serve to establish the precision of the method. For direct comparisons between known and unknown samples, it is necessary to determine if the pair is significantly different. A student's t' value is calculated for each pairwise comparison to determine if the pair is from the same source or different sources. Since the number of measurements for the replicate distances and the comparative metrics are different with no guarantee of the same variance the appropriate calculation to determine t' is given below along with the equation for calculating the number of degrees of freedom (d.f.)[29]:

$$t' = \frac{\left|\overline{D}_{DS} - \overline{D}_{SS}\right|}{\sqrt{\frac{s_{DS}^2}{n_{DS}} + \frac{s_{SS}^2}{n_{SS}}}} \quad \textbf{(3)}$$

$$df = \frac{\left(\frac{s_{DS}^2}{n_{DS}} + \frac{s_{SS}^2}{n_{SS}}\right)^2}{\frac{\left(\frac{s_{DS}^2}{n_{DS}}\right)^2}{n_{DS}-1} + \frac{\left(\frac{s_{SS}^2}{n_{SS}}\right)^2}{n_{SS}-1}} \quad \textbf{(4)}$$

where s_{DS} is the standard deviation for the distances of the comparative measurements (different samples), s_{SS} is the standard deviation for the distances of the replicate measurements (same samples), n_{DS} and n_{SS} are the number of comparisons performed for the comparative and replicate samples, respectively. The $\overline{D}_{DS}$ and $\overline{D}_{SS}$ are the average metric values for the comparative and replicate measurements. Once the d.f.

and the t' values are calculated, the critical t value (t_{crit}) can be referenced at a specified confidence level. If $t' > t_{crit}$ then the null hypothesis can be rejected and the two samples are deemed to be from different sources.

Principal Component Analysis

Principal component analysis (PCA) is a technique used to reduce the dimensionality of a data set by representing the data as a smaller number of variables, otherwise known as the principal components. The principal components are identified such that principal component one contains the largest fraction of the variance in the data set, with each successive principal component representing progressively smaller percentages of the variance. The variance of each principal component is generally presented in a scree plot (Figure 2). Where there is a break in the curve signifies which principal components are required to reproduce the data with minimal error. Sample spectra can then be clustered into groups based on similar contributions from the principal components. The first two components frequently encompass a significant portion of the variance, often greater than 90%.[27, 30]

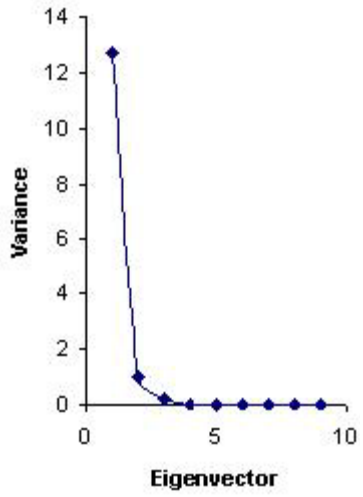

Figure 2: An illustration of a general scree plot

Linear Correlation

Spectra analyzed by linear correlation were normalized to the most intense peak in the spectrum and averaged over 5 replicate spectra. Each replicate spectra was comprised of an averaged of 10 single shot spectra. To normalize the spectra to the most intense peak, each point in the spectra was subjected to the following equation. Where the minimum point of the spectra is subtracted from each point in the spectra and then this value is then divided by the most intense peak subtracted by the minimum peak intensity. This equation is performed on each point in the spectra to normalize the whole spectra from 0 to 1.

$$I_{N,X} = \frac{I_x - I_{\min}}{I_{\max} - I_{\min}} \quad \textbf{(5)}$$

Peak Identification

Peaks present in LIBS spectra with a signal to noise (S:N) ratio greater than 3 were identified by a simple algorithm developed by Coombes et al.[31] This algorithm was based on initially determining the local minima and the local maxima in the whole spectrum to calculate to noise which is the difference between the median values of the maxima and the minima peaks. Then all of the local maxima with a difference from the local minima less than noise are removed from the spectra. Local maxima which are separated by 0.06 nm are then combined, only the highest local maximum is retained as a peak.

Product-Moment Correlation Coefficient

The product-moment correlation coefficient, otherwise known as the Pearson correlation, is a measure of how linear a set of data points.[27]

$$r = \frac{\sum_i \left\{ \left(x_i - \bar{x}\right)\left(y_i - \bar{y}\right) \right\}}{\left\{ \left[\sum_i \left(x_i - \bar{x}\right)^2 \right] \left[\sum_i \left(y_i - \bar{y}\right)^2 \right] \right\}^{1/2}} \qquad \textbf{(6)}$$

The Pearson correlation value was calculated for all of the same sample comparisons and for all of the different sample comparisons. By using the t' and the d.f., calculated from equations 3 and 4, in conjunction with the average Pearson correlation coefficients, it can be determined if the two samples are from the same source or different sources.

Rank Correlation

Rank correlation is another form of linear correlation; however, this method differs because the sample population does not need to be normally distributed in order to determine a relationship between two spectra.[26, 27] This method initially ranks the spectral peak intensities in each spectrum from low to high. The rank correlation method is applied to all identified peaks in the spectrum which meet a specified criterion. In this study, all peaks with a signal-to-noise (S:N) ratio greater than 3:1 were used. The peaks are then given a number from 1 to n, where n is the total number of peaks in each spectrum. The assigned numbers are plotted against each other and the correlation coefficient (r) is calculated. The correlation coefficient is calculated for each pairwise comparison both within the same sample and between the different samples, as described previously, to determine if the two samples can be discriminated using the *t*-test.

Confidence Intervals

Based on previous research of Koons and Buscaglia, it is imperative to determine how type I and type II errors are affected when performing statistical analyses.[25] There is an inverse relationship between these two errors; therefore, when the type I error percentage decreases the type II error percentage increases. The Student's *t*-test was used to calculate confidence intervals for peaks present in both spectra.[25]

The overall type I error rate is approximately n x α; where n is the number of variables. If α = 0.05, there is a 5% chance of a type I error. Therefore, using another variable for further discrimination can add up to an additional 5% chance of type I error. In order to control the type I error, the Bonferroni correction is used where the individual α' level for each variable is equal to α/n, where α is the overall type I error desired. However, by lowering the α level to minimize the type I error, the probability of having a type II error increases. In addition to decreasing α' to minimize the type I error, reducing the number of variables used will also reduce this type of error only if α' is held constant. Based on this information, it should be determined which error is of greater consequence: using too many variables and increasing the probability of making a type I error or using too few variables and limiting the discriminating power of the method and making a type II error.[25]

Ten variables were chosen for each direct comparison. In identifying peaks for this method, peaks had to be present in at least 4 out of 5 spectra obtained from the same sample at a signal to noise (S:N) ratio greater than 3:1. Peaks used for discrimination had to be present in both the questioned and known samples. The confidence interval for each peak present in the spectra was calculated from the average intensity ($\overline{X}$) and standard deviation (s) at the α' level, refer to equation 7.

$$\overline{X} \pm t_{n-1} \frac{s}{\sqrt{n}} \qquad \textbf{(7)}$$

If the absolute difference, $\left|\overline{X}_A - \overline{X}_B\right|$, is less than the sum of the confidence intervals for the two peaks, the two samples can not be discriminated; whereas, if the absolute difference exceeds the sum of the confidence interval, the two samples can be discriminated by this peak.

Receiver Operating Characteristic (ROC) Plots

The ROC plot evaluates the sensitivity and the 1-specificity of a sequence comparison by plotting the true positive fraction (sensitivity) vs. the true negative fraction (1-specificity). This determines the effectiveness of metric values used when comparing and retrieving data from a library, i.e. does the searched spectra correctly retrieve the library spectra from the same source. Each data point used in the comparison is initially classified as either a true positive value or a true negative value. A true positive value is the metric value calculated between a correctly identified pairwise comparison (same sample). A true negative value is the metric value calculated between an incorrectly identified pairwise comparison (different samples). These data points are then ranked in order from lowest to highest based on the HQI values (refer to Figure 3). The weight of each true positive fraction is calculated by taking the inverse of the total number of positive HQI values and the same is true to calculate the weight of the true negative fraction. The ROC plot is then created by plotting the fraction value for the lowest value whether of the negative or positive fraction and then the next lowest value. The area under the curve determines how probable it is that a value from the

positive group will be chosen before a value from the negative group. For an optimal sequence, all of the metric values from the same sample comparison would have a lower value and subsequently plotted before the metric values of the different sample comparisons (Figure 3).[32] As the area under the curve approaches 1, the more probable it is that a true fraction value will be chosen before a negative fraction value. If the area approaches 0.5, the sequence set is considered to a random event. Examples of creating ROC plots are given in Figure 3.

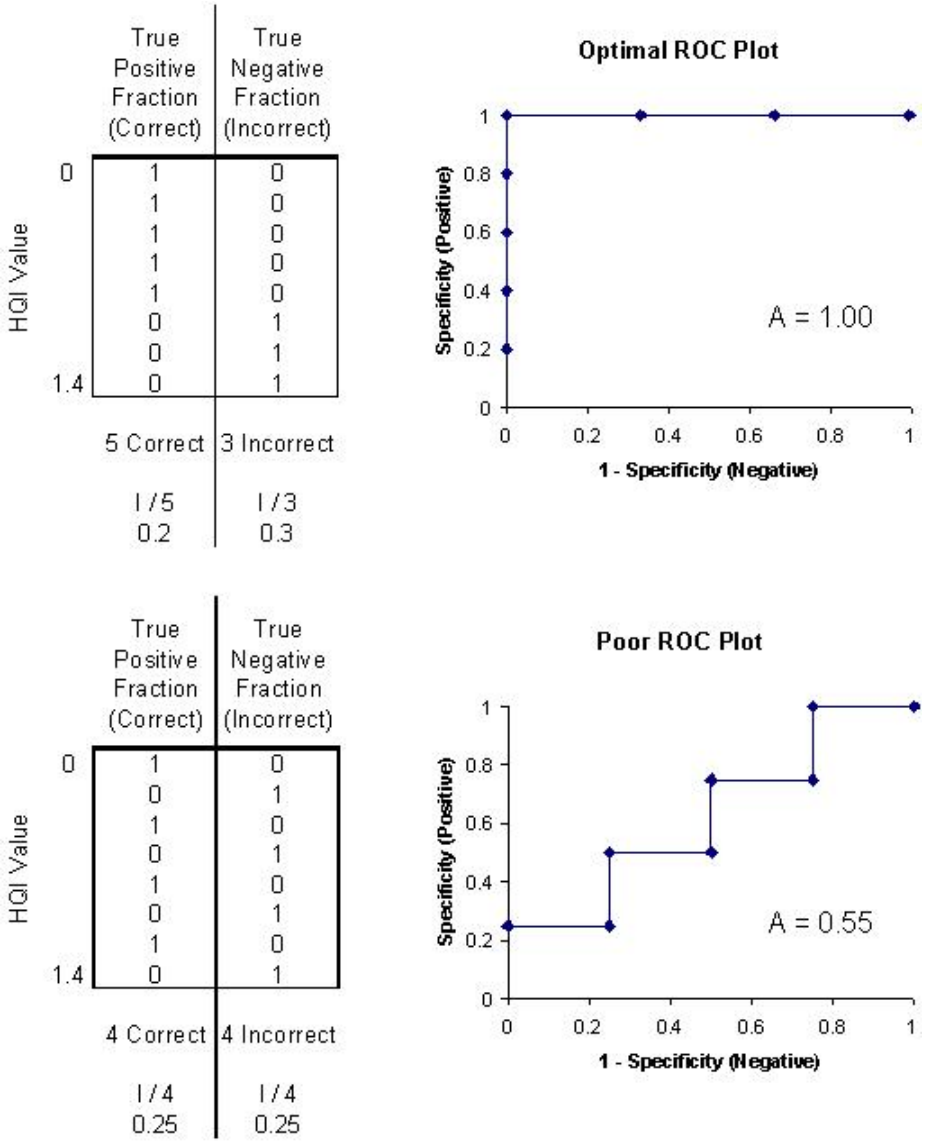

Figure 3: Illustrations of an ideal ROC curve and one based on randomness

CHAPTER FIVE:
CHARACTERIZATION OF A LIBS PLASMA

Physics of a Laser Induced Plasma

Laser induced plasmas are spatially inhomogeneous during the early states of the plasma generation. As the plasma evolves in time it moves towards a state of equilibrium. In addition to the measure of inhomogeneity of the plasma, shot-to-shot fluctuations of the laser also generate plasmas that are different from the one previous, which affects the resultant spectra. Characterization of the induced plasma is imperative in understanding the state of the plasma generated and subsequently the spectra produced.

Local Thermodynamic Equilibrium

The assumption of local thermodynamic equilibrium (LTE) is generally made for plasmas prepared in the laboratory. LTE can be expected when the energy absorbed by a molecule is distributed equally to other molecules through collisional processes, such as collisional excitation and de-excitation, before radiation is emitted or recombination of electrons occur.[33-35] This type of equilibrium can also be expected if the velocity distribution of the colliding particles are thermal so that steady state solution can be obtained for the rate equations.[33] LTE depends mainly on the electron density of the plasma; therefore, a minimum electron density needs to be acquired for LTE to exist.[33,

[35] The electron density lower limit is given by equation 8, where ΔE is the largest energy transition for which the condition holds for the electron temperature (T_e).[17, 23, 35, 36]

$$N_e\left(cm^{-3}\right) >> 1.6x10^{18}\sqrt{T_e\left[\Delta E\left(eV\right)\right]^3} \quad \textbf{(8)}$$

Plasmas with electron densities > ~ 10^{18} are difficult to produce and do not provide much information due to overlapping of spectral lines such that line broadening parameters, oscillator strengths and continuous absorption coefficients can not be obtained.[33] To a lesser extent, LTE is based on the electron temperature, atomic and ionic cross sections and their transition probabilities.[33]

A plasma is assumed to be at thermodynamic equilibrium (TE) if the Maxwell velocity distribution function (equation 9)[37], the Boltzmann population distribution (equation 10)[37-40], Saha-Eggert ionization-recombination relation (equation 11)[40-43], Planks radiation law (equation 12)[37, 44] and any other process that is based on temperature can be described by a single temperature for all species in the plasma. When the Plank's function is not valid and the plasma satisfies the equations 10 – 12 and other relations that at any spatial point and at any point in time, then the plasma is considered to be at LTE.[45, 46] Some equations that can be used to evaluate thermodynamic equilibrium are provided below.

The Maxwell velocity distribution function:

$$f(v) = 4\pi\left(\frac{m}{2\pi kT}\right)^{3/2} v^2 e^{\left[\frac{-mv^2}{2kT}\right]} \qquad \textbf{(9)}$$

$$v = \sqrt{v_x^2 + v_y^2 + v_z^2}$$

where m is the molar mass of the molecules, k is the Boltzmann constant, T is the temperature of the system, and v is the speed of the molecules in the system.

The Boltzmann population distribution:

$$\frac{N_i}{N} = \frac{g_i e^{-E_i/kT}}{\sum_i g_i e^{-E_i/kT}} \qquad \textbf{(10)}$$

where N_i is the population density of the excited species i, g_i is the statistical weight of species i, T is the temperature of the system, E_i is the energy of state i and N is the total number of species i in the system. The denominator represents the internal partition function of the species i at temperature, T.

The Saha-Eggert ionization-recombination relation:

$$g_x = \frac{(2mkT_i\pi)^{3/2}}{n_e h^3} \frac{2Z_x^+}{Z_x} e^{-\varphi_x/kT_H} \qquad \textbf{(11)}$$

where n_e is the electron density, m is the electron mass, φ_x is the ionization potential of an atom of element X, T_i is the ionization temperature, h is the Planck's constant, and Z_x^+ and Z_x are the partition functions of the ion and the atoms.

Planks radiation law is:

$$dE = \frac{8\pi hc}{\lambda^5\left(e^{hc/\lambda kT} - 1\right)} \quad \textbf{(12)}$$

where λ is the wavelength of the emitted photons, c is the speed of light and the other terms have been explained previously.

LIBS Plasma Event

A LIBS event is comprised of a four part mechanism: ablation of the sample's mass, breakdown of the sample's mass, plasma formation and elemental emission. This process begins when the pulsed laser's energy is focused onto a small sample area. Typically a nanosecond pulsed laser is used, as was used in this study; however, pico- and femto-second lasers have be used to perform LIBS experiments.[47-49] If the power density of the pulsed laser is higher than the dielectric breakdown threshold value of the sample, the sample's mass breaks down and the particulate matter vaporizes.[7] The laser pulse continues to permeate the vapor plume and the matter absorbs some of the laser's energy and scatters the rest of the energy. This scattering leads to ionization of the particulate matter and creation of a plasma. Plasma expansion occurs from ns – μs after the initial laser pulse. During these early stages of plasma formation, the electron density and plasma temperature is high.[17, 35, 50] Ion-electron interactions occur during this period, these interactions (recombination and bremsstrahlung) lead to broadband continuum emissions of the plasma, which needs to be removed from the spectrum usually through time-resolved spectroscopy or a spectrometer gate delay. This gate

delay can be manually adjusted to open the spectrometer gate after the continuum emissions have ceased. Following plasma expansion is radiative cooling of the plasma, which occurs from 1 μs – 0.1 ms. Radiative cooling leads to radiative emission of narrow atomic or ionic species as well as diatomic (molecular) band transitions. Plume condensation can leave a residue of coagulated particles on the sample's surface after radiative cooling.[51-53] Figure 4 shows residual particles left after a LIBS plasma event. Also evident from this figure are impressions from the shockwave caused by the induced plasma.

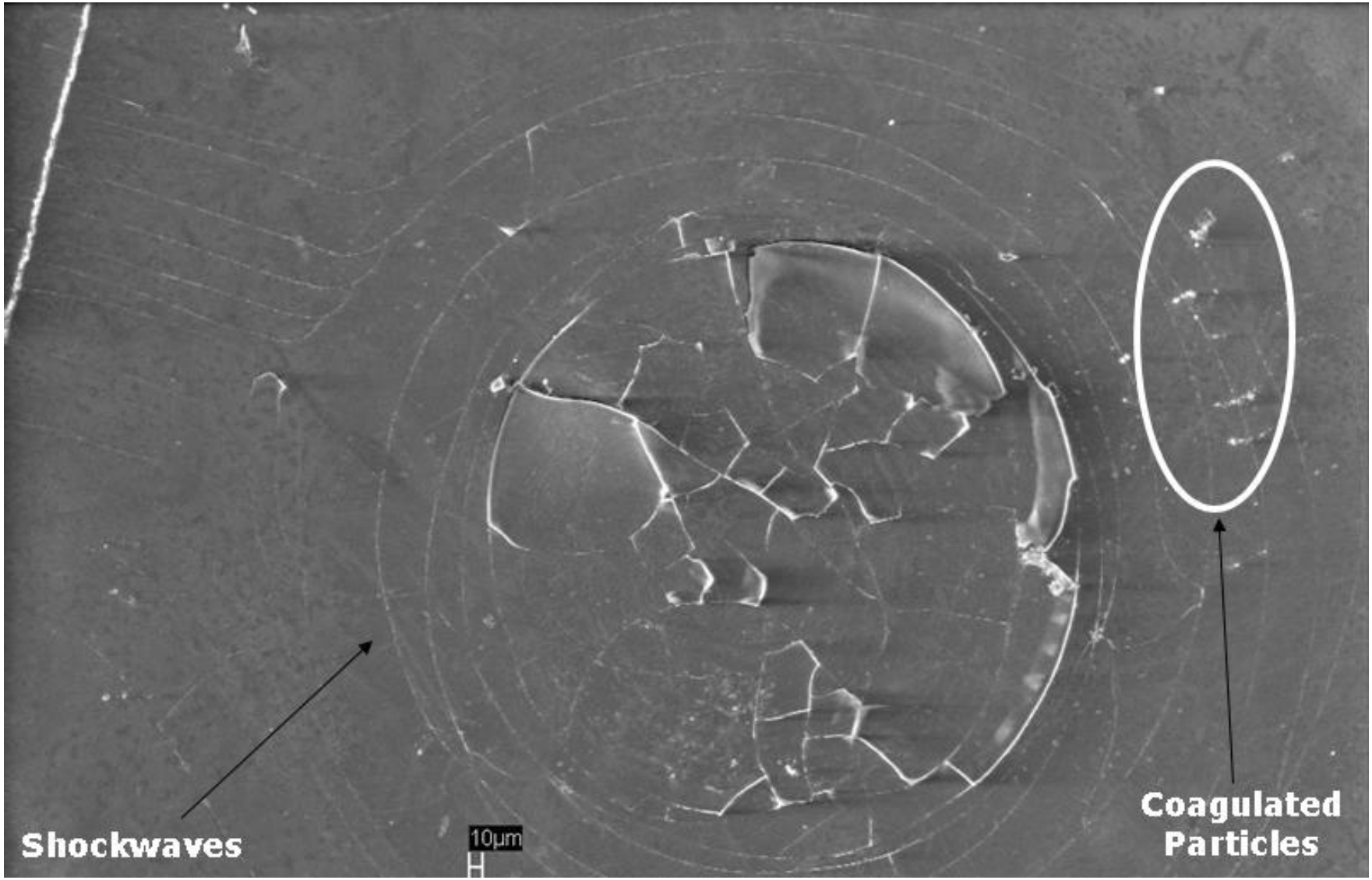

Figure 4: SEM image of LIBS interrogated of a float glass

Molecular Processes within the Plume during and after Plasma Generation

When a plasma is created it expands in all directions at such a velocity (10^5 m/s) that it creates a shockwave. However, the direction of the most expansion is in the direction normal to the sample's surface. It is believed that there are three different processes that occur during the plume expansion.

At pulse widths with low pressures, multiphoton ionization occurs through absorption of the a few photons from the lasers radiation simultaneously. This then leads to multiphoton ionization of some of the species and creates a few free electrons through three body collisions with photons and neutrals.[17, 35, 54, 55]

At pulse widths with higher pressures, i.e. nanosecond pulses, the process differs.[55] This process is the two step process, described below:

- Continuum absorption of the laser radiation by the free electrons through an inverse bremsstrahlung process.[35]
- Inverse bremsstrahlung then leads to avalanche ionization which is initiated by a free electron which then ionizes other species in the system through collisions, more electrons are produced, more energy is absorbed from the laser and an avalanche occurs. Ultimately increasing the electron density and the temperature of the gas or a breakdown.[5, 17, 35, 42, 55]

After plume creation and expansion, there is a significant amount of continuum "white light" emission observed. This emission is due to bremsstrahlung radiation and radiative recombination. Bremsstrahlung radiation occurs from the deceleration of the electrons in the system.[37] Continuum emission is a broad band emission that spans the wavelength range (Figure 5). Therefore, a time-resolved spectrometer is necessary to remove such continuum from the resulting spectra (Figure 5). Removal of the continuum emission can be achieved by opening the spectrometer gate after emission has ceased. During this radiative phase, ionic emissions are generally seen but are usually hidden amongst the continuum emission. Neutral and molecular emissions have a longer lifetime and can be observed after continuum emission has ceased.[5, 56]

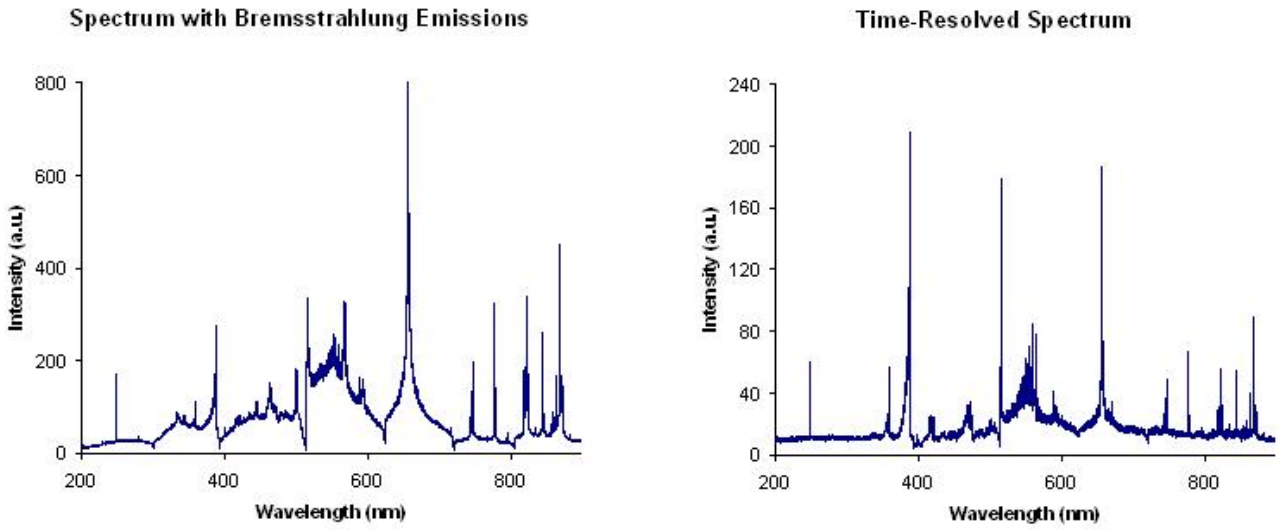

Figure 5: Representative spectra of a spectrum with bremsstrahlung emission and a time-resolved spectrum.

Particles in the plasma lose their initial momentum through many processes after plume creation: collisions with the atmospheric gas, recombination, attachment, diffusion, and excitation of the electronic level. Diatomic species can lose their momentum through other processes such as vibrational and rotational excitations. These processes lead to plasma cooling and eventually photon radiation of the species in the system. During plasma cooling, the species recombine to form atoms and diatomic species.[55, 57, 58]

Processes are different when a plasma is generated in a vacuum. After plasma generation, the particles disperse due to the lack of confinement by the surrounding atmosphere. When the plasma is created in air, the plasma is confined to a general area because the air is too heavy to move and there are many collisions that lead to plasma cooling. However, in a vacuum there are little to no collisions which and recombination takes much longer than in an air atmosphere. The main process of recombination is through radiative recombination, refer to equation 13.[17, 57]

$$M^{+} + e \rightarrow M + h\nu \qquad \textbf{(13)}$$

Determination of the Plasma Temperature

There are many types of temperatures that can be calculated for laser induced plasmas: electron, excitation, ionization, vibrational, etc. These temperatures may or may not agree due to the inhomogeneous nature of the plasma during the early states of

formation. As the plasma heads toward a cooling stage, gradually equilibrium is reached through collisions between the plasma species, as described earlier.[17]

Plasma Temperature Calculation

The plasma electron temperature can be calculated using the Boltzmann equation (14).[59]

$$\ln\left(\frac{g_i A_{ij} c}{I_{ij}\lambda}\right) = \frac{E_i}{kT_{app}} + \ln\left(\frac{4\Pi g_0}{hlN_0}\right) \quad \textbf{(14)}$$

In equation 14, g_i is the statistical weight of the upper excited state i; A_{ij} is the transition probability from the excited state to the lower state j; I_{ij} is the intensity of the peak at the wavelength λ, E_i is the upper energy level of the excited state, and T_{app} is the apparent electron temperature. The apparent temperature is used initially because the true electron temperature can only be obtained if the plasma is determined to be at LTE.[59] The speed of light and the Boltzmann constant are denoted by c and k, respectively. To calculate the T_{app}, the log of the weighted intensity (left hand side of equation 14) is plotted against the upper energy level for that peak. Multiple lines from the same element are used to calculate the plasma temperature in order to obtain a more accurate estimate of the plasma temperature. The resulting slope obtained is equal to $-\frac{1}{kT_{app}}$. The Boltzmann plot intercept is rarely used due to the difficulties in obtaining absolute intensity measurements; therefore, relative intensities with respect to the most intense peak are generally used.[59]

Depending on the element used, the calculated temperature varies due to the elemental reactions within the plasma. The Boltzmann plot can calculate the excitation temperature more accurately from atoms than from ions, if the plasma is at LTE.[59, 60] If there is a great deal of scattering about the best fit line then the LTE approximation is void.[61] This is said to occur when radiative decay is the dominant energy transfer mechanism over electron collisions as the plasma expands and/or cools. To correct for non-equilibrium effects on the temperature calculation and obtain a result more consistent with LTE, a correction factor (b_i) can be used. The b correction factor (equation 15) is a ratio of experimental population density of the excited species i ($N_i^{\exp}$) to the population density predicted by the Saha and Boltzmann distributions (N_i^{LTE}) at the excitation source temperature: [45, 59, 62-64]

$$b_i = \frac{N_i^{\exp}}{N_i^{LTE}} \qquad \textbf{(15)}$$

Burton and Blades[46] have reported correction factors for atomic (b_a) and ionic (b_i) transitions using steady-state collsional and radiative arguments (equations 16 and 17):

$$b_{i,atom} = 1 + \left(\frac{6.55x10^{13} E_\infty \left(E_\infty - E_i\right)^{2.607}}{N_e T^{0.107}} \right) \qquad \textbf{(16)}$$

$$\frac{1}{b_{i,ion}} = 1 + \left(\frac{1.27x10^{11} E_i^3 T^{1/2}}{N_e} \right) \qquad \textbf{(17)}$$

The energy terms are in eV, densities are in cm^{-3} and temperature is in Kelvin (K). E_∞ is the first ionization potential; E_i is the upper energy level of the individual transition; N_e

is the electron density and T is the electron temperature. When the b factor is included, the Boltzmann plot should shift towards linearity. The corrected Boltzmann equation is written below:[46]

$$\ln\left(\frac{g_i A_{ij} bc}{I_{ij}\lambda}\right) = \frac{E_i}{kT_{app}} + \ln\left(\frac{4\Pi g_0}{hlN_0}\right) \quad \textbf{(18)}$$

In utilizing the Boltzmann plot method to calculate the electron temperature, the plasma must be optically thin so that emitted photons can escape the plasma without further interaction and an accurate measurement of their intensities can be obtained.[33, 35, 36, 50, 65] To verify if plasma is optically thin with respect to a certain element, the transition probabilities and the statistical weights of the upper level must be known for that elemental emission lines. If the ratio of the observed intensities is consistent with the ratio predicted from the statistical weights, then the plasma with respect to this element is optically thin. To determine if the induced plasma for the glass samples was optically thin, sodium lines 288.158 nm and 249.52 nm were used. Based on the ratio of the emission intensities it was determined that these plasmas were optically thin with respect to these Si emission lines.

Electron Density

The electron density can determine if a plasma is close to LTE.[33, 35] There are many ways to determine the electron density of a plasma; of which, includes usage of the

electron temperature. Among the equations that use the electron temperature to calculate the electron density is the Saha equation (equation 11).[40-43, 66] However, when the electron temperature is not accurately known there are equations that do not use temperatures to measure the electron density. The amount of peak broadening at the full width at half maximum (FWHM) can be used to determine the electron density.

There are four types of broadening: natural, pressure (Stark), Doppler (thermal) and opacity.[34, 67, 68] Natural broadening is generally negligible, and consists of either: Van der Waals broadening (corresponding short range interactions) or broadening by resonance (excitation energy transfer where emitted photons are reabsorbed).[69] The type of pressure broadening that is most prominent in the spectral peak width is Stark broadening in the line widths are broadened due to "interactions of the radiating ions and atoms with surrounding particles"[34] in the electric field.[68] Since Stark broadening is based on the electron density, calculation of this parameter is generally used as an estimate. Doppler (thermal) broadening is less prominent in dense plasmas. Doppler broadening actually shifts the maximum intensity center line of the peak.[69 (pg 228)] Broadening based on the opacity of the plasma can be destructive to the emitting spectral profile of the emitting photons because it can lead to self-reversal lines. This effect is wavelength dependant and emitting photons at the central wavelength can be reabsorbed by particles in the plasma as it travels to the outside wall of the plasma. This leads to broadening because the center of the emitting spectral profile (at a particular wavelength) has a higher probability of being reabsorbed due to the dense

population of photons at this wavelength than the edges of the profile. Therefore, the intensity of the profile edges can be more intense than the photon center (refer to Figure 6), this type of peak is considered to be a self-reversed line.[50, 70, 71]

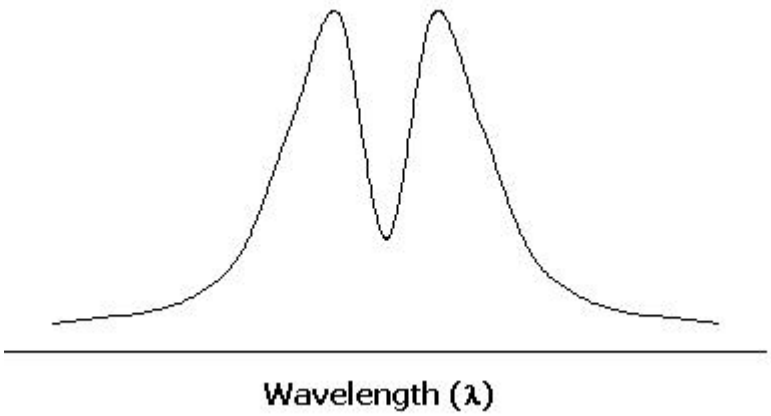

Figure 6: Illustration of the spectral profile of a self-reversed peak

The N_e was determined via Stark broadening in this project. The electron density relies on determining the true FWHM, initially. To do this, the FWHM of a representative peak is subtracted from the questioned peak FWHM. The representative peak is generally a Mercury peak and it accounts for instrumental broadening.[36, 72]

$$\Delta\lambda_{true} = \Delta\lambda_{observed} - \Delta\lambda_{instrument...} \quad \textbf{(19)}$$

The true FWHM ($\Delta\lambda_{true}$) of the peak in question is the difference between the observed FWHM ($\Delta\lambda_{observed}$) of that peak and the FWHM of the instrument ($\Delta\lambda_{instrument}$). Instrumental broadening can be determined by obtaining the FWHM of a Mercury peak

from a HG-1 Mercury-Argon calibration source (Ocean Optics, Dunedin, FL, USA). In general, the FWHM of a peak is equivalent to

$$\Delta\lambda_{1/2}\left(\overset{o}{A}\right) = 2w\left(\frac{N_e}{10^{16}}\right) + 3.5A\left(\frac{N_e}{10^{16}}\right)^{1/4}\left[1 - 1.2N_D^{-1/3}\right]\cdot w\left(\frac{N_e}{10^{16}}\right) \quad \textbf{(20)}$$

where the first parameter is the contribution from electron broadening, the second parameter is the ion broadening correction, electron impact parameter (w)[34], A is the ion broadening parameter, N_D is the number of particles in the Debye sphere and N_e is the electron density (cm^{-3}). Since there is a small contribution from ionic particles in plasma during the radiative processes, the second parameter in equation 9 is negligible. Therefore, equation 20 can be reduced to equation 21 which can be used to calculate the electron density of the plasma.[36, 72]

$$\Delta\lambda_{1/2}\left(\overset{o}{A}\right) = 2w\frac{N_e}{10^{16}} \quad \textbf{(21)}$$

Determining the electron density based on this equation is less tedious because this calculation is independent of an LTE assumption. If the electron density is greater than the electron density lower limit then the assumption of the plasma being at LTE can be accepted. The lower limit of the electron density can be calculated by[17, 23, 36]

$$N_e\left(cm^{-3}\right) \geq 1.6\cdot 10^{12}\sqrt{T_e\left[\Delta E(eV)\right]^3} \quad \textbf{(22)}$$

where T_e is the calculated temperature from the Boltzmann plot and ΔE is the largest difference of the energy transition of the peaks used for temperature calculation.

The lower limit can also be calculated by[59]

$$N_e\left(10^{17}\,cm^{-3}\right) >> 30{,}545\sqrt{T_e(K)}\left(\frac{z^2}{\lambda(nm)}\right)^3 \qquad \textbf{(23)}$$

where T_e is the electron temperature that has previously been calculated through the Boltzmann plot, z is the degree of ionization (1 for atoms and 2 for ions) and λ is the wavelength for which the lower limit is to be calculated. This calculation should be made at the shortest and the longest wavelengths of the elemental emissions used. If the N_e is higher than the lower limit at each wavelength, then the LTE assumption can be accepted for every wavelength.

Plasma Temperature and Electron Density Results

It is possible, in theory, to use the plasma temperature to normalize spectra to a specified temperature to eliminate significant fluctuations in back-to-back spectra of same samples. To normalize these spectra, the plasma temperature would be calculated for a standard reference sample and the questioned sample. The peak intensities in the questioned spectrum would be back-calculated and corrected based on the calculated temperatures. To do this type of calculation, the peaks have to be completely resolved in order to accurately determine the identity of each peak. However, do the resolution limits of the LIBS2000+ spectrometer, of approximately 0.5 Å, accurate peak identification is unachievable. In the case that two "reasonable" peaks overlap and both elements are present in the sample, the peak can not be used for plasma calculation. This is because the overall intensity of this peak may be a

contribution of either or both elemental emissions. Therefore, this elemental emission intensity can not be used for calculating the plasma temperature and another set of elemental emission must be used. It is imperative to have good spectrometer resolution in order to accurately identify the peaks for plasma temperature calculations.

Since the samples used for determining the plasma temperature are glass, the silicon peaks can be used for calculating the plasma temperature based on equations 14 and 18. Using the M.I.T. Wavelength Emission Tables[73], the elements emitting at emission wavelengths surrounding silicon peaks were investigated and none of the elements emitting at these wavelengths are components of glass. In addition to this information and the presence of the most sensitive silicon peak; it can be ascertained that the other peaks can be identified as silicon. The most sensitive peak is indicative of an element's presence in a sample. The most sensitive peak generally has the highest transition probability; therefore, if an element is present in the sample, this peak will be present in the spectra. This is true for many elements, for both atomic peaks and the ionic peaks. If, however, the most sensitive peak is not present, it is reasonable to assume that this element is not in the sample or that the most sensitive peak is not observed in the spectral region. Plasma temperature calculations required accurate peak identification and using multiple lines ensure a better estimation of the temperature. Therefore, if there is an outlier it may be reasonable to assume that the outlier is not an accurately identified peak.

Electron Density Calculation

To calculate the electron density for the glass samples, the most sensitive Si peak at 288.16 nm and the Hg peak at 334.16 nm were used to determine the true FWHM of the silicon peak by using equation 22. The Hg peak was recorded from Hg/Ar lamp (Ocean Optics, Dunedin, FL, USA). The electron impact parameter (w), 0.00561 Å, was acquired from tables in Griem's book.[34]

To calculate the FWHM for N_e determination, experimental widths across a peak were fitted to the Gaussian function[37]:

$$y(x) = ae^{-(x-b)^2/2\sigma^2} \quad \textbf{(24)}$$

Where a is the height of the peak, b is the center of the peak and σ is the variance in at the peak's FWHM. The variance σ is related to the FWHM of the peak by the following equation:

$$FWHM = 2\sigma\sqrt{2\ln(2)} \quad \textbf{(25)}$$

Plasma Temperature Calculation

Silicon peaks were used to evaluate the temperature of the plasma for glass samples, since its presence is assured and the induced plasmas are optically thin with respect to these peaks. In this study, the electron temperature of the plasma was calculated by the Boltzmann and the corrected Boltzmann equations 14 and 18, respectively. A Boltzmann plot used to calculate the plasma temperature is illustrated in Figure 7. The blue points represent values calculated initially before any correction was applied. Red

points represent values calculated after the b correction for atoms was introduced. It is to be pointed out that the r^2 value for the "1st Correction" set has significantly increased to 0.87 from 0.60 by applying the b correction. This shows that the temperature calculated from this set of values is closer to the actual plasma temperature than the initially calculated temperature.

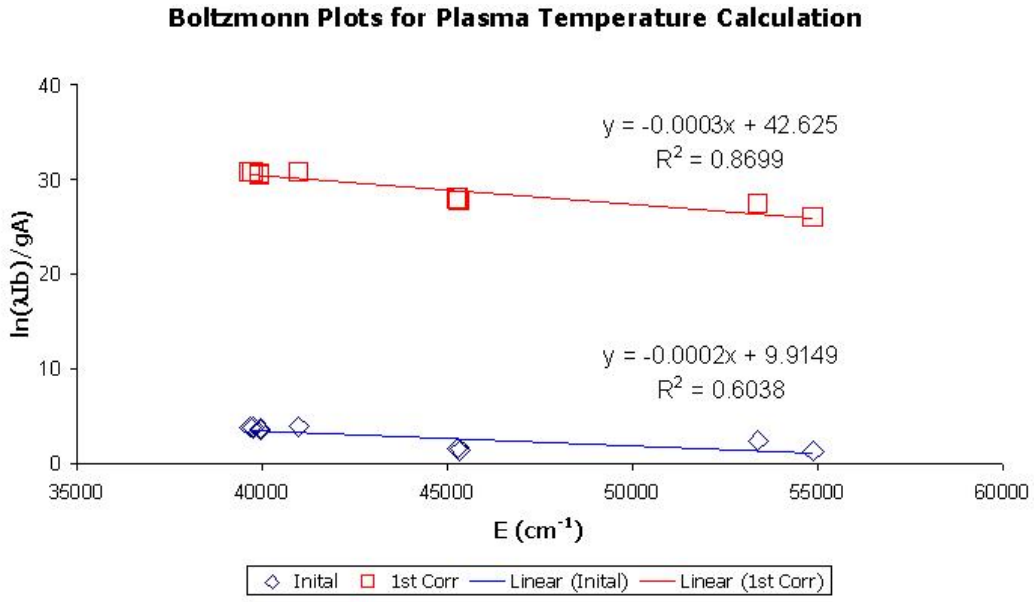

Figure 7: Boltzmann plot for plasma temperature calculation

The temperature of the plasma was calculated for ten samples from each group of glass types. The electron density and plasma temperature are presented in Table 1.

Table 1: Calculated electron density and plasma temperature for glass samples

	Auto Float (Float)		Auto Float (Non-Float)		Auto Side Mirror (ND)		Headlamp		Brown Container	
Sample	N_e cm^{-3} (10^{15})	Temp (K)	N_e cm^{-3} (10^{15})	Temp (K)	N_e cm^{-3} (10^{15})	Temp (K)	N_e cm^{-3} (10^{15})	Temp (K)	N_e cm^{-3} (10^{15})	Temp (K)
1			8.02	4731.17	1.78	4645.33	15.15	4580.88	23.17	4925.50
2	9.80	4766.20	8.02	5059.92	2.67	4602.57	8.91	4513.04	10.69	4652.43
3	4.46	4879.27	12.48	5087.64			9.80	4393.29	24.96	4769.88
4	11.59	4997.53	14.26	4955.56			3.56	4406.60		
5	4.46	4595.86	0.89	5036.11	6.24	4684.07	6.24	4764.72		
6	8.91	4954.61	8.91	4855.63	6.24	4640.43	12.48	4622.73	16.04	4950.71
7	7.13	4753.87	9.80	4815.34	2.67	4601.01	19.61	4724.00		
8	2.67	4753.87	2.67	4589.40	5.35	4646.10				
9	0.89	4868.11	3.56	4990.74	0.89	4664.98	0.89	4363.72	5.35	4393.35
10	5.35	4748.90	5.35	4845.16	5.35	4626.38	9.80	4733.19	9.80	4858.56
Average Temp		4813.14		4896.67		4638.86		4566.91		4758.40
%RSD Temp		2.56		3.25		0.62		3.42		4.40
N_e Limit (23)	8.93		8.85		8.62		8.64		8.94	
N_e Limit (22)	35.25		34.92		34.04		34.08		35.27	

For the plasmas generated for the above samples, the assumption of LTE should not be accepted. The calculated N_e is not greater than the electron density lower limits presented at the bottom of Table 1 for most of the samples, which may illustrate that the plasmas induced during these analyses were not at LTE. The N_e could not be calculated accurately for some of the samples, due to poor FWHM measurements.

Silicon emissions were used to calculate the plasma temperature for two back-to-back float glass (float side) samples collected a year prior for comparison with the above data set. This was done to determine how different the plasma temperatures are for the same sample analyzed in the same day. The temperature for the first spectrum was calculated at 7,694.09 K, while the temperature for the second spectra was calculated at 7,940.37 K. For these plasmas, the LTE assumption can be accepted because the electron density is approximately 5.44×10^{16} cm^{-3} which is greater than the N_e lower limit of 4.42×10^{16} (based on equation 22).

There is a significant difference between the temperatures of the first data set (Table 1) and the second data set; where the temperature for first set was calculated to approximately 4,700 K and the second set was approximately 7,700 K. In addition to this difference, the electron density for the first data set was on average 5.79×10^{15}, whereas the electron density for the second set was significantly larger. This difference may be due to laser degradation over a one year time period. This degradation could

have caused less intense spectra, lower electron density and hence, a lower plasma temperature.

Precision of the LIBS Instrumental Method

Variations of the intensity of the induced plume can be affected by the sample's temperature[74], the topography of the sample's surface or shot-to-shot variations of the laser's interaction with the sample[75]. To determine the precision of the LIBS analytical method on the same day and on different day analyses, a study was conducted that focused on optical alignment and laser fluctuations. This study was conducted on three separate days. On each day, the optical alignment was optimized to produce the most intense spectra by adjusting the angle of the fiber optic lens and the height of the focal lens. Optimization was set using a borosilicate glass sample. NIST SRM 610 sample was used to calculate the reproducibility of the analytical method. Average LIBS spectra, consisting of an average of 10 single shot spectra, was collected at five different locations on the SRM sample. This process was repeated each day of analysis.

Eleven (11) emission ratios were created for each of the five spectra collected and the %RSD was calculated for each ratio. The average peak ratio %RSD for any particular day was 6.5 ± 1.4%. The emission ratios chosen so that they encompassed the same range of emission that is used in the comparison of glasses described in the methods below. Ratios of back-to-back spectra collected on the same day had relatively low

%RSD; however, these ratios had a significantly larger average %RSD from day to day comparisons, approximately 24.5 ± 29.2% over the three days of analysis. Individual ratio %RSD was as large as 105% in the analysis over the three day period. These results suggests limiting sample analysis of questioned to known comparisons to same day back-to-back analysis.[75] Samples analyzed by LIBS in this study were analyzed on the same day to avoid higher variances during comparisons.

Figure 8 shows inconsistencies of back-to-back laser interactions with the sample glass matrix. Each location was interrogated by 10 single LIBS shots. It is evident from the image that the laser does not interact with the sample consistently. This type of inconsistency can lead to a high %RSD in the analytical method.

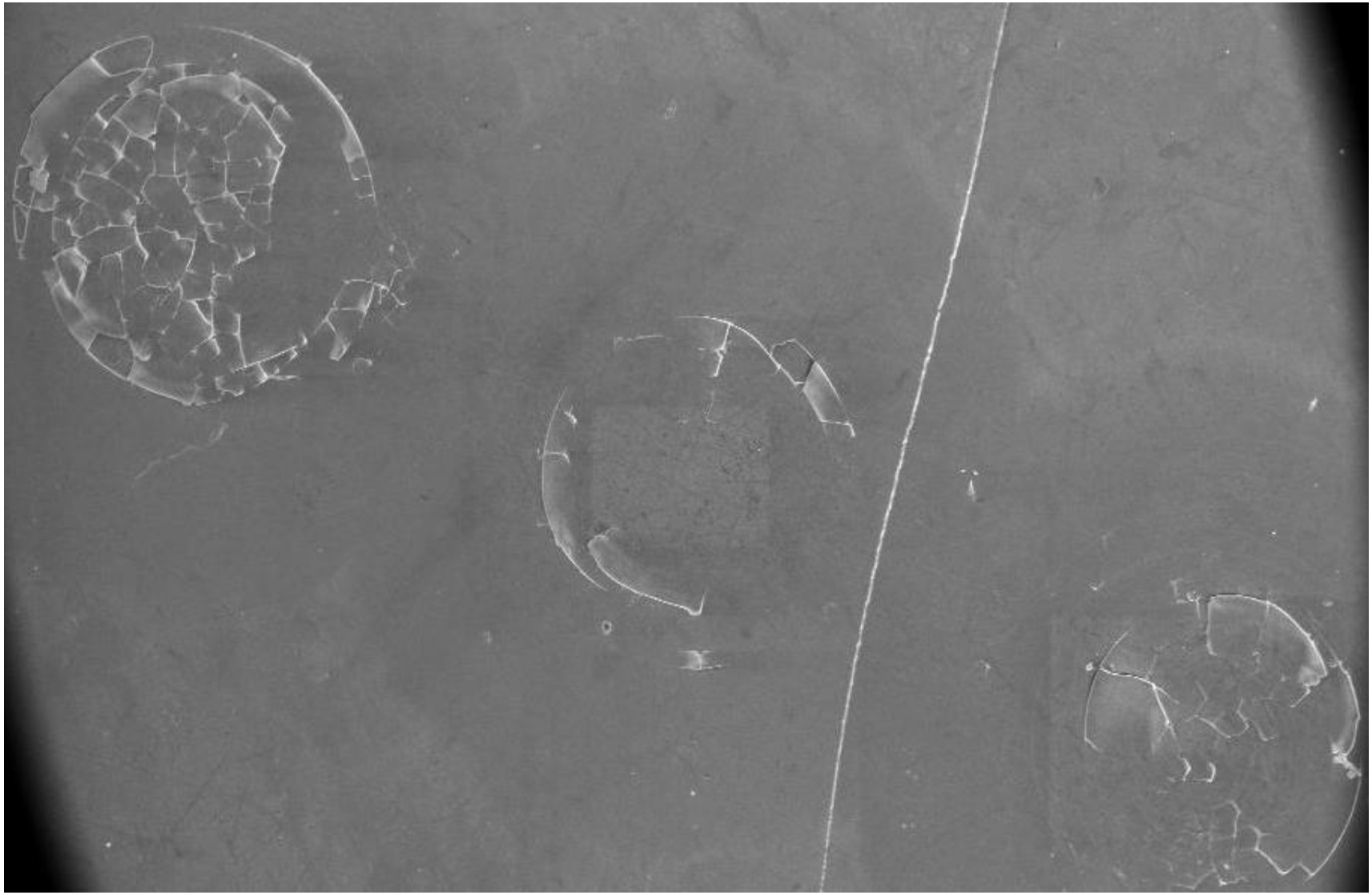

Figure 8: SEM image of a LIBS interrogated float glass that illustrates laser inconsistencies

Other types of unwanted laser-matrix interactions that can occur are presented in Figure 9 (top surface) and Figure 10 (bottom surface). These images show that after 10 single shots, the matrix was melted by the laser interaction. On the top surface of the sample there is evidence of the laser impact and particle recombination but it seems that the sample was melted as well. The bottom surface, away from the actual impact of the laser on the sample, shows that a portion of the sample was melted and left a hole in the sample. There also seems to be a "bubbling" effect probably from heat generated by the laser. While, this did not occur for every sample, it is another inconsistency of the laser-matrix interaction that can affect the resulting spectrum.

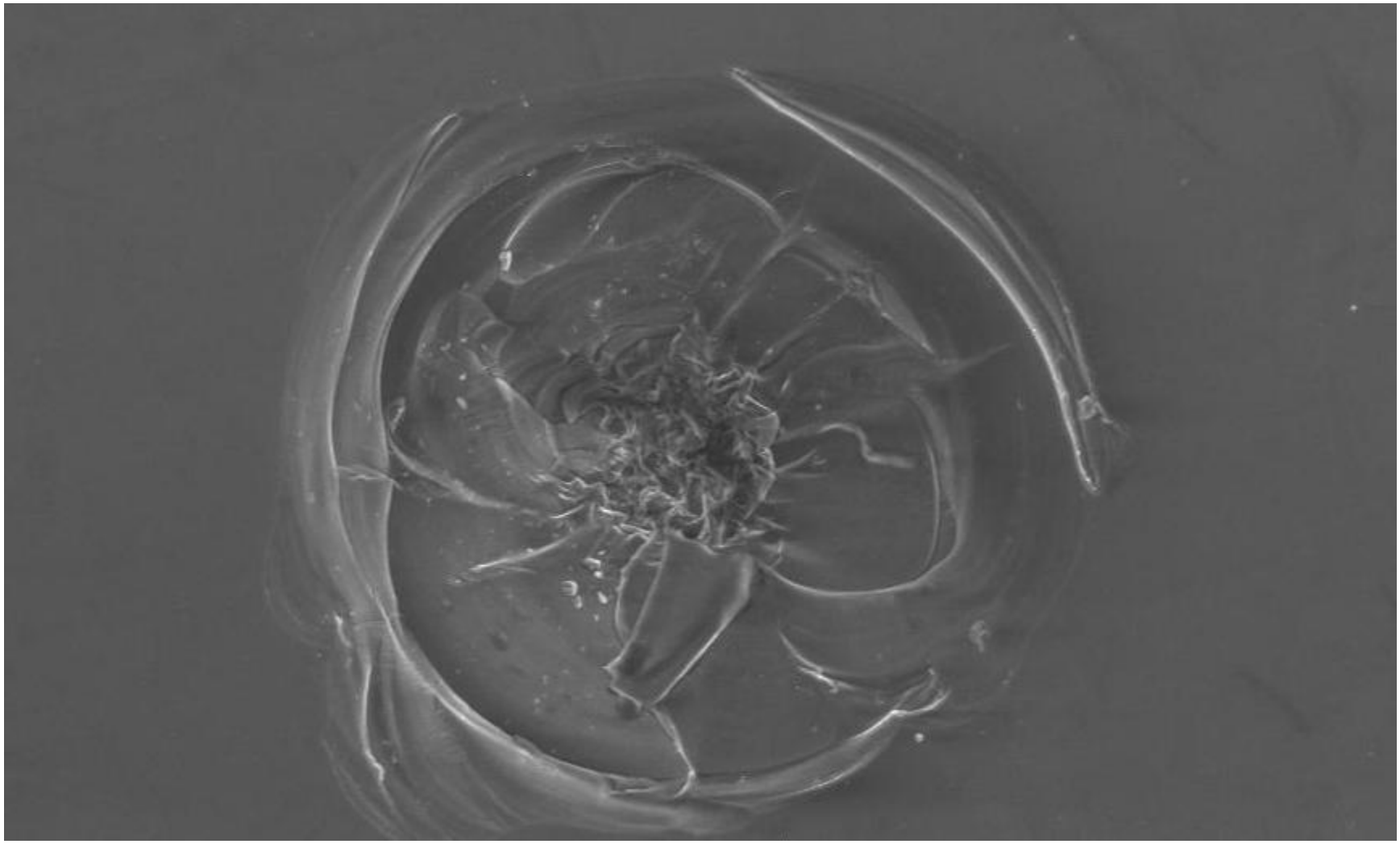

Figure 9: SEM image of a LIBS interrogated float glass which shows a burning / melting effect of the laser (top surface)

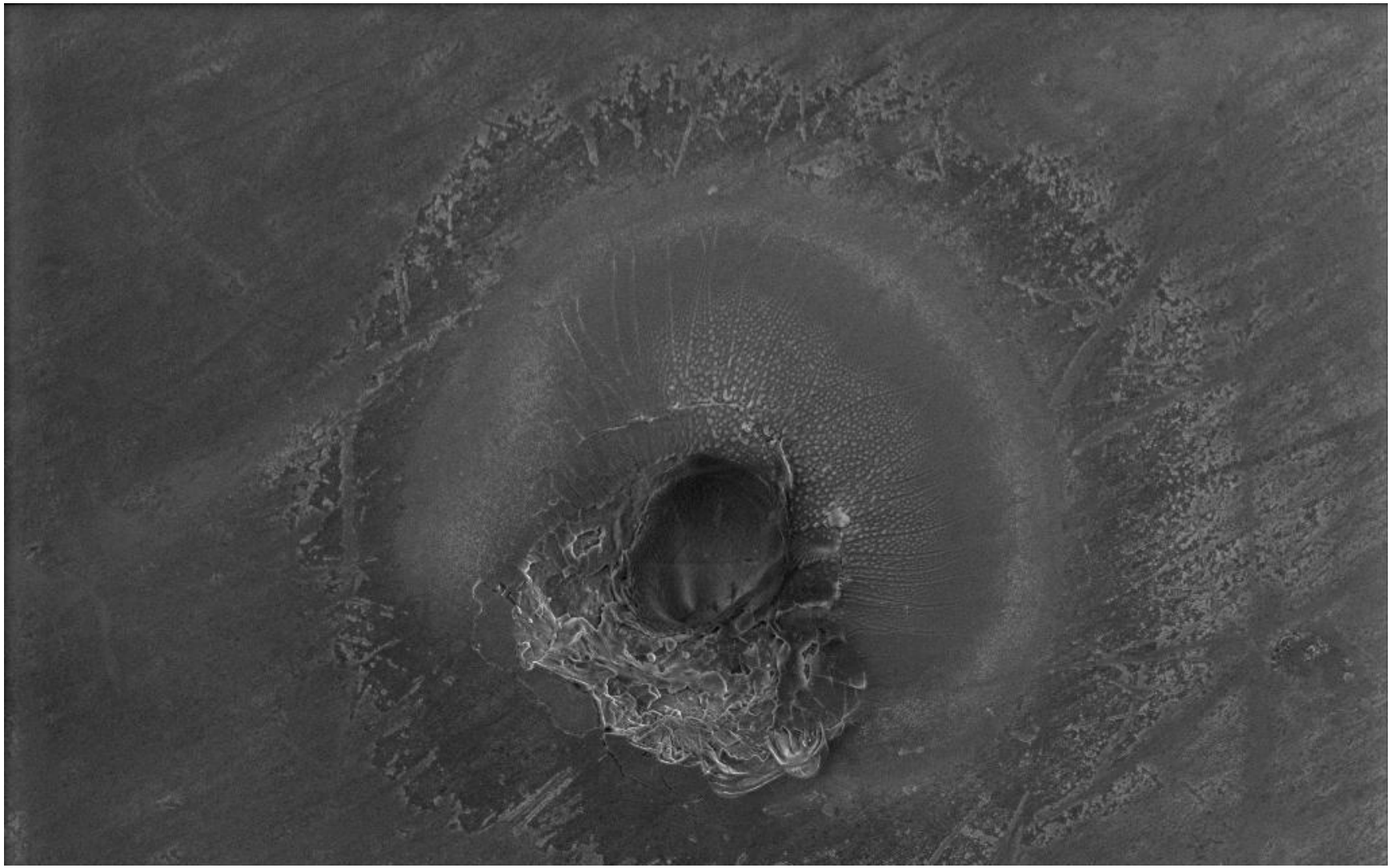

Figure 10: SEM image of a LIBS interrogated float glass which shows a burning / melting effect of the laser (bottom surface)

CHAPTER SIX:
GLASS ANALYSIS AND DISCRIMINATION

Glass is a type of trace evidence found at crimes scenes from automobile crashes to assault cases. This evaluation of LIBS as a viable forensic analytical method was conducted by analyzing glass samples by three main techniques, LIBS, LA-ICP-MS and XRF. Refractive index measurements were used in conjunction with LIBS, LA-ICP-MS and XRF to enhance the overall discrimination power.

Forensic analysis of glass has typically been based on refractive index, dispersion and density analyses.[76] In 1991, the statistical discrimination of flat glass by neutron activation analysis of the sample's elemental composition was demonstrated.[77] The determination of up to 70 elements by ICP-MS was later demonstrated.[78] The forensic significance of glass composition and refractive index has recently been assessed.[79] Results of that study, which examined glass composition using inductively coupled plasma – atomic emission spectroscopy (ICP-AES) demonstrated that the concentrations of ten elements (Ca, Fe, Al, Mn, Sr, Mg, Ba, Ti, Zr, Na) and the refractive index could be used together to distinguish unrelated glass specimens at a level of one in 10^5 – 10^{13} samples.[79] Similar results were later shown to hold for determination of the same ten elements by inductively coupled plasma – mass spectrometry (ICP-MS).[25, 28] The utility of elemental analysis for the discrimination and matching of glass evidence in casework has recently been reported.[80] The importance of discriminating

glasses based on composition has also been demonstrated in a recent report of the analysis of glass-containing gunshot residue by SEM-EDX analysis.[81] Research by Almirall has recently focused on the use of laser ablation inductively coupled plasma mass spectrometry (LA-ICP-MS)[82, 83] and a comparison of LIBS with other techniques for the discrimination of glass fragments.[8, 84] Analysis of glass fragments by synchrotron radiation x-ray fluorescence spectrometry (SF-XRF) showed the discrimination power of this method. Samples that could not be discriminated by RI were determined to be from different sources by this method.[85]

Glass Experimental Analysis

Sample Preparation

In this study, automobile float glass samples were examined on both the float and the non-float side. The float side (tin side) of the glass was identified by the appearance of a light pink emission under a 254 nm (short wave) UV light. The identity of the float side was confirmed with depth profiling using LA-ICP-MS and imaging using SEM-EDX. Using SEM-EDX, the side-view of the sample clearly confirmed the presence of Sn only on the fluorescent side of the glass sample. Detailed compositional mapping of the Sn concentration was not performed due to the low energy limit (20 keV) on the instrument used in this analysis. Glass samples analyzed by SEM-EDX were cleaned with isopropanol and left uncoated for analysis in the variable pressure instrument. Samples were placed on a carbon adhesive disk attached to an aluminum stub for

subsequent analysis. For measurements obtained by LIBS, LA-ICP-MS and XRF there was minimal sample preparation required for elemental analysis.

Refractive Index (RI) Analysis

There were two different variances used to calculate the discrimination percentage of the glass samples via RI measurements. One of the standard deviations used was a literature value of 2.2×10^{-4} obtained from the Forensic Science Handbook.[86] This study suggested that in a 60 cm x 30 cm pane of glass the standard deviation in the refractive index was no more than 2.2×10^{-4} for the glasses samples tested. Based on the accepted standard deviation value, the calculated value of the variance is approximately 4.8×10^{-8}. Based on the RI measurements obtained from the GRIM3, the variance is much smaller, on the order of 10^{-9}, which increased the overall discrimination percentage.

The RI for the glass samples was measured by the GRIM3 instrument (Foster and Freeman, Evesham, Worcestershire, UK). Fragments of each glass sample were measured approximately 14 times. The discrimination power of the RI alone was calculated two different ways at two different confidence levels (CL), 90% and 99%.

Laser Induced Breakdown Spectroscopy (LIBS) Analysis

To analyze the glass samples using LIBS, 5 average spectra, each comprised of 10 single-shots, were collected at different positions on the sample surface. Each spectrum was collected under an argon flow directed over the surface of the sample. Ratios were created from emission lines to minimize laser shot-to-shot fluctuations and as a result it provided better discrimination than individual emission peak intensities. The peaks chosen for creating ratios were baseline resolved, present in most of the glass samples and were present in LA-ICP-MS analysis for direct comparison. The ratios created where based three criteria: (1) the spectral proximity, (2) the transitions having nearly similar degenerate upper energy levels and (3) ratios that span the full spectrum. The ratios chosen for discrimination were based on their ability to discriminate the samples and their F-statistic which was obtained from the ANOVA test.

Great care was taken to ensure that the spectral emissions chosen for the ratio analysis were baseline resolved. As the representative spectrum in Figure 11 illustrates, there are numerous high intensity peaks present in these spectra. However, most of these peaks do not provide effective discrimination between the glass samples because they are present in all glass types with the same relative intensity. Many of the less intense peaks, attributable to trace elemental emissions, yielded higher discrimination of the glass samples examined.

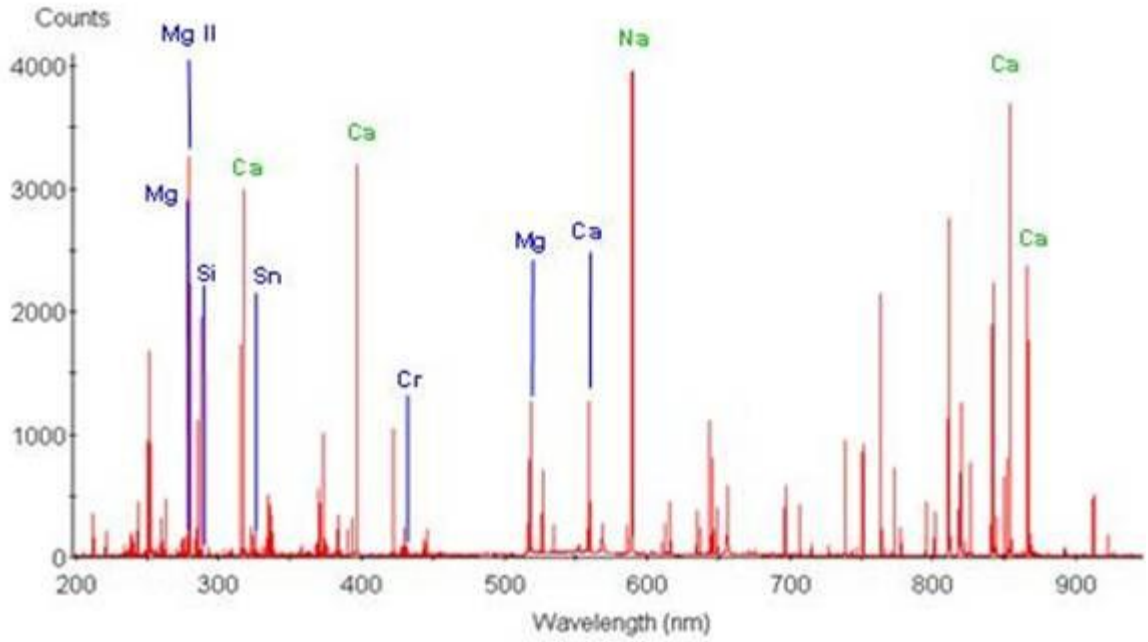

Figure 11: A typical LIBS spectrum of automobile float glass – float side. Species shown in blue were used to construct discriminating ratios. Species shown in green were tested for discrimination and subsequently rejected due to low F-statistics and low discriminating percentages.

Ionic and atomic emission lines present in the majority of glass samples were chosen for discrimination based on the criteria stated in the previous paragraph. Of these emission wavelengths, ratios were created based on their spectral proximity to one another. Utilizing ratios for analysis reduces the effect of shot-to-shot fluctuation from the laser, resulting in lower %RSD for the ratios. Not all emission lines were observed in all of the float glass samples studied; however, most emissions were present in the majority of the samples. The absence of specific emission lines in a given float glass sample spectrum was used as an additional sample-discriminating factor. Pairs of emission lines were chosen to create ratios such that the pairs of lines fell within a

spectral region confined to a single spectrometer. Requiring pairs of lines to be confined to a single spectrometer is intended to guard against spectrometer-to-spectrometer dark current variation. Restricting ratioed peak intensities to peaks having similar upper energy levels was examined; however, due to the limitations of the spectrometer, absolute identification of the peaks was not possible, making the implementation of this criterion impossible with the limitations of this instrument. The emission line ratios that were determined to have the highest F-statistic and a low Pearson correlation coefficient comprised the set of ratios used for overall discrimination of the glass samples (Table 4).

In order to account for instrumental instabilities in the LIBS system, the precision of LIBS analysis of the automobile glass samples was measured by repeated, hourly LIBS analysis of the same float glass sample. The "same-day" %RSD obtained for each emission line ratio was relatively low, 0.8% to 15.0%. LIBS data on all 23 automobile float glass (float side) samples was acquired over the course of a single day, thereby avoiding day-to-day instrumental fluctuations.

Presented in Figure 12 is an illustration of how similar LIBS spectra from the same glass type can be. This similarity can lead to difficulties in full spectral analysis between samples of the same glass type.

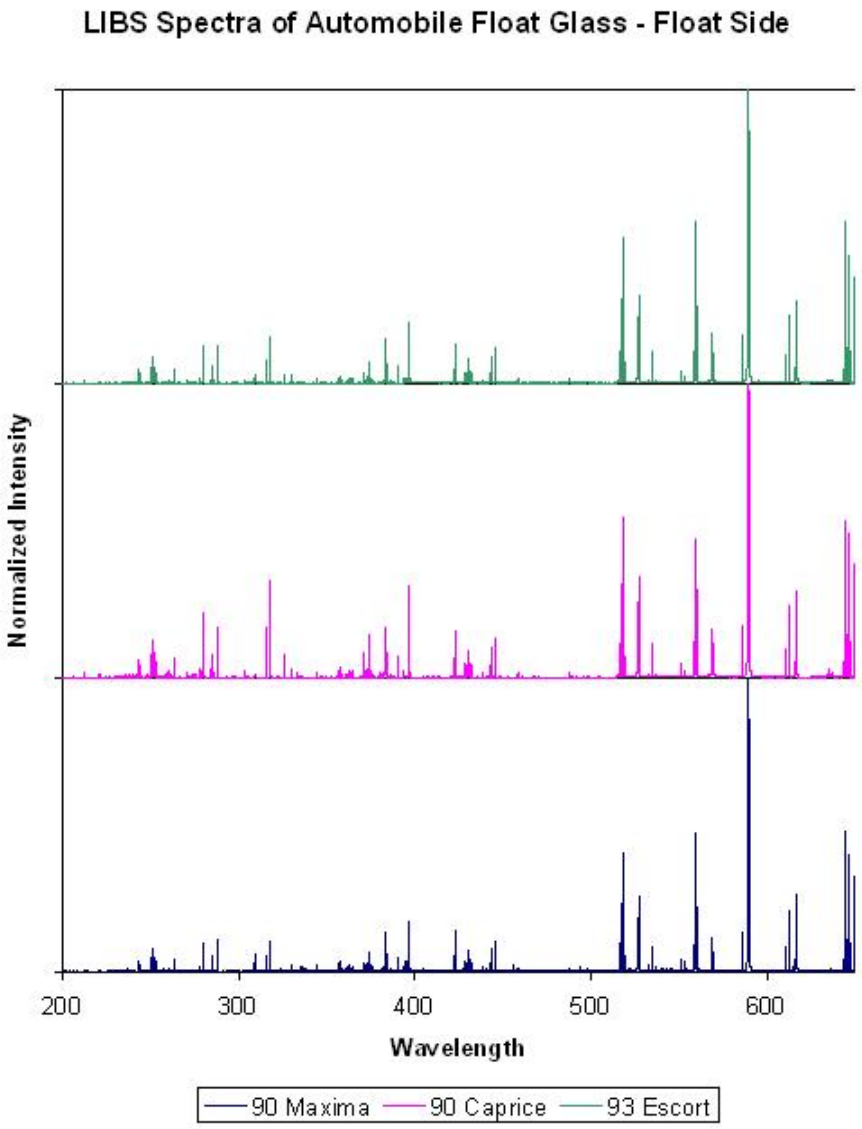

Figure 12: An illustration of the similarity of LIBS glass spectra

Laser Ablation Inductively Coupled Plasma Mass Spectrometry (LA-ICP-MS) Analysis

The LA-ICP-MS methodology comprised of selecting isotopes that were present in the LIBS spectrum and have been used for discrimination in published literature.[82, 87] Isotopic abundance ratios, rather than absolute individual isotopic abundances, were

used for glass discrimination in order to mitigate the effect of pulsating carrier gas flows in the LA-ICP-MS. Isotopes exhibiting a large response (> 100,000 counts) were ratioed to other isotopes with a large response, while isotopes with a smaller response (< 100,000 counts) were ratioed to other ratios with a smaller response. Isotopic ratios were created from the 16 isotopes sampled in order to ensure that results could be compared with the results obtained from the LIBS analytical method. The data analysis was similar to that described for LIBS; ratios were created from LA-ICP-MS isotope abundances to minimize any instrumental fluctuations. Discrimination ratios were chosen based on the Pearson correlation coefficient and the F-statistic value. The F-statistic values were much higher for the LA-ICP-MS ratios than the LIBS ratios due to the more precise nature of the LA-ICP-MS instrumentation.

Raster Experimental Method

Twelve successive LA-ICP-MS repetitions (single laser ablations) were integrated into a single scan. Ten successive scans were collected for each sample layer (the first scan in each layer was discarded to eliminate carryover between the analysis of different layer). The standard deviation for each isotopic ratio was determined from the average of the nine individual scans taken for each layer of sample ablated.

Each layer of glass was compared with the same layer from another glass sample (e.g. layer 1 from sample A was compared to layer 1 from sample B). Each layer,

individually, was evaluated for its discriminating power for the 23 glass samples. The intensities from the three layers ablated were summed for discrimination to ensure a representative sampling of each glass. Layer-by-layer analysis revealed small variations in elemental concentration spatially distributed across the surface of the glass as well as vertical distributions, as revealed by depth profiling of the summed isotopic data from each layer. The discriminating power was determined for each isotopic ratio. The instrumental parameters used for this analysis are presented in Table 2.

Table 2: Instrumental parameters for LA-ICP-MS raster method – glass analysis

Parameter	Value
Laser Output Energy	6 mJ/pulse
Laser Output wavelength	213 nm
Sampling Energy	12 mJ (40%)
Scan Speed	30 μm/sec
Raster Spacing	50 μm
Spot Size	50 μm
Ablation Depth	5 μm
Frequency	10 Hz
RF Power	940 W
RF Matching	1.81 V
Carrier Gas	1.13 L/min
Ablation Cell Vol.	22 mL
Ablation Mode	Raster Layer
Sampling Time	120 minutes
Pre-ablation	Yes
Integration Time	0.1 sec/isotope

Drill-Down Experimental Method

This method was developed because it was the most similar to the LIBS process of analysis. In this method, five positions were analyzed and one scan was done per position. Each scan was comprised of 12 acquisitions with each acquisition is comprised of an average of 12 repetitions. The power used for analysis was 65% of the maximum (6 mJ), the laser frequency was set to 10 Hz and the spot size of the laser was 50 μm. Unlike the raster method where 10 scans was taken per layer, only one scan was collected to minimize any "well" issues due to the laser defocusing after every shot. This technique has been used elsewhere for drill down analysis to identify different layers in the sample.[88, 89] The instrumental parameters for this method are presented in Table 3.

Table 3: Instrumental parameters for LA-ICP-MS drill-down method – glass analysis

Parameter	Value
Laser Output Energy	6 mJ/pulse
Laser Output wavelength	213 nm
Sampling Energy	6 mJ (65%)
Raster Spacing	50 μm
Spot Size	50 μm
Ablation Depth	5 μm
Frequency	10 Hz
RF Power	1140 W
RF Matching	1.81 V
Carrier Gas	1.20 L/min
Ablation Cell Vol.	22 mL
Ablation Mode	Spot Drill Down
Sampling Time	10 minutes
Pre-ablation	Yes
Integration Time	0.1 sec/isotope
Laser Output Energy	6 mJ/pulse

Comparison between LIBS and LA-ICP-MS

For the samples analyzed by the LA-ICP-MS the first layer was ablated to remove any impurities from the surface prior to analysis. A cleaning shot was not performed for the LIBS analysis. A study was performed to determine if a cleaning shot improves the precision of the experimental method. This was assuming that any impurities located on the surface would affect the averaged spectra. To investigate this issue, 10 single-shots were collected in one position with cleaning shots that range from 0 to 5 shots. It was observed that the percent relative standard deviation (%RSD) varied with no trend observed relative to the number of cleaning shots. The random variations in the %RSD were attributed to laser shot-to-shot fluctuations. It was concluded that cleaning shots did not affect the precision of the LIBS method.

X-Ray Micro-Fluorescence (XRMF) Analysis

For samples analyzed by XRMF the surface was cleaned with acetone to remove any residue. Each glass sample was analyzed at 3 different positions on the surface of the glass in order to calculate the variance between replicate measurements on the same samples and different samples. Emission ratios were generated for sample comparison.

Glass Discrimination within a Glass Type

Samples used for Discrimination Analysis

Analysis of the automobile float glass analyzed on the float side was comprised on 23 glass samples (253 unique pairwise comparisons). Twenty-seven (27) samples were analyzed on the non-float side, which lead to 351 unique pairwise comparisons. The non float side was examined to determine if any discriminatory information was evident on this side in comparison to the float side of the glass. Samples of automobile side and rear window float glass were collected from 27 automobiles located at a local salvage yard. Samples chosen were representative of a significant range of automobile make and year of manufacture.

Fifteen (15) headlamp glass samples (105 unique pairwise comparisons) were collected for analysis. Nine samples were collected from a local salvage yard of which two were from unidentified sources. Six samples were purchased at various aftermarket dealers. The outside of the headlamp glass was examined to provide a smooth surface in comparison to the inside of the sample. Since glass is not a completely crystalline material[86] and atmospheric elements can leach into the top layer of the sample, sampling of the side of the glass exposed to the environment may identify any elements unique to location of storage of the automobile.

The sample set of the side mirror glasses was comprised of 34 samples (561 pairwise comparisons). These samples were collected from 32 automobiles located at a local salvage yard. The driver and the passenger side mirrors were collected for two automobiles. The samples were analyzed on the coated and the non-coated side of the glass. The non-coated glass side of these samples was the non-float side of the float glass used to construct the mirrors.

Fifteen (15) brown container glass samples (105 unique pairwise comparisons) were examined on the inside of the sample in order to obtain a level surface for analysis.

ANOVA/Tukey HSD Data Analysis

Refractive Index

Automobile Float Glass – Float Side and Non-Float Side

The first RI comparison utilizing the variance calculated for each sample, ANOVA followed by the Tukey HSD post-test, discriminated 96.4% and 95.7% at the 90% confidence level (CL) and the 99% CL, respectively. Using the literature RI variance of $4x10^{-8}$, 87.4% and 85.0% of the sample pairwise comparisons could be discriminated at the 90% CL and the 99% CL, respectively. Since using the literature value provided less discrimination it was removed from subsequent discriminations where the refractive index was used in combination with data from other analytical techniques.

Headlamp Glass

The refractive index was able to discriminate 80.0% and 76.2% of the fifteen glass headlamp samples at the 90% CL and 99% CL, respectively, using the ANOVA/Tukey HSD analysis.

Side Mirror Glass

At the 90% CL, only 46.5% of the 34 side mirror glass samples could be discriminated and only 42.3% could be discriminated at the 99% CL. The discrimination percentage is lower for this set of glass samples because a few samples (~11 samples) had a large RI variance greater than $1x10^{-7}$. If these samples are removed from this set, the overall discrimination by refractive index alone increases to 88.0 and 85.0% at the two confidence intervals.

The large variance in RI exhibited by some samples may be attributed to heterogeneity of the glass itself; however, there was a clear layer over the reflective side that may have affected the variance of these samples. The clear layers of these samples were analyzed by FTIR-ATR and were determined to be of a type of organic polymer, similar to poly aryl ether.

Brown Container Glass

Of the brown glass samples, 81.9% could be discriminated at a 90% CL and only 75.2% at the 99% CL. It was noticed that some of the brown glass samples had an inner layer of a clear glass which had a completely different refractive index. This increased the variance of some of the brown container samples.

Elemental Ratios

Elemental ratios were created for the discrimination of glass samples which was calculated by using the ANOVA/Tukey HSD analysis. Elemental ratios consisted of emission line ratios and isotopic abundance ratios.

LIBS

Automobile Float Glass – Float Side

A total of 92.9% of the float glass samples could be discriminated at a 90% CL based on the LIBS ratios and 82.2% could be discriminated at the 99% CL. Utilizing the experimental RI variance from this work, the overall discrimination increased to 100% at the 90% CL and 99.2% of the samples could be discriminated at a 99% CL (Table 4). The correlation values calculated for the emission ratios used in the discriminating comparisons were less than 0.6, which illustrates that these ratios were minimally correlated. The F-statistic value of the discriminating ratios for this sample set ranged

from 6 – 28. The Sn/Na ratio, which had an F value of 28 provided the most discrimination of the 253 unique pairwise comparisons.

Table 4: LIBS emission discrimination percentages for automobile float glass – float side

Emission Line Ratios	F-statistic	90%	99%
Mg II (280.271 nm)/Sn (283.998 nm)	6.2	15.4	8.3
Si (288.158 nm)/Al (309.271 nm)	17.8	38.7	30.0
Sn (328.233 nm)/Na (330.237 nm)	28.4	50.2	40.7
Na (330.237 nm)/Ti II (336.123 nm)	10.0	28.9	19.4
Ca (422.673 nm)/Ti (428.335 nm)	22.3	15.4	10.7
Cr (428.973 nm)/Ti (430.839 nm)	9.8	23.7	16.6
Mg (518.36 nm)/ Ti (521.038 nm)	9.3	19.0	13.0
Sn (326.233 nm)/ Ti II (336.123 nm)	10.8	25.3	17.8
Fe II (259.94 nm)/Mg (277.983 nm)	10.1	32.4	20.9
Ca (649.378 nm)/Ba (649.876 nm)	16.7	19.0	17.0
Discrimination by Emission Ratios Only		92.9	82.2
Experimental RI (10^{-5}) Only		95.7	94.9
Emission Ratios + Exp. RI		100.0	99.2

Automobile Float Glass – Non Float Side

The eight LIBS emission ratios chosen for discrimination provided 82.3 % discrimination at the 90% CL and the 71.8% discrimination at the 99% CL. Combining the LIBS ratios

and the measured RI data allowed 99.4% and 98.9% of the samples to be discriminated at the 90% CL and the 99% CL. The F-statistic values calculated for this set of samples ranged from 7 – 25.

Table 5: LIBS emission discrimination percentages for automobile float glass – non-float side

Emission Line Ratio	F-statistic	90%	99%
Si (221.174)/Nb (243.538)	10.4	14.2	14.2
Si (252.851)/Mn II (257.610)	24.3	21.4	14.5
Si (288.158)/Ca II (317.930)	9.1	26.2	19.1
Fe (373.713)/U (383.146)	11.5	32.8	24.5
Cr (390.568)/Fe (393.591)	25.2	27.1	19.6
Fe (393.591)/Ca (422.670)	7.3	15.7	10.2
Ca II (527.018)/Mn (534.940)	11.6	14.0	10.5
Na (819.479)/Cl (822.174)	9.5	29.9	22.5
Emission Ratios Only		77.5	67.0
Emission Ratios + Meas. RI		99.2	98.3

Headlamp Glass

Using the LIBS data alone, approximately 98.1% of the glass samples could be identified at a 90% CL. At the 99% CL, 97.1% could be discriminated. With the addition of the refractive index information, 100% of the samples could be differentiated from one another at both confidence intervals (Table 6). The Pearson

correlation revealed three pairwise comparisons that had an r greater than 0.8; due to the discrimination percentage these values were retained.

Table 6: LIBS emission discrimination percentages for headlamp glass

Emission Line Ratio	F-statistic	90%	99%
B (249.772)/Si (250.690)	191.9	60.0	48.6
Sb (252.851)/Fe II (259.940)	5.4	17.1	9.5
Mg II (280.271)/Si (288.158)	12.0	21.0	13.3
Th II (339.203)/Zr II (343.823)	51.3	63.8	54.3
U (394.382)/Al (396.152)	16.1	47.6	44.8
Al (396.152)/Ca II (396.847)	14.0	38.1	27.6
Zr II (343.823)/Ce (349.621)	22.1	53.3	49.5
Na (819.479)/Cl (821.204)	16.1	41.0	30.5
Na (819.479)/Cl (822.174)	12.8	38.1	32.4
Emission Ratios Only		98.1	97.1
Emission Ratios + RI		99.1	99.1

Side Mirror Glass

The glass side of the side mirror samples was analyzed by the LIBS method. Based on discriminating ratios, 61.3% of the automobile side mirror was discriminated at a 90% CL. At the 99% CL, only 53.7% could be discriminated by elemental ratios alone.

When the RI data is added, the overall discrimination increased to 78.6% and 71.3%, refer to Table 7.

Table 7: LIBS emission discrimination percentages for automobile side mirror – glass side

Emission Line Ratio	F-statistic	90%	99%
Na (285.281)/Si (288.158)	8.1	20.7	15.5
Mg II (280.271)/Sn (283.998)	106.3	39.8	35.1
Si (288.158)/Ca II (317.930)	6.8	15.9	9.8
Fe (373.713)/U II (383.146)	15.7	23.7	18.2
Mg (383.829)/Ca II (396.847)	4.2	11.4	7.0
Cr (390.568)/Nd (393.591)	9.8	16.6	16.4
Fe (393.591)/Ca (422.670)	4.1	7.0	3.7
Mg (518.360)/Ca (558.875)	15.7	20.1	15.2
Fe (559.470)/Na (568.864)	5.6	12.8	6.2
Emission Ratios Only		61.3	51.0
Emission Ratios + RI		77.9	70.1

Brown Container Glass

The ANOVA/Tukey HSD test was used to calculate the discriminating power of this analytical method. Based on the discriminating elemental ratios, 98.1% and 97.1% of the samples could be discriminated without incorporating the RI information at

confidence levels 90% and 99%, respectively (Table 8). With the incorporation of the RI data, 99.0% and 98.1% of the samples could be discriminated.

Table 8: LIBS emission discrimination percentages for brown container glass

Emission Line Ratio	F-statistic	90%	99%
Si (221.806)/Fe II (238.204)	15.0	44.8	41.0
Mg II (279.553)/Na (285.201)	9.9	32.4	21.9
Mg II (280.271)/Mg (285.213)	17.23	48.6	40.0
Na (285.281)/Si (288.158)	396.43	19.0	14.3
Mg (518.360)/Ca (558.876)	377.83	84.8	83.8
Ca (558.876)/Na (588.995)	24.7	50.5	45.7
Ca (616.217)/Cd (643.847)	18.84	53.3	46.7
Si (742.350)/N (746.831)	56.1	56.2	56.2
Na (818.326)/Cl (822.174)	34.8	43.8	41.0
Na (819.479)/Cl (821.204)	14.4	31.4	27.6
Emission Ratios Only		98.1	97.1
Emission Ratios + RI		99.0	98.1

LA-ICP-MS

Automobile Float Glass – Float Side

The raster method was used as the method of analysis for this sample set. Data taken from layer 1 of each glass sample distinguished 100% of the samples at both the 90%

CL and 99% CL, without the addition of the RI data. Evaluation of data taken from layer 2 of the glass samples discriminated 100% of the samples both at the 90% CL and at the 99% CL (Table 9). The sum of the three sets of data (layers 1 – 3) provides a composite data set that reflects the overall composition of the glasses. Using the composite data, at the 90% CL and at the 99% CL, 100% of the samples could be distinguished (Table 9).

The F-statistics obtained from the LA-ICP-MS isotopic ratios are significantly larger than those obtained from the LIBS emission ratios. The F-statistic values gathered from the LIBS analysis of the float glass (float side) sample had a maximum value of 28 (Sn (328.233 nm)/Na (330.237 nm)) while those from the isotopic ratios had a maximum value of 46,083 in one case ($^{27}Al/^{29}Si$) for the analysis of the same sample set. The difference between the F-statistics calculated for analytical method, without the aid of RI, illustrates the precision of the methods.

Table 9: LA-ICP-MS discrimination percentages for layers 1, 2, 3, and composite of all three layers used in sampling automobile float glass – float side. RI data was not included since 100% discrimination was attained for each analysis.

Isotopic Ratio	Layer 1			Layer 2			Layer 3			Sum of 3 Layers		
	F-value	90% CL	99% CL	F-value	90% CL	99% CL	F-value	90% CL	99% CL	F-value	90% CL	99% CL
^{7}Li / ^{53}Cr	109.7	64.4	58.9	240.7	77.9	72.3	182.2	81.0	73.9	229.7	77.5	73.1
^{23}Na / ^{24}Mg	70.6	45.1	41.5	196.6	54.9	48.6	29.6	24.5	24.5	74.2	50.6	43.5
^{27}Al / ^{47}Ti	1,323.3	86.2	83.4	4,276.5	90.1	89.7	3,488.2	89.3	89.3	9,737.2	93.3	92.1
^{27}Al / ^{29}Si	8,165.3	76.3	70.8	21,202.0	74.7	72.7	14,590.0	75.1	70.0	46,083.8	77.1	73.1
^{29}Si / ^{39}K	146.5	87.7	85.4	198.0	91.3	89.7	128.4	88.9	88.1	205.0	93.7	93.3
^{55}Mn / ^{238}U	2,364.5	92.5	91.7	3,195.6	89.3	87.4	3,476.0	86.2	81.0	5,998.9	91.3	89.7
^{57}Fe / ^{55}Mn	996.5	35.6	34.4	830.4	37.2	34.8	222.6	39.5	35.2	843.0	46.2	39.1
^{66}Zn / ^{60}Ni	58.6	64.4	58.5	28.7	52.2	46.2	2.3	4.7	1.4	31.9	54.5	51.4
^{118}Sn / ^{44}Ca	61.0	52.6	44.3	88.7	62.8	57.3	91.9	64.4	62.8	80.1	62.8	55.7
^{232}Th / ^{238}U	163.9	76.3	74.3	109.1	71.5	66.0	86.0	68.8	62.8	292.0	79.4	77.1
Overall Discrimination		100.0	100.0		100.0	100.0		100.0	100.0		100.0	100.0

Headlamp Glass

Instead of performing the LA-ICP-MS rastering method, a drill down method was applied for this sample set. This method was more similar to the LIBS method of analysis. The discrimination for this sample set was significantly lower than previously obtained with other samples. 72.4% and 61.0% of the samples were discriminated at 90% CL and 99% CL, respectively. When the RI data was incorporated, the discrimination percentages increased dramatically to 93.3% and 91.4% at the 90% CL and 99% CL, respectively (

Table 10).

Table 10: LA-ICP-MS isotopic discrimination percentages for headlamp glass

Isotopic Ratio	F-Statistic	90%	99%
^{7}Li / ^{53}Cr	73.4	13.3	13.3
^{137}Ba / ^{140}Ce	251.4	13.3	13.3
^{27}Al / ^{47}Ti	7.2	26.7	14.3
^{57}Fe / ^{55}Mn	5.1	18.1	8.6
^{232}Th / ^{236}U	2.6	3.8	0.0
^{85}Rb /^{232}Th	11.4	13.3	13.3
^{88}Sr /^{90}Zr	23.0	5.7	0.0
^{139}La /^{178}Hf	8.5	26.7	15.2
^{27}Al / ^{29}Si	6.1	24.8	24.8
Isotopic Ratios Only		72.4	61.0
Isotopic Ratios + RI		93.3	91.4

Side Mirror Glass

LA-ICP-MS was used to analyze the glass side of the side mirror glass samples (Table 11) by the ANOVA/Tukey HSD test. The raster method was used as the analytical method of analysis. The overall discrimination achieved by this technique was significantly higher than the LIBS and RI discrimination percentages. By encompassing the three layers of analysis, overall 100% of the samples were discriminated by isotopic ratios alone at the confidence level of 90%. When the confidence level increased to 99%, the discrimination percentage decreased to 99.8% with RI and 99.6% without RI.

Table 11: LA-ICP-MS discrimination percentages for Layers 1, 2, 3, and composite of all three layers used in sampling side mirror glass

Isotopic Ratio	Layer 1			Layer 2			Layer 3			3 Layers Summed		
	F-value	90% CL	99% CL	F-value	90% CL	99% CL	F-value	90% CL	99% CL	F-value	90% CL	99% CL
^{7}Li / ^{53}Cr	128.5	62.9	58.3	136.7	70.8	66.7	131.9	71.7	67.7	234.1	72.4	69.2
^{23}Na / ^{24}Mg	6.8	5.9	5.9	20.1	28.5	21.6	97.3	64.0	56.7	136.4	69.5	64.7
^{27}Al / ^{47}Ti	724.1	70.0	66.1	710.0	70.2	66.1	650.3	68.8	65.4	2507.4	81.8	79.3
^{29}Si / ^{39}K	110.3	62.6	60.6	558.8	81.3	78.6	866.5	84.5	81.8	278.1	73.8	69.5
^{55}Mn / ^{238}U	30.0	5.9	5.9	77.7	52.4	45.3	389.9	80.0	75.4	125.6	68.1	63.1
^{57}Fe / ^{55}Mn	564.0	67.0	61.8	1145.5	69.9	67.2	1087.0	71.8	69.5	4653.2	83.6	80.8
^{66}Zn / ^{60}Ni	22.7	43.3	33.7	18.4	41.7	36.0	2.07	3.7	1.4	13.6	34.6	26.7
^{118}Sn / ^{44}Ca	677.9	83.4	81.6	413.2	80.8	76.8	531.6	82.4	80.4	706.8	84.1	81.6
^{232}Th / ^{238}U	24.2	36.5	32.1	30.8	36.5	31.4	185.2	59.7	55.0	102.1	53.8	47.6
^{27}Al / ^{29}Si	670.1	75.2	72.0	1013.0	80.6	77.0	827.3	77.7	74.0	1224.9	81.3	77.5
Isotopic Only		99.3	98.6		99.5	99.3		99.8	99.3		100.0	99.6
Isotopic + RI		99.5	98.8		99.5	99.3		99.8	99.5		N/A	99.8

XRF

Automobile Float Glass – Float Side

The automobile float glass (float side) was discrimination by ANOVA/Tukey HSD analysis using XRF emission ratios. Discrimination emission ratios were created from the 26 emission peaks. From these peaks, discriminating ratios were chosen as to provide maximum discrimination with minimal correlation between the emission ratios. For this sample set, 90.9% of the samples could be discriminated at the 90% CL and at the 99% CL, 85.8% of the samples were discriminated. If this information is used in conjunction with the experimental RI data described above, 99.2% and 98.8% can be discriminated at the 90% CL and the 99% CL, respectively (Table 12).

Table 12: XRF emission discrimination percentages for automobile float glass – float side

Emission Line Ratios	F-value	90%	99%
Na K/Mg K	2.86	3.95	1.19
K K/Ca K	96.17	66.01	57.31
Ti K/Cr K	25.45	30.43	30.43
Rb K/Sr K	4.11	8.30	5.53
Sr K/Zr K	70.58	50.99	41.90
Al K/Mn K	4.31	7.51	1.58
Sc K/Co K	3.70	7.91	5.53
Zn K/Cd K	1.77	0.39	0.00
Emission Ratios Only		90.9	85.8
Emission Ratios + M. RI		98.8	98.8

Headlamp Glass

The discrimination obtained with XRF alone was lower than that obtained by LIBS or LA-ICP-MS by the ANOVA/Tukey HSD test. The F-statistics calculated for these discrimination ratios were less the 40, which is significantly lower than the F-statistic values for the LA-ICP-MS isotopic ratios and similar to the F- statistic values for the LIBS elemental ratios. At the 90% CL, 68.6% of the samples could be discriminated based on XRF measurements alone. With the RI data, this discrimination value increased to 91.4%. At the 99% CL, 88.6% and 67.6% of the pairwise comparisons

were deemed to be from different sources, with and without RI data, respectively (Table 13).

Table 13: XRF emission discrimination percentages for headlamp glass

Emission Line Ratio	F-value	90%	99%
Al K/Si K	15.6	29.5	22.9
K K/Ca K	49.3	13.3	13.3
Na K/Cu K	1.8	1.0	0.0
Na K/Al K	3.2	3.8	0.0
Sr K/Zr K	14.5	15.2	13.3
Si K/Ca K	13.8	28.6	22.9
Zr K/Rb K	37.6	55.2	53.3
Emission Ratios Only		68.6	67.6
Emission Ratios + RI		91.4	88.6

Side Mirror Glass

The reflective side of the side mirror was analyzed by XRF (Table 14). The F-statistic of the discriminating ratios chosen for this discrimination ranged from 2 to 1,115. The elemental ratio that had a F-statistic of 2 (Zr K/Cd K) only discriminated 2% at the 90% CL and did not discriminate at the 99% CL; whereas, the ratio with a F-statistic of 1,115 (Cr K/Fe K) discriminated 90.6% and 87.7% at the 90% CL and the 99% CL, refer to Table 14. Ten discriminating ratios differentiated 98.8% of the samples at the 90% CL

and 97.9% at a 99% CL. There was a slight increase in discrimination, 98.9% and 98.0% respectively at the 90% CL and the 99% CL with the addition of The RI data.

The non-coated glass side of the side mirror was analyzed by XRF as well (Table 15). The F-statistic values were significantly lower than those calculated for the deposit side of the mirror. The F-statistics ranged from 2 to 73. Using the XRF discrimination ratios alone, at the 90% and the 99% CL, 80.6% and 71.0% was differentiated. The overall discrimination of XRF + RI was lower for the deposit side, the discriminating power for this side of the glass was 90.6% and 83.1% at the 90% CL and 99% CL, respectively.

Table 14: XRF emission discrimination percentages for automobile side mirror – deposit side

Emission Line Ratio	F-value	90%	99%
Na K/Mg K	30.13	39.04	30.12
Ma K/Al K	140.62	73.62	69.16
Si K/Ca K	142.4	68.09	62.74
K K/Ti K	122.08	51.16	44.74
Cr K/Fe K	1115.64	90.55	87.70
Mn K/ Co K	6.78	12.66	10.52
Ni K/Cu K	6.44	5.88	5.88
Rb K/Sr K	3.70	6.42	4.64
Sr K/Zr K	82.93	48.66	40.82
Zr K/Cd K	2.31	1.96	0.00
Emission Ratios Only		98.75	97.86
Emission Ratios + RI		98.93	98.04

Table 15: XRF emission discrimination percentages for automobile side mirror – non coated glass side

Emission Line Ratio	F-value	90%	99%
Na K/Mg K	5.77	8.20	5.88
Ma K/Al K	16.59	39.39	28.34
Si K/Ca K	1.086	5.17	0.18
K K/Ti K	13.84	35.12	28.70
Cr K/Fe K	16.86	21.57	21.39
Mn K/ Co K	3.10	5.70	5.70
As L/Rb K	2.66	5.35	4.28
Rb K/Sr K	11.43	17.47	11.94
Sr K/Zr K	73.74	38.15	29.77
Zr K/Cd K	4.02	7.12	3.39
Emission Ratios Only		80.57	70.94
Emission Ratios + RI		90.55	83.07

Brown Container Glass

One hundred percent of the brown container glasses were discriminated from one another at both the 90% and the 99% confidence levels. The F-statistics calculated for the discrimination ratios ranged from 11 to 3,700. The discrimination ratio that had a F-statistic of 3,700 (K K/Ca K) was able to discriminate 95.2% of the samples at the 90% CL, refer to Table 16.

Table 16: XRF emission discrimination percentages for brown container glass

Emission Line Ratio	F-value	90%	99%
Na K/Mg K	11.56	38.10	29.52
Al K/Si K	30.10	38.10	34.29
K K/Ca K	3,700.03	95.24	91.43
Ti K/Cr K	16.18	41.91	27.62
Ca K/Fe K	2,041.76	94.286	91.43
Cu K/Zn K	11.15	13.33	13.33
Rb K/Sr K	56.02	41.91	33.33
Sr K/Zr K	166.79	84.76	80.00
Si K/Ca K	71.61	60.95	53.33
Al K/Mn K	11.98	13.33	13.33
Emission Ratios Only		100.00	100.00

Student's t-Test Data Analysis

HQI Discrimination

The hit quality index (HQI) is based on the cosine of the angle between two spectra (vectors), i.e. a questioned and a known spectrum. The spectra were normalized to the most intense peak in the spectrum. The HQI is calculated from the dot product between spectra A and spectra B, refer to equation 26. If the two spectra are similar, HQI is close to 0; if the spectra are dissimilar, HQI approaches $\sqrt{2}$.

$$HQI = \sqrt{2} \times \left[\sqrt{1 - \frac{(a \bullet b)}{\sqrt{a \bullet a}\sqrt{b \bullet b}}} \right] \quad \textbf{(26)}$$

XRF

Automobile Float Glass – Float Side

This method was used for full spectral discrimination of the XRF spectra. This method alone provided a slightly higher discrimination percentage at both the 90% CL and the 99% CL than the ANOVA/Tukey HSD analysis method. The spectral emission recorded ranged from 0 – 40.2 keV. However, most of this area (10 – 40 keV) is comprised of noise from the baseline, refer to Figure 13. When the spectral range used for comparison was shortened to the unique area of the spectral emission, the overall discrimination increased. It is necessary to note that the peaks centered around 20 keV are present in every sample and were removed when the spectral range is limited to 0 – 10 keV.

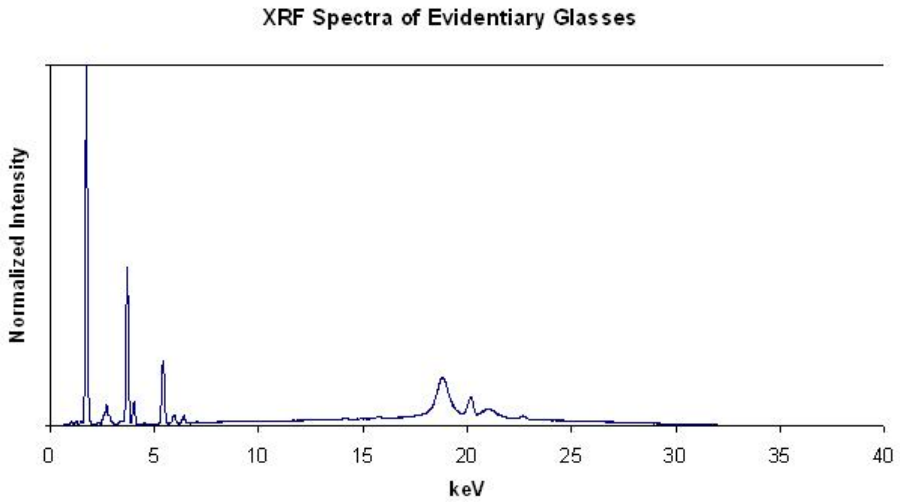

Figure 13: Representative XRF glass spectra

Using a limited spectral region, approximately 80% of the 253 pair-wise comparisons can be discriminated. Incorporating the RI data with the XRF data, the discriminating power of this method increases dramatically to 99.6% at both a 90% and a 99% confidence level.

Table 17: XRF discrimination percentages of automobile float glass – float side

Energy Range (keV)	XRF Alone		XRF + RI	
	90% CL	99% CL	90% CL	99% CL
0 - 40.2	68.4	58.1	99.2	98.8
0.8 – 25.1	68.8	59.3	99.6	98.8
0.8 – 10.0	81.8	79.0	99.6	99.6

Headlamp Glass

Using the Student's *t-test* alone to discriminate the XRF full spectra, 84.8% and 76.2% of the headlamp samples could be discriminated at the 90% CL and the 99% CL when the spectral region of comparison was limited to 0.8 – 10.0 keV (Table 18). The discrimination increased with the addition of the RI data to 94.3% at the 90% CL and 92.4% at the 99% CL.

Table 18: XRF discrimination percentages of headlamp glass

Energy Range (keV)	XRF Alone		XRF + RI	
	90% CL	99% CL	90% CL	99% CL
0 - 40.2	70.48	61.90	95.24	92.38
0.8 – 25.1	70.48	61.90	95.24	92.38
0.8 – 10.0	84.76	76.19	94.29	92.38

Side Mirror Glass

This method was employed for spectral discrimination of the deposit side and the glass side of automobile side mirror. A limited spectral region was used for comparison, this ranged 0.8 – 10.0 keV. Higher discrimination was achieved for the deposit side of the mirror analysis, refer to Table 19.

Table 19: XRF full spectral analysis (0.8 0 10.0 keV) of the deposit and the glass side of automobile side mirrors

Side Analyzed	XRF Alone		XRF + RI	
	90% CL	99% CL	90% CL	99% CL
Deposit	93.94	91.09	96.08	94.47
Glass	91.62	86.99	94.29	90.37

Brown Container Glass

Using the full spectral Student's *t*-test for this sample set, significantly lower discrimination percentages were obtained. Only 53.3% and 31.4% of the sample could be discriminated at the 90% CL and the 99% CL if the entire spectrum was retained for comparison. The discrimination percentages increased dramatically once the spectral region shortened to include only the elemental emissions from the sample (0.8 – 10 keV). The percentages increased to 95.2% and 88.6% at the both the 90% and 99% confidence levels, respectively.

Table 20: XRF full spectral discrimination of brown container glass

Energy Range (keV)	XRF Alone		XRF + RI	
	90% CL	99% CL	90% CL	99% CL
0 – 40.2	53.33	31.43	87.62	78.10
0.8 – 25.1	53.33	31.43	87.62	78.10
0.8 – 10.0	95.23	88.57	98.10	94.29

Sorenson Discrimination

Automobile float glasses (float side) were analyzed by the Sorenson discrimination method. In the Sorenson equation, the metric is denoted as P. This equation counts the number of peaks that are the same in the two spectra being compared, multiplies the number of common peaks by two and divides the product by the total number of peaks in both spectra. This value, P, provides a quantitative comparison of the spectra. If the spectra are similar, P will approach 1; if the spectra are dissimilar, P will approach 0.[90]

$$P = \frac{2(n_a \cup n_b)}{n_a + n_b} \qquad \textbf{(27)}$$

Automobile Float Glass – Float Side

A sample set that consisted of 15 glass sample (105 pairwise comparisons), was analyzed by this method. Each glass samples was analyzed at 5 different positions on the surface of the glass in order to calculate the variance between replicate measurements on the same samples and different samples. This method allowed for 90.5% discrimination at the 90% CL and at the 99% CL 76.2% were discriminated.

Linear Discrimination

Pearson Correlation Coefficient

Full Spectral Correlation

Sample discrimination of automobile float glass (float side) was attempted by full spectral Pearson correlation. This correlation utilizes all data points, including baseline points. The correlation can be residual by plotting the intensities from each channel in spectrum A against the intensities from spectrum B. This analysis was performed on two comparisons of LIBS glass spectra and the results are illustrated in Figure 14 and Figure 15. One of the comparisons is of two glass samples that could be discriminated by elemental ratios and RI (Figure 14), while the other comparison was between two glass samples that could not be discriminated by elemental ratios or RI (Figure 15). The pairwise comparison illustrated in Figure 14 was previously discriminated by six different elemental ratios. The coefficient (r) values for both plots were similar. This method was insufficient for discrimination, which is attributed to the heavy weighting of the linear correlation by the points in the baseline, which generally leads to high coefficient values ($r > 0.9$) for comparisons between the same sample or different samples. Included in the points plotted are the points located on the sides of the peak which may provide broadening information and characterize the plasma itself, but there is no discriminating information offered for the pairwise comparison.

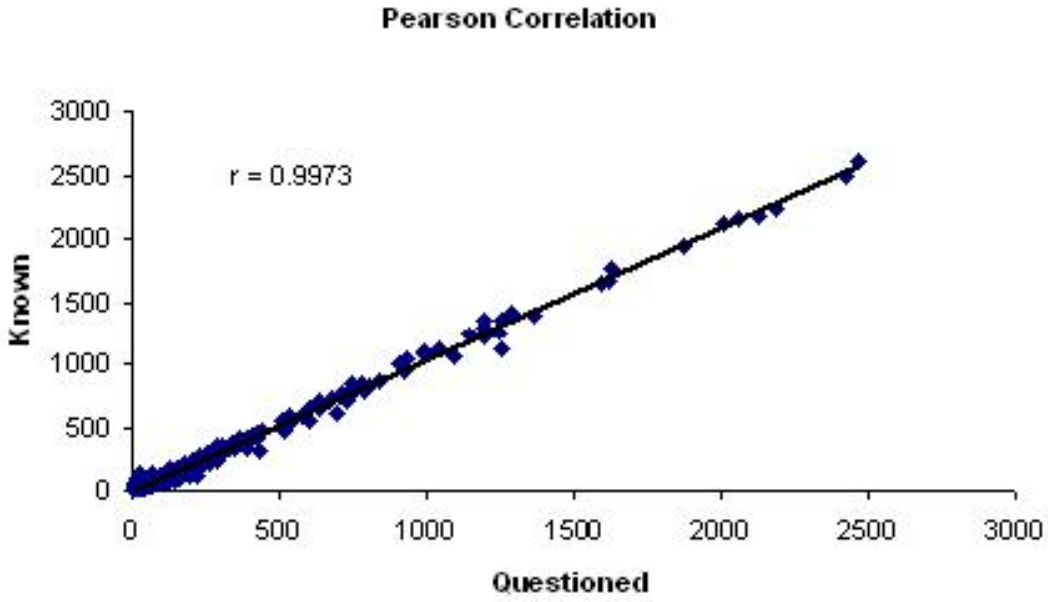

Figure 14: Discriminated pairwise comparisons analyzed by full spectral Pearson correlation

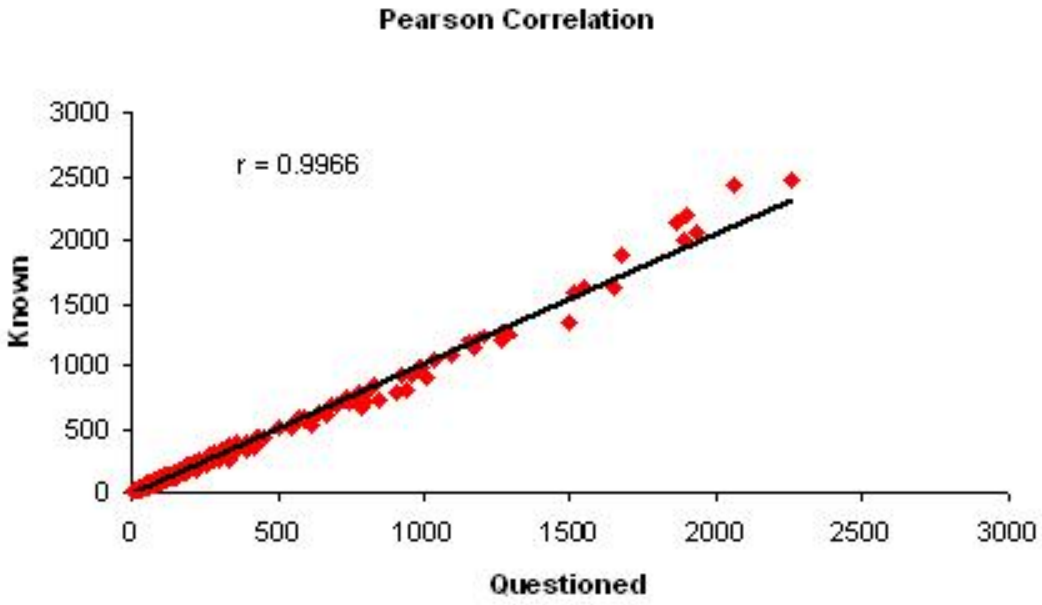

Figure 15: Not discriminated pairwise comparison analyzed by full spectral Pearson correlation

Isolated Peak Correlation

Due to the issues described above regarding the influence of the baseline on the correlation, peaks with a S:N > 3:1 were identified and plotted against each other to determine if any discriminating information could be obtained. In this method, if the peak was present in one spectrum and not in the other ("absent peaks"), it was not included in the plot. This avoids using missing information to aid discrimination. While two samples can be considered different of one has a peak and the other does not, there is no concrete determination to say that sample B does not possess the same peak but at a concentration lower than the limit of detection. The same pairwise comparisons analyzed in the previous section, where analyzed by this method as well. The isolated peak Pearson correlation plots are illustrated in Figure 16 and Figure 17. The coefficient values calculated for the two pairwise comparisons were both greater than 0.99, which is too similar to make any determination about the discrimination.

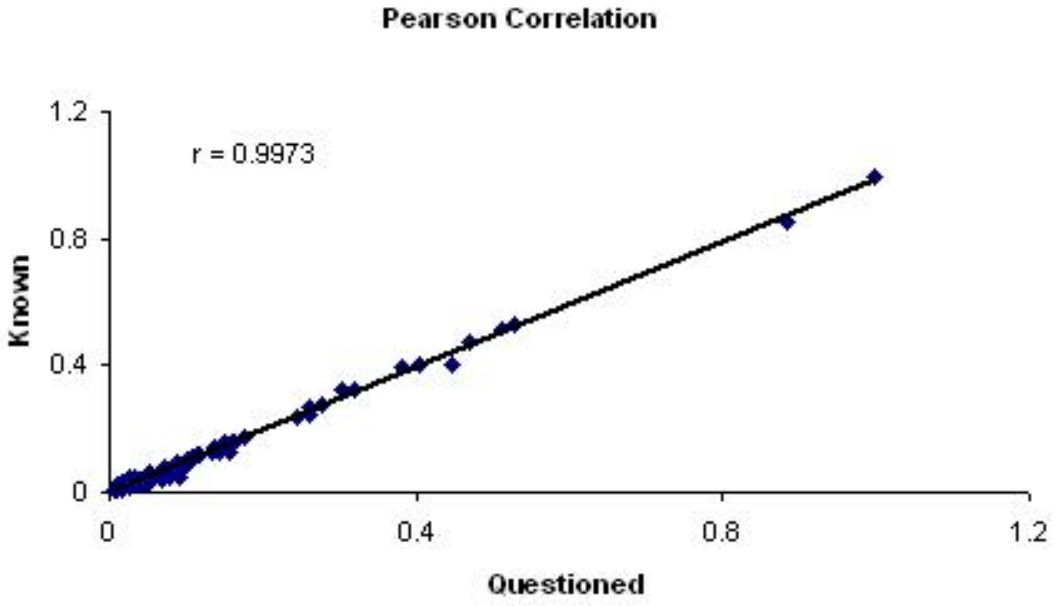

Figure 16: Discriminated pairwise comparisons analyzed by isolated peak Pearson correlation

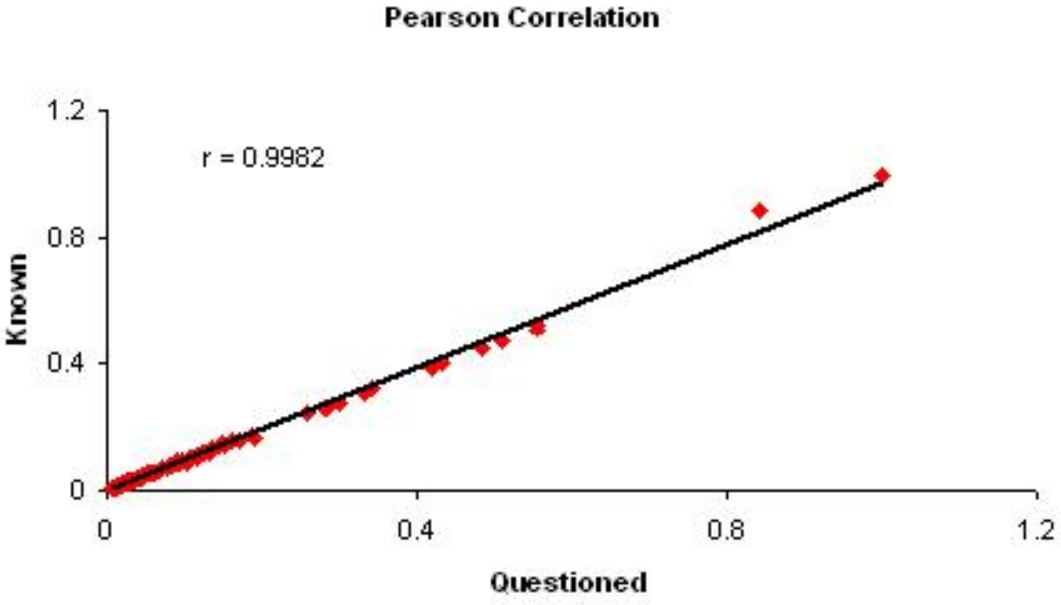

Figure 17: Not discriminated pairwise comparison analyzed by isolated peak Pearson correlation

A larger sample set, consisting of the same 15 samples analyzed by the Sorenson method of discrimination, was subjected to discrimination by the isolate peak Pearson analysis. This analytical method provided 29.5% discrimination at the 90% CL, which is significantly lower than the 90.5% discrimination obtained with the Sorenson analysis. At the 99% CL, 5.7% of the samples could be discriminated. This discriminating power is significantly lower than those obtained with the other discrimination methods and is due to the extreme similarity of the peak intensities in the known and unknown sample being compared.

Rank Correlation

The discriminated sample pair and the non-discriminated sample pair, presented in the previous sections were analyzed by rank correlation of the intensities of the identified peaks. The correlation is based on the intensity of peaks identified with a S:N > 3:1 and uses only the peaks that are present in both spectra. The rank correlation of the discriminated pair is illustrated in Figure 18. This plot shows a high degree of scattering about the best fit line. The rank correlation plot displayed in Figure 19 for the pair that was not previously discriminated by the ANOVA/Tukey HSD method and RI shows much less scatter. The correlation of the discriminated pair is much lower than the non-discriminated pair which illustrates the differences between the two samples compared.

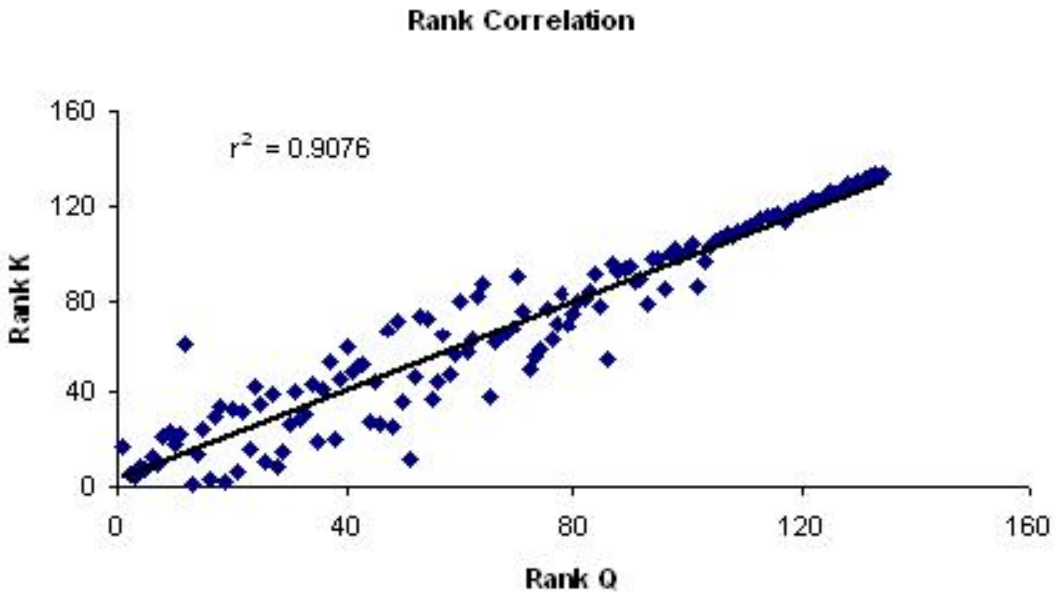

Figure 18: Discriminated pairwise comparison analyzed by isolated peak rank correlation

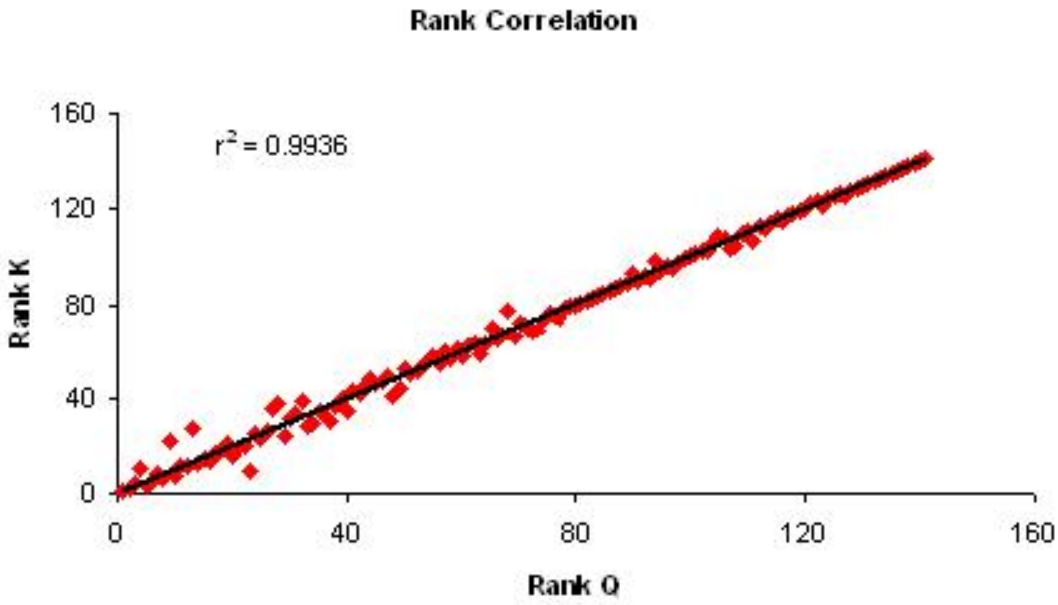

Figure 19: Not discriminated pairwise comparison analyzed by isolated peak rank correlation

The set of 15 samples analyzed by the Sorenson method and the Pearson correlation method was analyzed by the rank correlation method. In this discrimination study, 92.4% of the samples could be discriminated at the 90% CL and 83.8% of the samples were discriminated at the 99% CL.

Confidence Interval Discrimination

Full Spectral Discrimination

Full spectral discrimination of glass samples were analyzed by calculating the confidence intervals of the peaks in the known and unknown spectra. Only peaks with a S:N greater than three and are present in both spectra are utilized in this comparison. The intensity difference was calculated for each peak compared and the ten peaks with the largest difference were used for discrimination. The confidence intervals were then calculated for the peaks in spectra A and spectra B, if the intervals overlap then the pair was not discriminated by this peak. If the peaks do not overlap than the pair is discriminated.

Six comparisons were tested using this analytical method: three comparisons that were previously discriminated by elemental ratios and three comparisons that were not previously discriminated by the ANOVA/Tukey HSD analysis (Table 21). For this analysis, the spectral region analyzed was from 200 – 800 nm. The spectral region from 800 – 900 nm was not included in this discrimination in order to omitted peaks

associated with air atmospheric emission. Peaks having a S:N > 3:1 were included in the discrimination calculation.

Table 21 presents a comparison of the full spectral confidence interval analysis to the ANOVA/Tukey HSD analysis. There were 10 discriminating peaks with the largest difference in intensity identified for each comparison. However, these peaks were not able to discriminate the known and unknown samples based on the confidence interval. Absent peaks are defined as peaks present in one of the two spectra. The number of "absent peaks" provides supplemental information; generally comparisons that were discriminated have a high number of "absent peaks" which illustrates the difference between the known and the unknown sample. When the comparison can not be discriminated, there is usually a low number of absent peaks. The number of elemental ratios that could discriminate the comparison via ANOVA/Tukey HSD analysis is presented to illustrate the discriminating power of this analysis.

Table 21: Full spectral confidence interval discrimination of automobile float glass (float side) samples that were previously analyzed by the ANOVA/Tukey HSD method at a 95% CL

Known	Unknown	Peaks Identified	Discriminating Peaks	"Absent Peaks"	Discriminating Elemental Ratios
Explorer	Escort	10	0	31	1
Saturn	Avenger	10	0	60	3
Mazda	C1500	10	0	88	6
Escort	Mazda	10	0	0	0
Eclipse	Concord	10	0	55	0
Prism	Intrepid	10	0	49	0

The results presented in Table 21, illustrates that there is no discrimination obtained by the full spectral confidence interval method of analysis. Samples previously discriminated by the ANOVA/Tukey HSD analysis and had a high number of absent peaks was not discriminated by the full spectral confidence interval analysis.

Sub-spectral Discrimination

Better discrimination was attained if the spectra were broken up into spectral ranges (~250 nm). Only peaks with a S:N ratio greater than three were used in the analysis. The peaks with the highest difference in intensities are usually the most intense peaks and not necessarily the most discriminating. Less intense peaks, which can be unique to the samples, are not considered when used the full spectrum. By limiting the spectral range, differences in the less intense peaks can be included for discrimination.

This may lead to better discrimination of the pairwise comparisons. Only the spectral region from 200 nm – 650 nm was included in the discrimination. This was done to remove any influence of atmospheric peaks, located in the 650 nm – 900 nm spectral region. Each matrix comparison was evaluated at the 99% CL so that the Bonferonni correction could be utilized and give an overall confidence level of 98% CL for the total matrix.

Automobile Float Glass – Float Side

The following set of four matrices illustrates the sub-spectral analytical method of confidence interval discrimination. Each matrix results from spectral comparisons of 250 nm ranges.

Ten Comparisons of Pairs with the Largest Difference between the Average Means

Spectral Range: 200 - 450 nm

	Grandam	Caprice 89	Caprice 90	Escort	Mazda 626	Corolla	Neon	Mustang
Grandam								
Caprice 89	3							
Caprice 90	2	0						% Discriminated
Escort	1	0	0					75.00
Mazda 626	1	0	2	0				
Corolla	6	3	4	2	4			
Neon	0	3	1	2	1	5		
Mustang	0	4	6	1	1	7	5	

Spectral Range: 450 - 650 nm

	Grandam	Caprice 89	Caprice 90	Escort	Mazda 626	Corolla	Neon	Mustang
Grandam								
Caprice 89	0							
Caprice 90	1	0						% Discriminated
Escort	0	0	0					21.43
Mazda 626	0	0	0	0				
Corolla	0	0	0	0	0			
Neon	2	0	0	0	0	2		
Mustang	0	0	1	0	0	1	1	

Figure 20: Discrimination sub-matrices of automobile float glass – float side based on confidence intervals

For the total discrimination matrices (Figure 21), the first matrix entries represents the number of comparisons were able to discriminate the pairwise comparison by the two matrices in Figure 20. The second matrix in Figure 21, illustrates how many peaks were in one of the two spectra, which is referred to as "absent peaks". Whereas, with the ANOVA/Tukey method, 96.4% of the samples could be discriminated, only 78.57% were differentiated with this method of analysis.

Total Discrimination - Sub Matrices Added

	Grandam	Caprice 89	Caprice 90	Escort	Mazda 626	Corolla	Neon	Mustang
Grandam								
Caprice 89	3							
Caprice 90	3	0						% Discriminated
Escort	1	0	0					78.57
Mazda 626	1	0	2	0				
Corolla	6	3	4	2	4			
Neon	2	3	1	2	1	7		
Mustang	0	4	7	1	1	8	6	

Peaks Present in Only One of the Two Spectra ("Absent Peaks")

	Grandam	Caprice 89	Caprice 90	Escort	Mazda 626	Corolla	Neon	Mustang
Grandam								
Caprice 89	17							
Caprice 90	28	19						
Escort	26	13	30					
Mazda 626	23	10	27	3				
Corolla	21	18	36	23	22			
Neon	20	35	46	44	41	39		
Mustang	17	18	59	17	14	22	35	

Figure 21: Overall discrimination matrices based on confidence intervals for automobile float glass – float side

Brown Container Glass

Analysis of brown container glass by the sub-spectral confidence interval method, allows for 85.7% discrimination of these pairwise comparisons based on the first sub-spectral region. This discrimination is enhanced by the 57.1% discrimination obtained in the second sun-spectral region at a confidence level of 99% (Figure 22).

Ten Comparisons of Pairs with the Largest Difference between the Average Means

Spectral Range: 200 - 450 nm

	Abita	Bud Light	Bud Select	Dos Equis	Guiness	Miller 1	Miller 2	Scrimshaw
Abita								
Bud Light	5							
Bud Select	2	9						% Discriminated
Dos Equis	9	1	9					85.71
Guiness	10	3	9	3				
Miller 1	7	0	9	9	8			
Miller 2	2	0	2	9	9	2		
Scrimshaw	8	0	9	3	0	10	10	

Spectral Range: 450 - 650 nm

	Abita	Bud Light	Bud Select	Dos Equis	Guiness	Miller 1	Miller 2	Scrimshaw
Abita								
Bud Light	1							
Bud Select	0	0						% Discriminated
Dos Equis	3	0	2					57.14
Guiness	4	1	3	0				
Miller 1	1	0	0	3	3			
Miller 2	0	2	0	3	3	0		
Scrimshaw	4	0	2	0	0	3	3	

Figure 22: Discrimination sub-matrices of brown container glass based on confidence intervals

For comparative purposes, this same sample set was discriminated by the ANOVA/Tukey test where 100% of these samples could be discriminated compared to the 89.3% discriminated by the confidence interval method (Figure 23).

Total Discrimination - Sub Matrices Added

	Abita	Bud Light	Bud Select	Dos Equis	Guiness	Miller 1	Miller 2	Scrimshaw
Abita								
Bud Light	6							
Bud Select	2	9						% Discriminated
Dos Equis	12	1	11					89.29
Guiness	14	4	12	3				
Miller 1	8	0	9	12	11			
Miller 2	2	2	2	12	12	2		
Scrimshaw	12	0	11	3	0	13	13	

Peaks Present in Only One of the Two Spectra ("Absent Peaks")

	Abita	Bud Light	Bud Select	Dos Equis	Guiness	Miller 1	Miller 2	Scrimshaw
Abita								
Bud Light	12							
Bud Select	2	14						
Dos Equis	40	30	42					
Guiness	25	19	27	19				
Miller 1	7	7	9	37	22			
Miller 2	8	12	10	42	25	5		
Scrimshaw	32	24	34	10	13	31	34	

Figure 23: Overall discrimination matrices based on confidence intervals for brown container glass

Headlamp Glass

Based on the discrimination within the first sub-spectral region (220 – 450 nm) 82.1% of the samples could be discriminated. In the second sub-spectral region (450 – 650 nm) only 57.1 % could be differentiated, refer to Figure 24.

Ten Comparisons of Pairs with the Largest Difference between the Average Means

Spectral Range: 200 - 450 nm

	Grandam	Caprice 89	Caprice 90	Escort	Mazda 626	Corolla	Neon	Mustang
Grandam								
Caprice 89	7							
Caprice 90	8	8						% Discriminated
Escort	0	7	10					82.14
Mazda 626	4	7	10	9				
Corolla	6	7	6	10	0			
Neon	2	7	9	9	0	0		
Mustang	8	8	10	10	8	0	3	

Spectral Range: 450 - 650 nm

	Grandam	Caprice 89	Caprice 90	Escort	Mazda 626	Corolla	Neon	Mustang
Grandam								
Caprice 89	0							
Caprice 90	0	1						% Discriminated
Escort	0	1	2					57.14
Mazda 626	0	1	0	2				
Corolla	0	1	0	2	0			
Neon	0	1	2	2	2	2		
Mustang	0	1	2	2	0	0	2	

Figure 24: Discrimination by sub-matrices of headlamp glass based on confidence intervals

When these two regions are summed, 89.3% can be discriminated at an overall confidence level of 98% with this analysis (Figure 25). In comparison to the ANOVA/Tukey method, this method had a lower discrimination percentage. Using the ANOVA/Tukey method all of the samples could be discriminated.

Total Discrimination - Sub Matrices Added

	Grandam	Caprice 89	Caprice 90	Escort	Mazda 626	Corolla	Neon	Mustang
Grandam								
Caprice 89	7							
Caprice 90	8	9						% Discriminated
Escort	0	8	12					89.29
Mazda 626	4	8	10	11				
Corolla	6	8	6	12	0			
Neon	2	8	11	11	2	2		
Mustang	8	9	12	12	8	0	5	

Peaks Present in Only One of the Two Spectra ("Absent Peaks")

	Grandam	Caprice 89	Caprice 90	Escort	Mazda 626	Corolla	Neon	Mustang
Grandam								
Caprice 89	28							
Caprice 90	56	82						
Escort	4	32	56					
Mazda 626	56	80	10	54				
Corolla	15	43	10	11	43			
Neon	16	44	58	12	46	5		
Mustang	17	29	68	19	61	24	25	

Figure 25: Overall discrimination matrices based on confidence intervals for headlamp glass

Data Retrieval based on the HQI Calculation

LIBS

The utility of a library search is immeasurable in a forensic laboratory setting. The ROC plots were used to determine how specific this method of analysis is with respect to cataloging and generating a library for comparison based on HQI values. To test the utility of this discrimination, one LIBS spectrum from an automobile float glass (float side) car 1 was placed into a library (spectra a) and two replicate spectra from the same car were used to search against the library (spectra b). The HQI values were calculated for each comparison and these values were used to generate the ROC curve presented in Figure 26. The area under the curve was 0.73, this means that there is 73% probability of recovering the correct match at an HQI value lower than an incorrect match. The area achieved by this comparison is neither an ideal area nor an area that would be appropriate for developing a library for comparison. The poor sensitivity of this discrimination may be due to a high variance of back-to-back single shot spectra collected per sample or due to the high similarity of individual glass samples within the sample glass type.

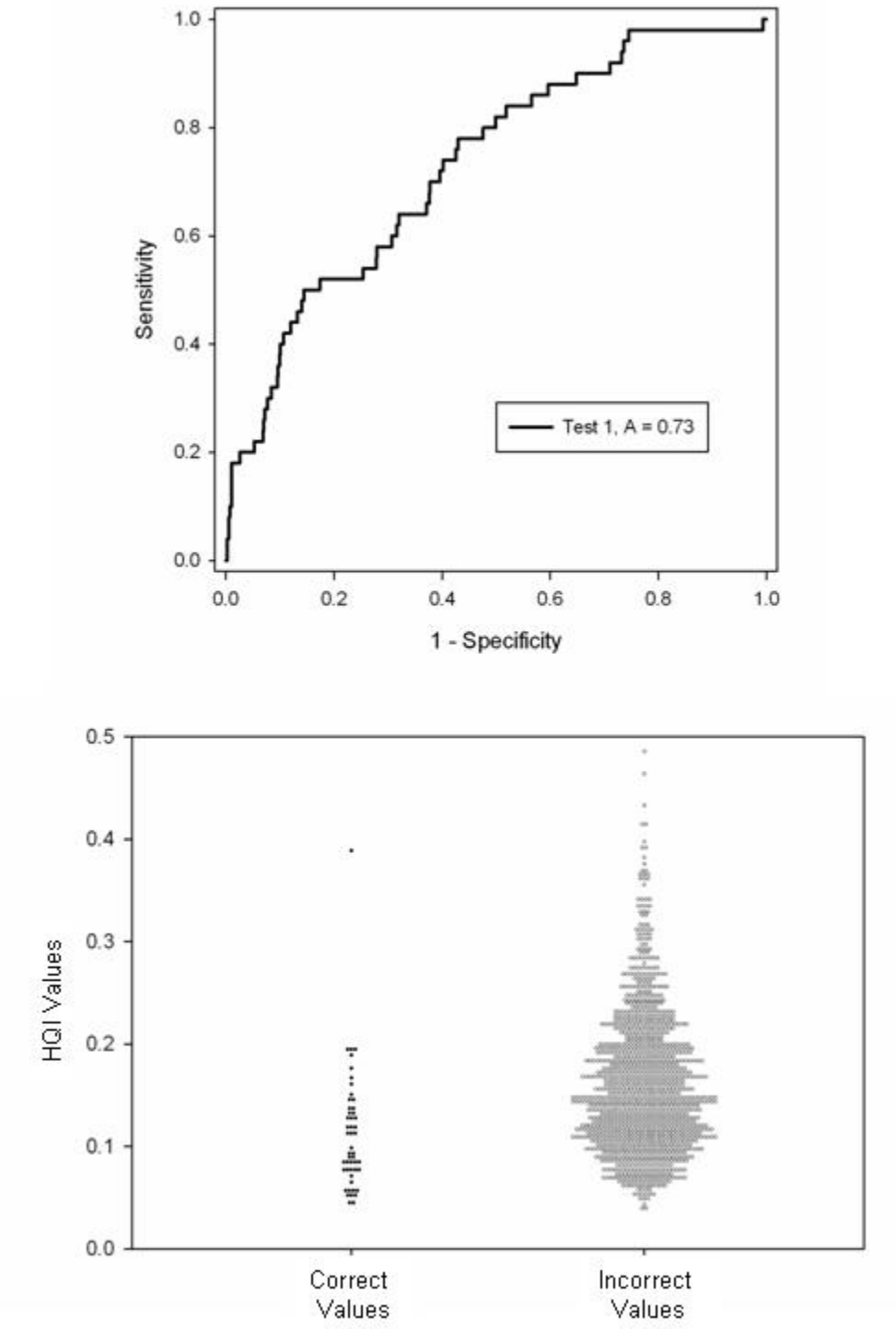

Figure 26: ROC plot and a dot histogram of the LIBS Student's *t*-test/HQI comparison of the automobile float glass – float side samples

Discrimination between Glass Types

Discrimination of glass samples of the same type via the full LIBS spectra was quite difficult due to the high degree of similarity of the glasses (refer to Figure 12). Therefore, full spectral discrimination between different types of glass samples was attempted. Visually, the spectra are quite different which should lead to PCA grouping or clustering (Figure 27).

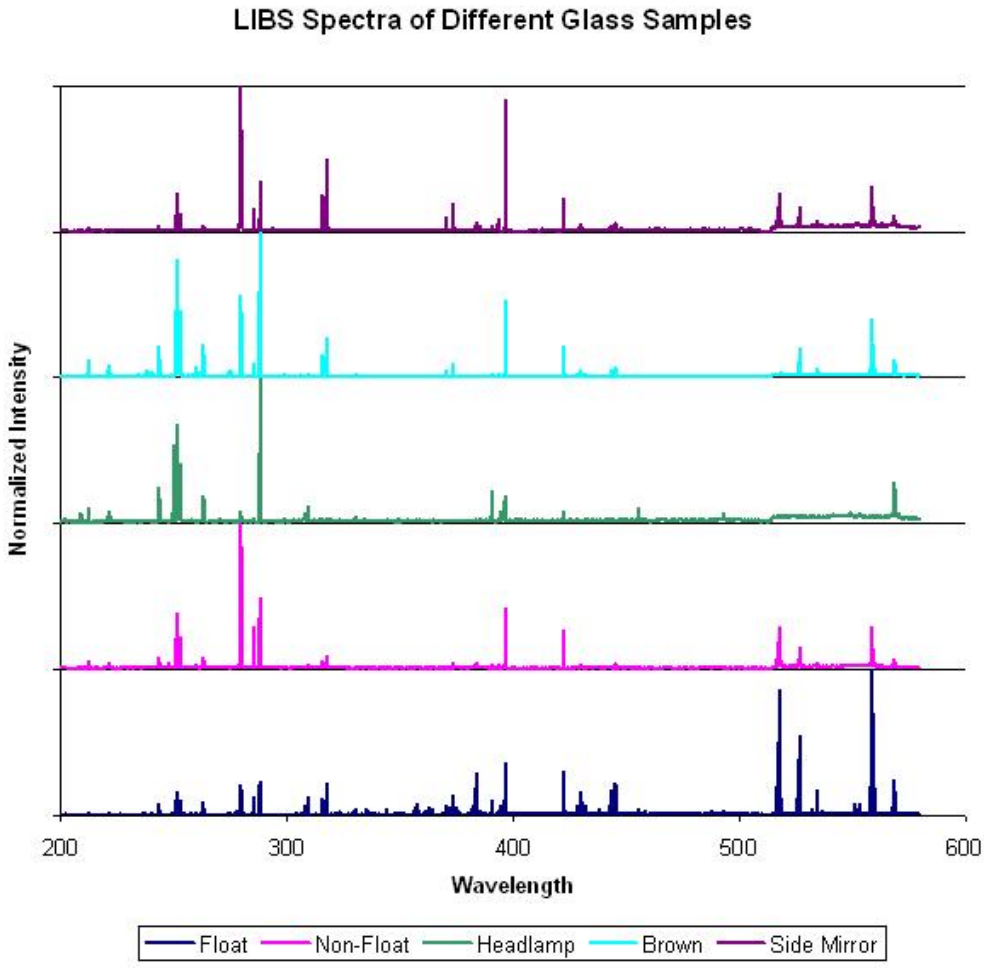

Figure 27: An illustration of LIBS spectra from different types of glass

PCA Groupings

Principal component analysis was examined as a rapid full spectral classification technique for different glass types. By reducing the variance in the spectra to their principal components groups of similar types of glasses was observed. The 3-D PCA (PC1, PC2 and PC3) plot is illustrated in Figure 28. This plot is comprised of ten spectra from different samples within each type of glass. There is significant overlap between the side mirror, automobile (float side) and the automobile (non float side) samples, which are all float glasses. Of the glass types examined, the headlamp spectra were the most different. While float glass and the drinking glass are soda-lime-silicate, headlamp glasses are generally borosilicate and may also be a soda-lime-silicate.[86]

PCA was performed using the glass spectrum from 200 nm – 514 nm. The area from 515 nm to 900 nm was omitted to prevent any influence from atmospheric emissions. Representative spectra of the distinct groups are illustrated in Figure 28 to illustrate how dissimilar these spectra are, the sodium peaks and atmospheric peaks are illustrated. Utilizing the peaks with a S:N greater than 3, rather than using the full spectrum, was evaluated by PCA for grouping of the types of glasses. However, more distinct groups were not evident using the peak intensities only.

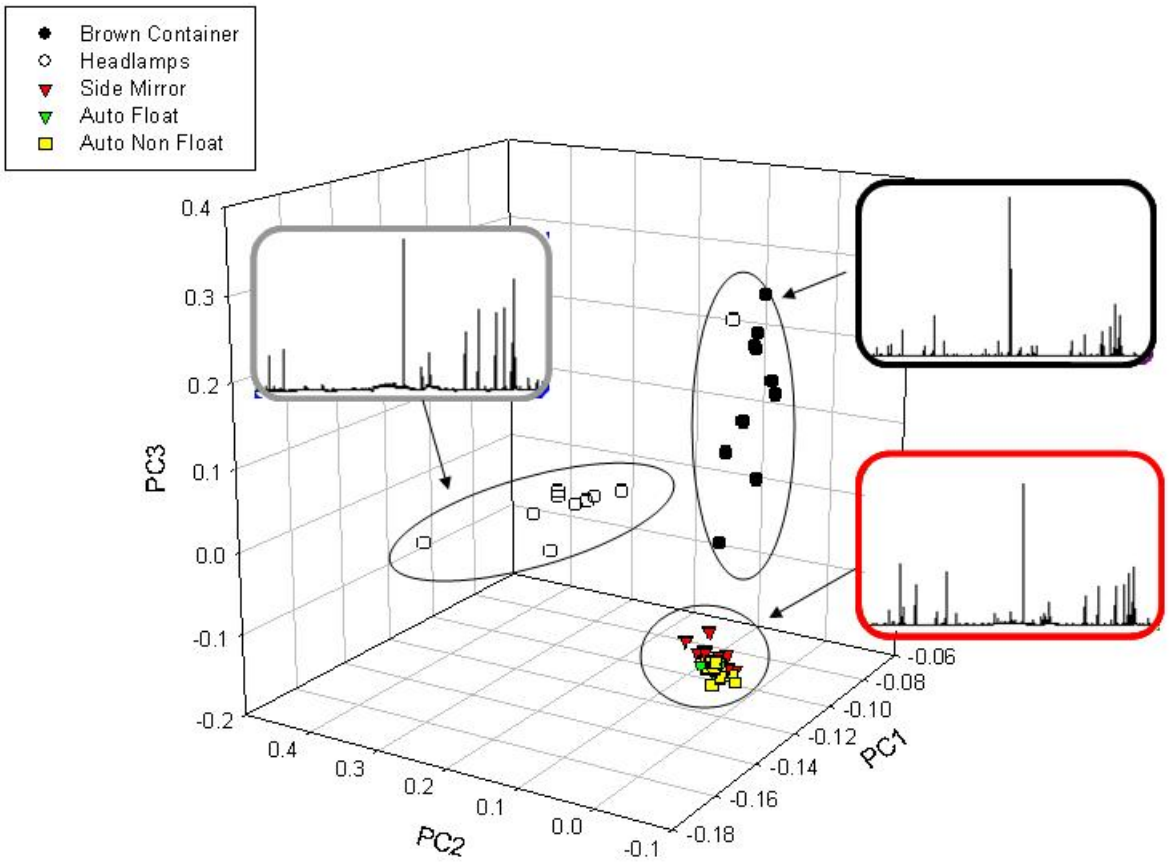

Figure 28: 3-D PCA plot of different types of glass based on full spectral analysis. The ellipses in this plot are not probability ellipses. They are present to clearly show the grouping of samples.

There are three distinct groups evident in Figure 28: the headlamps, the brown container glasses and the float glasses. One of the headlamps is grouped with the brown container glasses; this may be evidence of the two types of headlamps possible: borosilicate and soda-lime-silicate glass. Most of the headlamps were borosilicate and grouped as such; however, there was one sample that may be of the soda-lime-silicate type and groups with the container glasses. The three types of float glass group tightly together: automobile float glass – float side, the automobile float glass – non-float side

and the side mirror glass. Further analysis was performed to separate these types of glasses.

Elemental ratios (Table 22) were created to increase separation of the three types of float glass that were not separated in Figure 28. These ratios were created from peaks in the spectral range of 200 nm – 514 nm. PCA was performed on the elemental ratios in the same manner as that performed for the full spectral. The groups of float glass were nearly separated completely, illustrated in Figure 29. Representative spectra (200 – 514 nm) for each type of glass are presented in Figure 29, to illustrate similarities of the glass spectra. The spectra from the automobile – float glass samples is significantly different from the other two samples, this may be due to the side of the float glass analyzed. The side mirror glass analyzed on the glass side was also the non-float side of the glass and results in spectra similar to the automobile float glass - non-float side samples. However, PCA loadings separated the two types of glasses analyzed on the non-float side.

Table 22: Discriminating ratios used for principal component analysis of the float glasses that were not separated during full spectral analysis

Discriminating Ratios
Fe II (259.94 nm) / Mg (278.03 nm)
Si (252.85 nm) / Mn II (259.99 nm)
Si (221.73 nm) / Fe II (238.28 nm)
Na (285.26 nm) / Si (288.16 nm)
Fe (385.57 nm) / Si (390.57 nm)

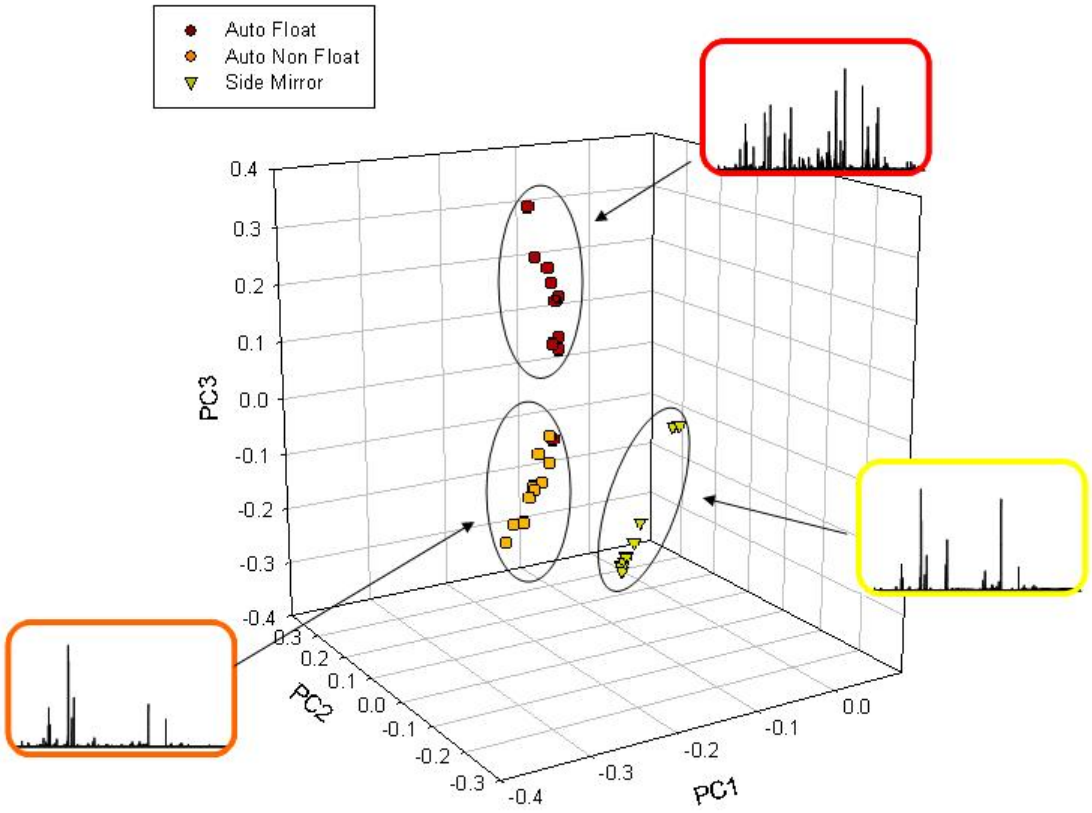

Figure 29: 3-D PCA plot of three types of float glasses based on the same ratio set. The ellipses in this plot are not probability ellipses. They are present to clearly show the grouping of samples.

Conclusion

LIBS in conjunction with RI data can provide discrimination comparable to the discriminating power of the more precise LA-ICP-MS. The lower discriminating power of LIBS results from higher variance observed relative to LA-ICP-MS. Creating a library of LIBS spectra for comparison does not seem feasible at this time due to the higher variance observed for ratios calculated from spectra not collected back-to-back on a

single day. However, this does not rule out using LIBS to perform back-to-back comparisons of known and unknown samples.

The most effective method of analysis for the glass samples was the ANOVA/Tukey HSD analysis which provided high discriminating power for each of the types of glasses. This is useful when comparing or differentiating known and unknown glass samples that are presumed to be from the same type of glass. This method of analysis is tedious based on the procedure for creating discriminating ratios. Therefore, full spectral methods were investigated to facilitate rapid and efficient comparison methods. Of these methods, the Student's *t*-test combine with rank correlation of selected peaks provided the best discriminating power for samples from the same glass type, refer to Table 23.

The area under the curve determined from the ROC curved for automobile float glass samples (float side) may increase if the rank correlation or the Sorenson analytical methods are used for comparison rather than the HQI method.

Table 23: Discrimination percentages of the glass samples analyzed by different methods of analysis at a 90% CL (without RI Data)

Glass Type	Side Analyzed	ANOVA/Tukey HSD				Student's *t-test*				Confidence Interval
		RI	LIBS	LA-ICP-MS	XRF	HQI	Rank	Sorenson	Pearson	Sub-spectral
Auto. Float	Float	96.4	92.9	100	77.1	81.8	92.4	90.5	29.5	78.6
	Non-Float		77.5							
Side Mirror	Glass	46.5	61.3	100	98.7	91.6				
	Deposit				80.6	93.6				
Headlamp	Outside	80.0	98.1	72.4	68.6	84.8				89.3
Brown Container	Inside	81.9	98.1		100	95.2				89.3

CHAPTER SEVEN:
CN AND C_2 DIATOMIC SPECIES

Vibrational bands of diatomic species can be visible but are weak in a LIBS spectrum. The emissions of these vibrational bands generally arise from recombined elements (ion-electron or ion-ion) or emissions of diatomic species that were separated as a whole from the sample during the LIBS event. Molecular C_2 is created in the middle of plasma while CN radicals are created at the edge of the plasma wall where interactions with atmospheric N_2 molecules can occur.[91] Some CN radicals can be created within the plasma if sample analyzed is comprised of carbon and nitrogen. Quantitative analysis via the CN band emission have been published elsewhere[92, 93]; however, analysis performed in this study are qualitative.

The diatomic species can emit from multiple vibrational and rotational states. The vibrational transitions produce larger, more intense bands than the rotational transitions. Rotational bands are observed, especially in the C_2 swan band sets, but it can be difficult to differentiate these bands from baseline noise. Vibronic bands are generally separated into bands sets based on the transitions from the upper to the lower vibrational level ($\Delta\upsilon$), where $\Delta\upsilon$ represents the difference of the vibrational quantum number between the upper and the lower vibrational states.[94, 95] Vibronic bands are labeled as (υ'-υ''), where υ' is the upper vibrational energy level in excited electronic state (E_1) and υ'' is the lower vibrational energy level in the ground electronic

state (E_0). In the $\Delta\upsilon = 0$ band set, the vibrational bands located here are emit from a vibration level in the excited state to the same vibration level in the ground state: i.e. (0-0), (1-1), etc. Whereas, $\Delta\upsilon = +1$ the bands present are from the transitions (1-0) and (2-1) and in the $\Delta\upsilon = -1$ band set include the bands that are from the transitions (0-1) and (1-2), refer to Figure 30.

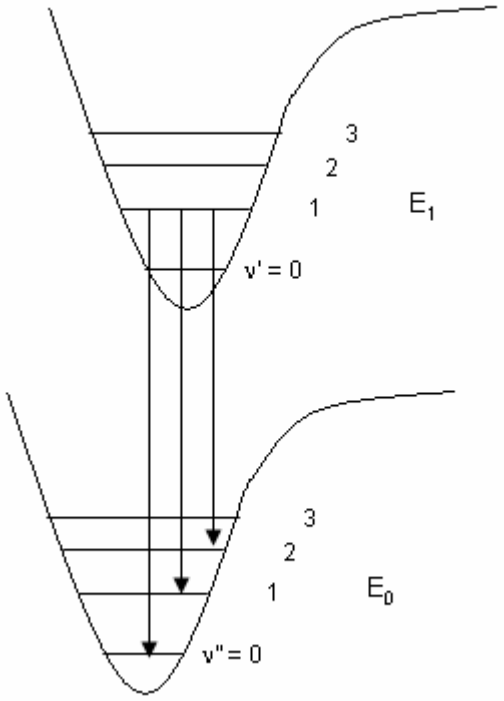

Figure 30: A depiction of the vibronic transitions

Each set has a major band head which is the most intense vibronic band; the band heads are usually the (0-0), (1-0) and (0-1) transitions. Vibrations can be located in a

band set as high and as low as $\Delta\upsilon$ = +/- 6, but the sets most frequently observed are $\Delta\upsilon$ = +2, +1, 0, -1.

C_2 Swan Peaks

C_2 emission peaks belonging to the Swan $d^3\Pi_g \rightarrow a^3\Pi_u$ system were observed most readily in this study. The recombination of two carbon ions yields a C_2 diatomic emission located between 450 – 600 nm, as seen in Figure 31.[94-99] The band heads that were observed are illustrated in Figure 31, these band heads $\Delta\upsilon$ = +1, 0 and -1 which are observed at 471.68 nm, 516.41 nm and 568.50 nm, respectively. Previous research has theorized that the excitation of the C_2 molecule and the C_2 swan bands in the emission spectra has two origins: "dissociation of high mass cluster C_x and their ions C_n^+ in the plasma plume and/or atomic carbon recombination".[100, 101] This mechanism does not seem to be affected by the energy density of the laser.[102]

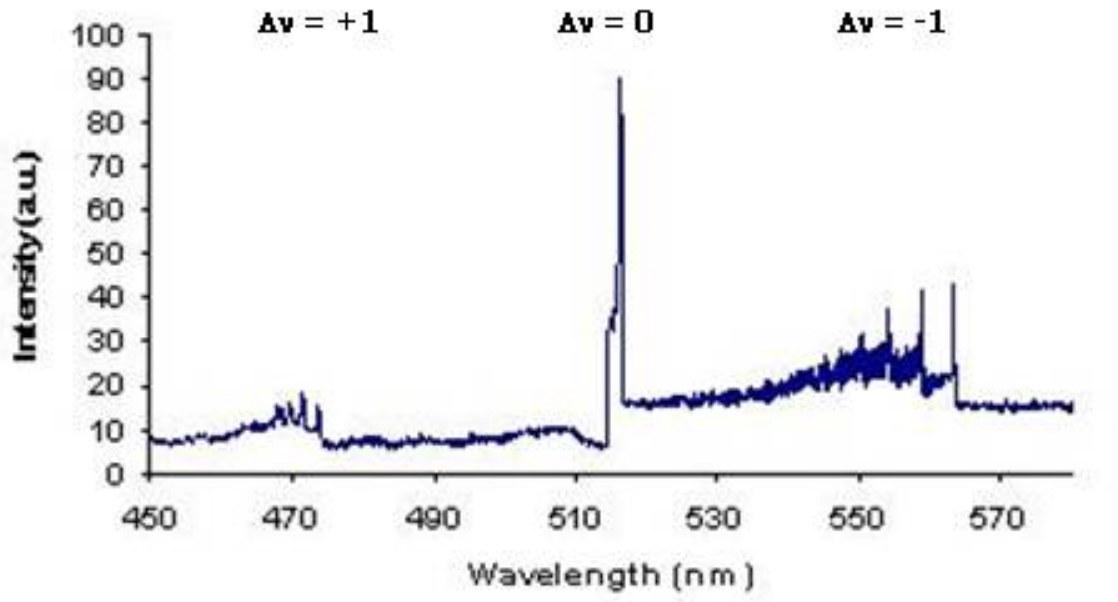

Figure 31: C_2 swan vibrational bands observed from polystyrene analyzed in an air atmosphere

As observed in Figure 31, only one vibrational band, the (0-0) transition, is noticed in the $\Delta\upsilon$ = 0 band set. For these experiments, no other vibronic transitions were observed for this band set as has been presented elsewhere.[72, 94, 95, 101] There is not a complete explanation for this observation, other than this band set falls on of the cusp of two different spectrometers and may have been lost. While the vibronic transition bands are observed most readily, the rotational peaks are largely noticed in the $\Delta\upsilon$ = -1 series. These peaks provide rotational information about the C_2 species.[94]

CN Violet Peaks

CN radical emissions observed in this study are from the violet vibration – rotational $B^2\Sigma \rightarrow X^2\Sigma$ system; these peaks are observed in the 350 - 430 nm spectral region, as seen in Figure 32.[94-96] The emissions of the CN radical band heads observed in the LIBS spectra CN vibration exhibits triple bond character of the diatomic species. The sets of bands that are observed are with this instrument are $\Delta\upsilon$ = +1, 0 and -1 which are located at 359.04 nm, 388.34 nm and 421.63 nm, respectively (refer to Figure 32). Other important CN emission systems, such as the red $A^2\Pi$-$X^2\Sigma^+$ system (704 – 738 nm)[99, 103], may provide more information about the sample. The red system is generally the strongest of the vibrational systems[104]; however, these bands were not observed in this study.

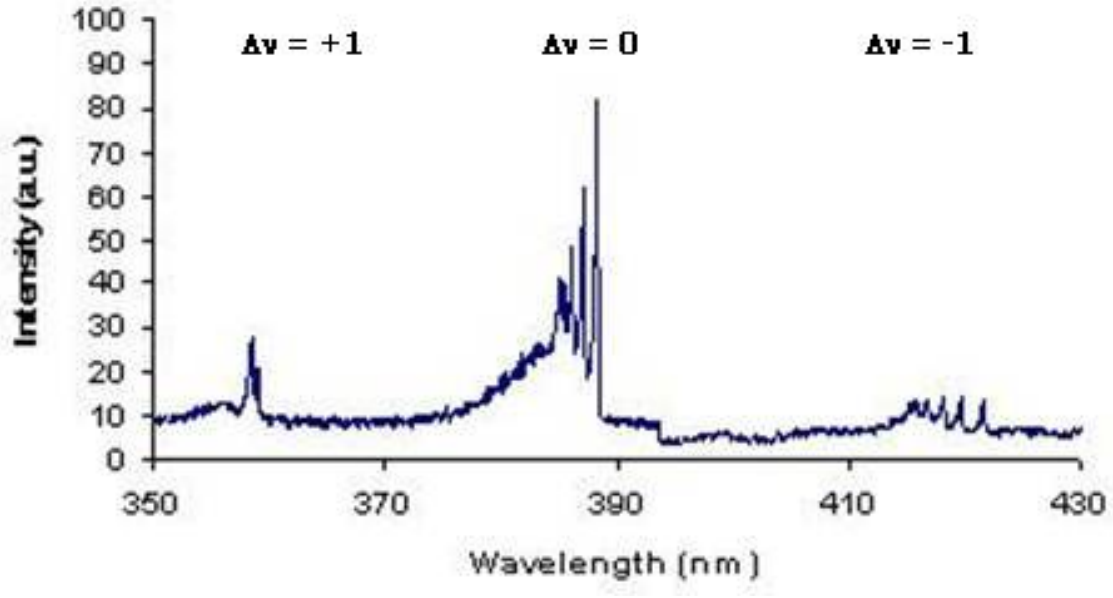

Figure 32: CN violet vibrational bands observed from polystyrene analyzed in an air atmosphere

It is theorized that the creation of the CN radical within a plasma plume occurs by two mechanisms, which occur at two different laser energies or fluences. At low energy the CN diatomic species is formed through a bimolecular reaction:[100]

$$C_{2(gas)} + N_{2(gas)} \rightarrow 2CN_{(gas)} \quad \textbf{(28)}$$

At higher laser fluences, approximately greater than 20 J cm^{-1}, the nitrogen molecule dissociates due to energetic collisions within the plasma. It is then theorized that the CN radicals are created through either one of the following two reactions:[100]

$$C_{2(gas)} + N_{gas} \rightarrow CN_{(gas)} + C_{(gas)} \quad \textbf{(29)}$$

$$C_{(solid)} + N_{(gas)} \rightarrow CN^{\bullet}_{(gas)} \quad \textbf{(30)}$$

In a LIBS plasma event, all elements in the immediate surroundings of the plasma are incorporated into the plasma, including the surrounding atmosphere. Hence, the CN vibronic emission can results from a recombination of atoms created in one of two ways: a sample's carbon atom recombines with a sample's nitrogen atoms or a sample's carbon atom recombines with an atmospheric nitrogen atom.

Comparison of Vibronic Bands to Infrared Spectroscopy

The vibrational transitions observed in LIBS spectra are similar to the stretching frequencies that are obtained from infrared spectroscopy. When converted from wavelength (nm) to wavenumbers (cm^{-1}), the difference between the band head from

different band sets can be compared to stretching frequencies of ground state organic molecules. This comparison can provide insight into the type of bond between the two atoms, whether single, double or triple bonds. The vibrational difference may be determined for either the excited state or the ground state; this depends on which diatomic emission bands are observed in the spectrum. This difference is illustrated in Figure 33, by the red arrows.

Figure 33: Depiction of the energy state used to calculate the vibrational difference

From the calculated frequencies given in Table 24, the structure of the CN diatomic species possesses triple bond character. This difference is not similar to the CN single bond stretch located around 1250 – 1020 cm^{-1}.[105] The structure of the C_2 possesses a carbon-carbon double bond (C=C) character. The difference observed in Table 24 for the C_2 bands is low to be considered a C_2 triple bond, which has stretching bands around 2260 – 2100 cm^{-1}.[105]

The stretching frequencies presented in Table 24, are a range of where the ground state stretching frequencies can be located on an IR spectra for these diatomic bonds The frequencies observed from the IR spectra of for bonds that are flanked by R groups. The frequencies calculated from the vibronic bands are from diatomic species that are free from any substituents. This may account for the difference observed in the stretching frequencies calculated from the vibronic bands and IR spectra.

Table 24: Comparison of vibrational bands and IR stretching frequencies

Diatomic Species	Band Head	nm	cm^{-1}	Difference (cm^{-1})	Stretching Frequency*	Moiety
CN	(0,1)	421.63	23,717	2034 Ground state	2260 - 2222	CN Triple Bond
	(0,0)	388.34	25,751			
	(0,0)	388.34	25,751	2101 Excited state		
	(1,0)	359.04	27,852			
C_2	(0,1)	563.50	17,746	1618 Ground state	1667 - 1640	C_2 Double Bond
	(0,0)	516.41	19,364			
	(0,0)	516.41	19,364	1744 Excited state		
	(1,0)	473.68	21,108			

*reference 105

Two-Dimensional (2-D) Correlation Spectroscopy

Two-dimensional (2-D) correlation spectroscopy is a technique that can identify the relationship two different series of peaks based on their emission intensities over time.

This technique can identify the correlation between two groups that are strongly interacting with each other. The 2-D correlation spectroscopy is based on two orthogonal components, the synchronous and the asynchronous correlation spectra, both of which provide a wealth of information about the two spectral regions being compared. Another advantage of using this correlation spectroscopy technique is that the sequential order of the intensity change of the two spectral regions with respect to the time is available.[106]

Synchronous 2-D Correlation Spectra

The spectral data must be measured at *m* equally spaced points in time *t* between the observation time T_{min} and T_{max}. This data set is represented by equation 31, where ν is the spectrum at the specified time t_j, where j = 1 - m.

$$\tilde{y}_j(\upsilon) = \tilde{y}(\upsilon, t_j) \quad \textbf{(31)}$$

The synchronous correlation spectrum Φ (υ_1, υ_2) is represented by the product of two spectral matrices:

$$\Phi(\upsilon_1, \upsilon_2) = \frac{1}{m-1} \tilde{y}(\upsilon_1)^T \tilde{y}(\upsilon_2) \quad \textbf{(32)}$$

In a synchronous 2-D correlation spectrum the intensity of the correlation represents the simultaneous change of the "spectral intensity measured at υ_1 and υ_2 during the

interval between t_{min} and t_{max}".[106, 107] In equation 32, υ_1 and υ_2 are spectral variables 1 and 2; t_{min} and t_{max} signifies the time interval of which the peaks where analyzed. A positive peak in a synchronous correlation plot signifies that the two spectral variables are increasing or decreasing together with respect to the external variable, t. If one spectral variable increases while the other decreases, a negative peak is observed.[106, 107]

Asynchronous 2-D Correlation Spectra

The Asynchronous correlation spectrum Ψ (υ_1, υ_2) is represented by the following equation:

$$\Psi(\upsilon_1,\upsilon_2)=\frac{1}{m-1}\tilde{y}(\upsilon_1)^T N\tilde{y}(\upsilon_2) \quad \textbf{(33)}$$

A linear transformation is necessary to provide an orthogonal discrete matrix of the second spectral range variable, $\tilde{y}(\upsilon_2)$. The Hilbert-Noda transformation matrix (N) is used to transform this variable.

$$N=\frac{1}{\pi}\begin{bmatrix} 0 & 1 & \frac{1}{2} & \frac{1}{3} & \ldots \\ -1 & 0 & 1 & \frac{1}{2} & \ldots \\ -\frac{1}{2} & -1 & 0 & 1 & \ldots \\ -\frac{1}{3} & -\frac{1}{2} & -1 & 0 & \ldots \\ \ldots & \ldots & \ldots & \ldots & \ldots \end{bmatrix} \quad \textbf{(34)}$$

The asynchronous 2-D correlation spectrum reveals the nature of sequential changes between the two spectral variables. Peaks are only observed in this spectrum if the intensity of the two spectral variables change asynchronously with respect to one another. If the sign of the peak is positive, the intensity change of ν_1 precedes than the change in ν_2 as the perturbation is applied. The sign in negative if the opposite occurs, i.e. if the intensity change of υ_2 precedes the change in υ_1.[106, 107] If no peaks are observed in this spectrum then the two spectral variables move simultaneously as the perturbation is applied.

Comparison between C(I), CN and C_2 peaks

Synchronous and the asynchronous plots were generated to determine the relationships between the C (I) atomic emission peak, the CN violet $\Delta\upsilon = 0$ bands and the C_2 swan $\Delta\upsilon = -1$ vibrational bands. The C_2 $\Delta\upsilon = 0$ was not used in this set because the whole band series was not present.

Sample Analysis

A polystyrene sample was analyzed in an air atmosphere in order to observe the CN bands. An average spectrum comprised of ten single shot spectra, each collected at a different position on the sample's surface. A set of ten single shots were collected at increasing spectrometer time delays from +1.0 μs to -20.0 μs at 0.5 μs intervals.

Synchronous and asynchronous plots were generated for the following comparisons: C (I) & CN, C (I) & C_2, and CN & C_2.

The data was mean-centered prior to generating the 2-D correlation plots. The spectral data collected at each delay time was averaged across the wavelengths and this "averaged spectrum" was subtracted from each individual spectrum.

Results and Discussion

The synchronous and the asynchronous plots that represent the comparison between the CN violet bands (υ_1) compared to the C_2 swan bands (υ_2) are illustrated in Figure 34. The synchronous plot indicates that the two peaks simultaneously decrease in intensity. The asynchronous plot, on the other hand, the negative peaks indicate that the intensity change in the CN peaks occurs slower than the change in the C_2 peaks with respect to the external variable time (t). This change is observed due to the steep drop in intensity of the C_2 peaks when compared to the CN peak. The lifetime of CN is longer than the lifetime of the C_2 species, $\tau_{C2} < \tau_{CN}$.

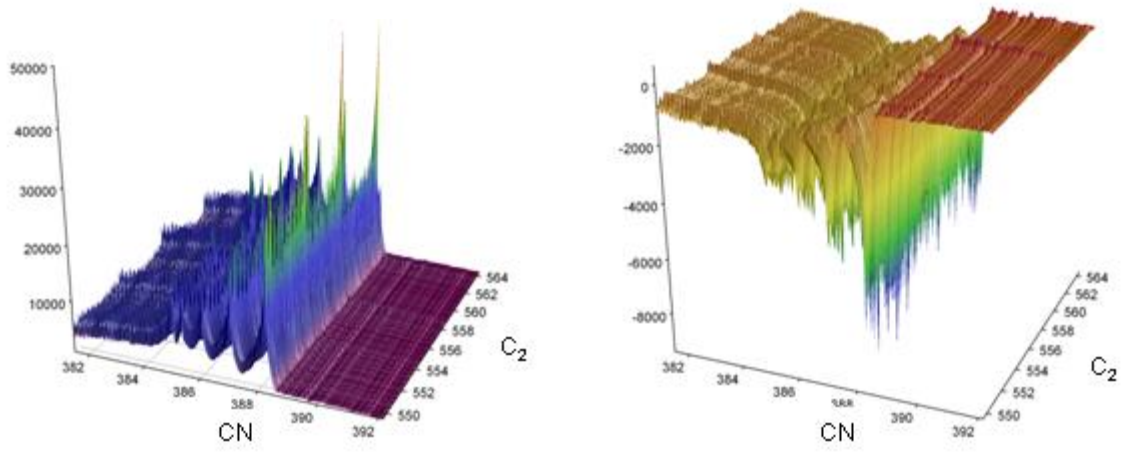

Figure 34: The synchronous and asynchronous plots of the CN Violet vs. C_2 Swan peaks

The synchronous and the asynchronous plots that represent the comparison between the C (I) atomic emission peak (υ_1) compared to the CN violet bands (υ_2) are illustrated in Figure 35. The synchronous plot indicates that there is a simultaneous change of the two spectral variables. The intensity from both variables decreases with time. The asynchronous plot, however, has a positive intensity which indicates that the C (I) peak loses intensity faster than the CN violet bands, indicating a shorter lifetime of the C (I) atomic peak.

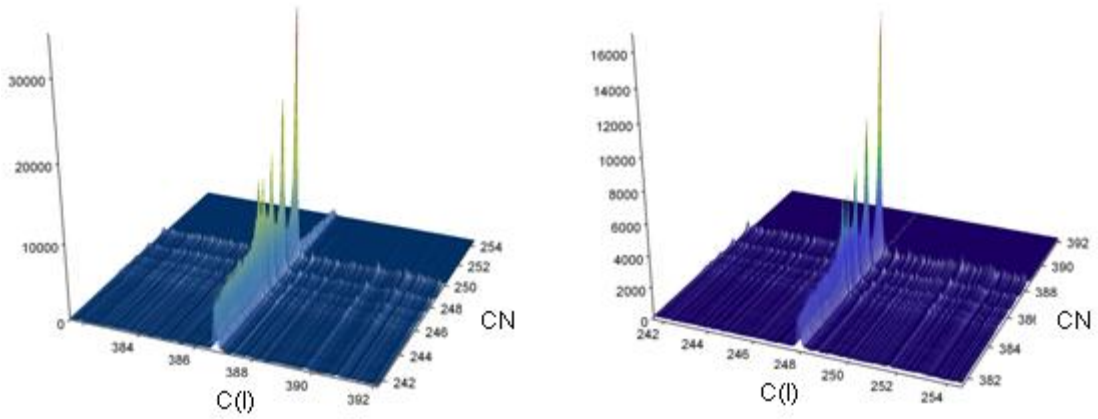

Figure 35: The synchronous and asynchronous plots of the C (I) vs. the CN Violet peaks

The synchronous plot between the C (I) atomic peak (υ_1) and the C_2 swan band (υ_2) in Figure 36 indicates that the two spectral variables decrease similarly. The asynchronous plot shows the C (I) changes faster than the C_2 swan bands, which indicates that the lifetime of C (I) is shorter than the C_2 bands. The lifetime of the C_2 bands is longer than the atomic peak which is also illustrated in Figure 36.

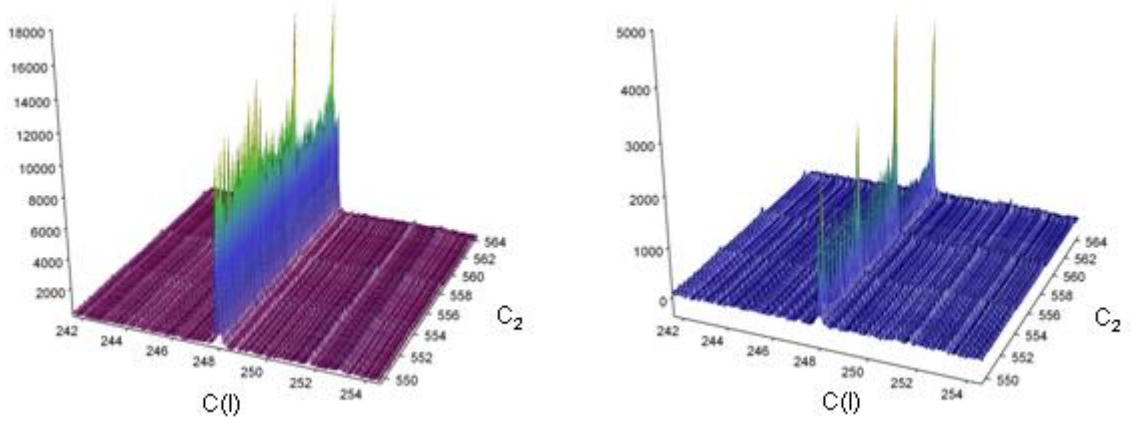

Figure 36: The synchronous and asynchronous plots of the C (I) vs. the C_2 Swan peaks

Based on the asynchronous plots illustrated in Figure 34 - Figure 36, the lifetime of these three species in the plasma created in these experiments are $\tau_{C(I)} < \tau_{C2} < \tau_{CN}$. This relationship is in accordance with the natural lifetimes of the atomic peak, violet and swan transitions are 29 ns, 64 ns and 102 ns, respectively ($\tau_{C(I)} < \tau_{C2} < \tau_{CN}$).[100] These lifetime can become longer for optical emissions of these species, over 200 ns for atomic emissions and over 1 μs for molecular species.[100]

Due to the poor time resolution of the spectrometer used in this study, it was not possible to see the growth of the diatomic band intensities. It might be possible that 2-D correlation spectra can be used to determine the relationship of these species during their formation in the plasma, i.e. which species is produced initially. It has been theorized by Abdelli-Messaci that the formation of the CN species is based on the C_2 species (refer to equations 28 and 29).[100] However, this Abdelli-Messaci makes no mention of how the carbon atomic peak is related and/or affected by the formation of diatomic species.

CHAPTER EIGHT:
DETECTION OF TRACE LEVELS EXPLOSIVE

The detection of explosives has become a major issue to Homeland Security in the last few years. Rapid detection and classification of trace levels of explosives or energetic materials has become necessary. Research from other groups has explored the use of LIBS to identify explosive materials. López-Moreno et al utilized a 45 m stand-off LIBS detection system of explosives based on elemental ratios and the presence of Swan bands.[108] Elemental ratios have been used by DeLucia et al. for detection of energetic materials, as well.[6] Elemental ratios have also been used to compare single pulse LIBS to double pulse LIBS in the analysis of explosive residues.[109] LIBS has been used to detect landmines and their casings.[110, 111] All these research groups reported the sampling of explosive materials in air, which introduces atmospheric nitrogen and oxygen in the resulting spectra.

Organic high explosive materials mostly contain carbon, nitrogen and oxygen. When samples of these materials are analyzed by LIBS, diatomic molecular emissions are observed in the resulting spectra. The diatomic emissions that are primarily observed are the CN and the C_2 band emissions. The relationship between the sample's molecular structure and the diatomic species emissions was investigated in this study. A method for the depositing trace amounts of explosives in solution or other explosive-like materials on solid supports was developed and nanosecond single pulse LIBS data

were recorded. Polystyrene and a 1,000 ppm solution of 2,4-dinitrotoluene (2,4-DNT) in acetonitrile (ACN) were used as standards. In a second set of experiments powdered materials were analyzed. The detection limits observed in this work for 2,4-DNT trace levels on copper substrate are lower than surface explosives contamination levels previously reported. RDX was detected on an aluminum substrate at a detection limit of 40 $\mu g/cm^2$ using a man-portable LIBS system (MP-LIBS).[109] The detection limit observed in this study was generally 1.08 $\mu g/cm^2$ but was as low as 18.07 ng/cm^2 on one occasion.

Explosives in Solution

Sample Preparation

Trace Surface Loading Preparation

One mg of the analyte was dissolved in one mL of acetonitrile (ACN) to give a 1000 ppm solution. A 0.81 cm^2 square of background/support material was used for these experiments. The support was cut to 0.9 cm on each side so that it would easily fit into a square 1 cm quartz absorption/fluorescence cell (1 cm x 1 cm x 4 cm). The cell was utilized for experiments described below wherein a blanket of argon (Ar) was placed over the sample by flooding the cell. Using an Eppendorf pipette, 10 µL of the explosive solution was delivered to the center of the support material. The solvent was allowed to evaporate in the face of a chemical fume hood. Five measurements were made of the diameter of the film of residue left after the solvent evaporated. The

diameter depends on the substrate but is reproducible and independent of the analyte concentration in the dilute solutions used. The surface loading in $\mu g/cm^2$ was calculated from the analyte concentration, volume delivered to the substrate and the average diameter of the residue.

Homogeneity of the Deposited Samples

For single shot analysis in this study it was important that a homogenous residue was analyzed in order to maximize the area of analysis. The residue is too thin to do depth analysis with LIBS; therefore, single shot analysis at different points of the residue is required for single averaging. Homogeneity of a sample's residue is a function of not only of the sample but on the solvent used as well. The initial solvent used was ACN because of the good solubility of 2,4-DNT in this solvent. In addition to ACN, acetone, toluene and methanol were also examined as solvents for these experiments. 1000 ppm solutions of 2,4-DNT in each solvent were prepared. 100 μL of each solution was deposited onto the copper support. The diameter of the residue was measured to calculate the surface concentration of 2,4-DNT on the support. One hundred single-shot spectra were collected in air, across the residue to determine if the 2,4-DNT was homogenous distributed. The CN (0-0) band was used to estimate the homogeneity of the residue.

Table 25: Solvent effect on the homogeny of sample's residue

	Acetonitrile	Methanol	Toluene	Acetone	Polystyrene
Concentration (mg/mL)	1.00	1.00	1.00	1.00	
Drop Amount (µL)	100	100	100	100	
Drop Diameter (cm)	1.42	2.04	2.18	2.72	
Surface Concentration (mg/cm^2)	0.063	0.031	0.027	0.017	
Average Intensity	200.69	120.91	100.29	119.97	87.92
%RSD of the CN (0-0) peak	23.80	47.89	62.62	42.68	15.41

When analyzed in air, the CN intensity of the residual 2,4-DNT is more intense than the intensity from the polystyrene standard. This is possibly due to the difference in the structure of each sample or the concentration of the analyte. Polystyrene is a polymer whereas 2,4-DNT is deposited as single molecules. In the case of the single molecules, the most of the laser's energy goes into ionizing and atomizing the elements in the sample. In the case of the polymer, while the laser's energy would go into atomizing and ionizing the sample's elements, some of the energy goes into breaking polymer bonds as well. Therefore, less of the sample is ablated from the sample resulting in less intense CN bands.

The residues left after solvent evaporation do not appear homogenous but instead have random circles and spots within the residual area, refer Figure 37. It was determined

that these residual spots are not a concentrated area of 2,4-DNT but are likely areas of oxidized copper, and coincide with area where the solvent was slow to evaporate.

Figure 37 show images of the 2,4-DNT residues left behind by various solvents. The 2,4-DNT residue is not the large, lighter areas but the tiny crystals noticed mainly around the edge of the residue. Methanol left a large opaque white spot that disappeared over time. Again, this was not a concentrated area of 2,4-DNT; however, the exact nature of the spot was not determined.

Acetonitrile (ACN)

Acetone

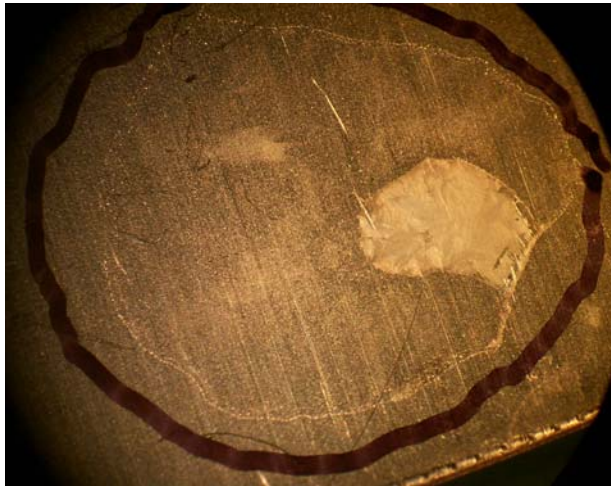

Methanol

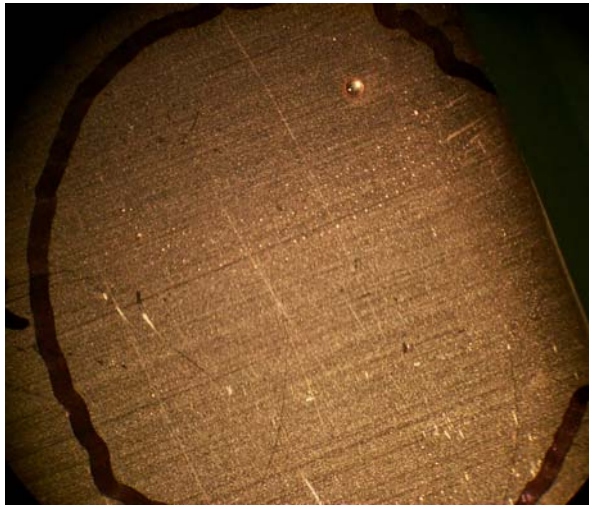

Toluene

Figure 37: 2,4-DNT residue from various solvents on a copper support

To determine that these lighter areas were not analyte concentrated 50 μL of pure ACN was deposited onto the copper support and allowed to evaporate in the face of a chemical fume hood. Similar residual spots were observed as before and this area was analyzed in addition to pure copper. Emissions from the diatomic species were not observed in the single-shot spectra collected from the ACN residue or the copper substrate.

LIBS Experimental Method

A diagram of the LIBS2000+ sample chamber is given in Figure 38.a. Experiments were performed in one of three ways. The first way consisted of placing the analyte-coated substrate in the sample chamber and the analysis was performed either in an atmosphere of air or under a flow of Ar (approximately 145 mL/min) directed onto the substrate. The second way consisted of placing the analyte-coated substrate into a quartz fluorescence/absorption cuvette. The cuvette was aligned such that the laser was focused on a spot within the thin film of analyte. A blanket of argon was flowed over the sample by flowing the gas into the cuvette through a Teflon needle inserted into the top of the cell (refer to Figure 38.b). The third way consisted of fashioning a cap for the cuvette which would slow the argon from flowing out of the cell and create an argon atmosphere with minimal air content. This cap was created from a polyvinyl chloride plastic piping, a borosilicate glass which did not absorb the laser's energy and an air-tight tubing sealed into the piping for gas transportation (Figure 38.c).

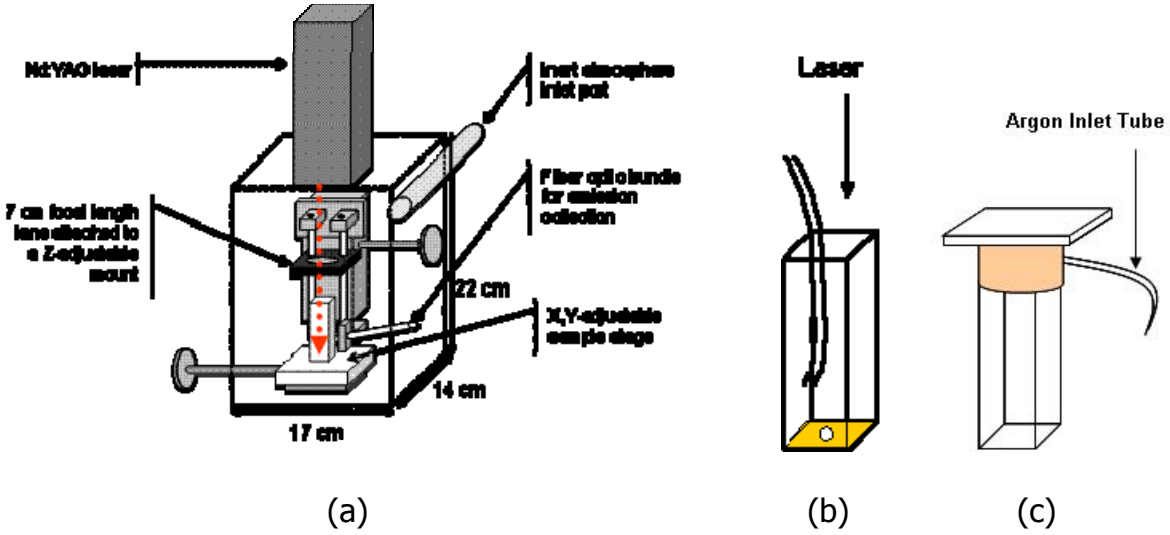

Figure 38: Diagram of the LIBS 2000 sample chamber and cuvette setups: (a) LIBS setup used for analysis with the cuvette, also illustrated are the Nd-YAG laser, the focal lens and the sample stage. (b) Initial cuvette setup with the gas tight tube for argon directed over the sample. (c) Final cuvette setup with fitted cap to create and ensure an argon atmosphere for sample analysis.

All spectra were collected as single-shot spectra without averaging. Laser power was 31.5 mJ/pulse and the spectrometer delay time for spectral collection was set to 2.5 μs. Prior to collecting the first spectrum and between spectra, the argon was allowed to flow for 2 minutes.

Analysis and Results

2,4-Dinitrotoluene (2,4-DNT) was analyzed on various supports to determine which support material allows for the most intense peaks from 2,4-DNT with the least amount of interfering background peaks. Substrates examined included: copper, aluminum

foil, lead and a glass microscope slide. Spectral bands originating from the support material were observed, along with C (I), CN and C_2 bands associated with the presence of the 2,4-DNT.

Spectra of 2,4-DNT on the support materials are shown in each figure below, in an air atmosphere and under a flow of argon. The top spectra in each figure shows a 10-shot average spectrum of standard polystyrene in air to facilitate the identification of the diatomic species' emissions, CN and C_2.

Copper Substrate

Figure 39 - Figure 41 show the analysis of 2,4-DNT in an air atmosphere and under a flow of argon (145 mL/min). The CN and C_2 peaks are quite intense and they can be seen readily. Due to the large number of lines that are produced from the copper substrate, the area around the CN (0-0) band and the C_2 (0-0) band was expanded in Figure 40 - Figure 41 to show that the these bands are present and that copper is in the vicinity but not interfering with the diatomic emissions.

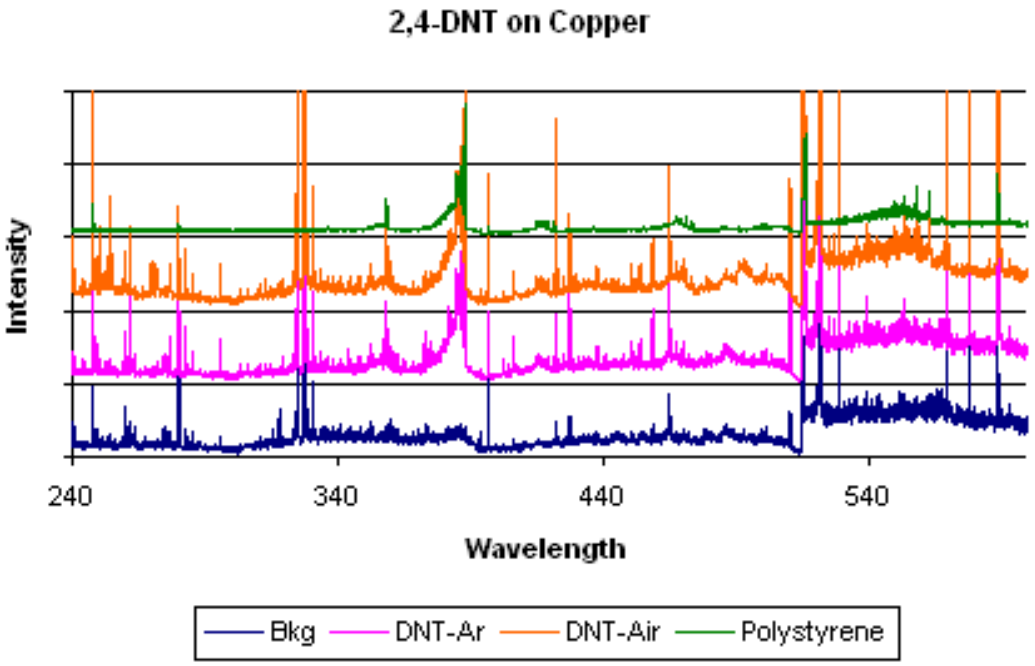

Figure 39: LIBS spectra of 2,4-DNT collected on a copper substrate under an argon flow and in an air atmosphere

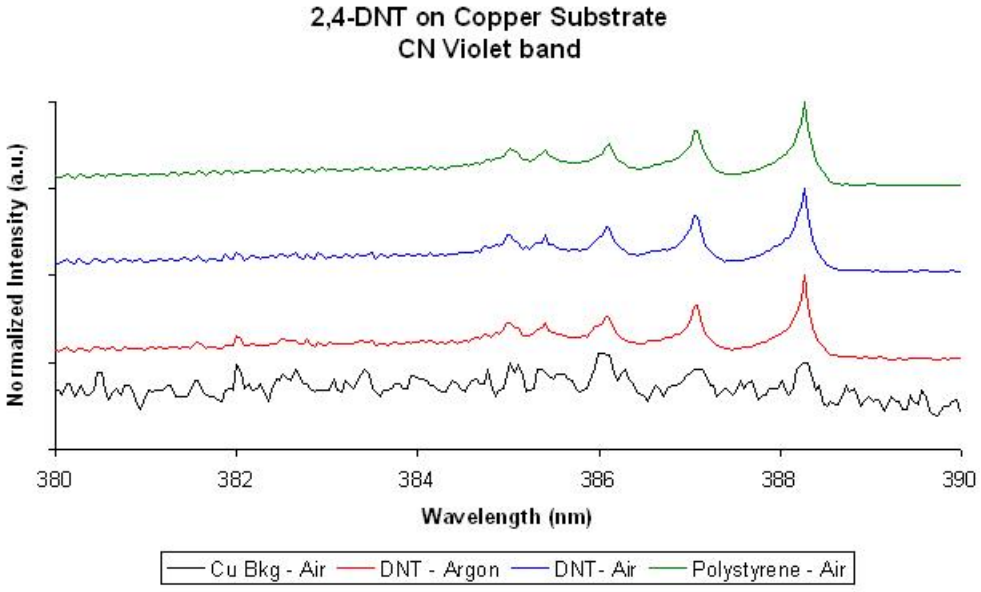

Figure 40: Close up of CN violet bands from the 2,4-DNT on a copper substrate under an argon flow and in an air atmosphere

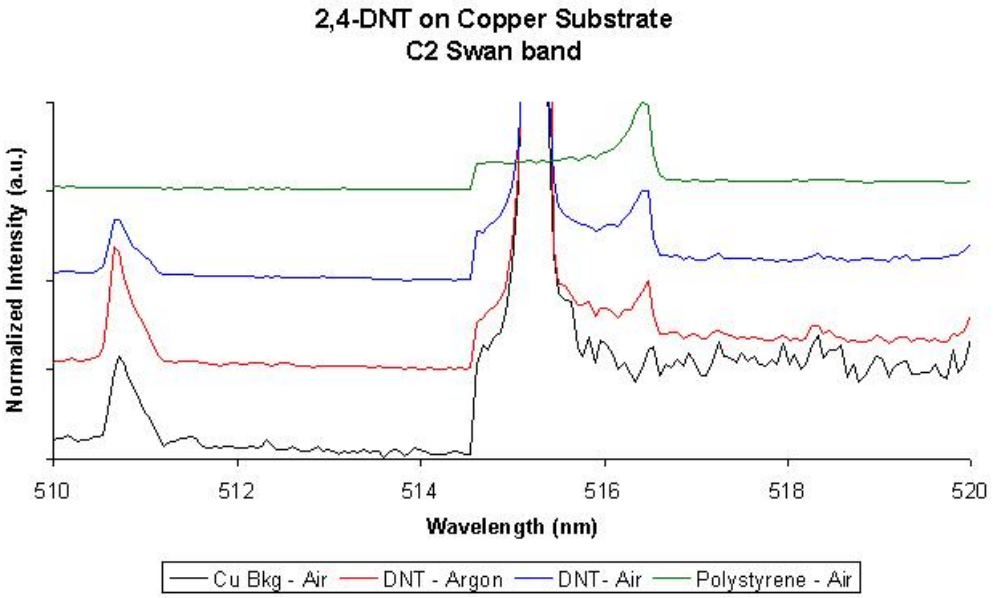

Figure 41: Close up of C_2 swan bands from the 2,4-DNT analysis on a copper substrate under a flow of argon and in an air atmosphere

Aluminum Substrate

The analysis of 2,4-DNT on an aluminum support is shown in Figure 42. While the aluminum substrate contributed fewer lines than copper, the CN and C_2 band intensities were smaller than those observed on the copper, (refer to Figure 39). All peaks were present with relatively high intensities, except for the C_2 $\Delta\upsilon$ = +1 series which was quite low. There are no significant differences between the spectra resulting from a change in atmosphere from air to a flow of argon.

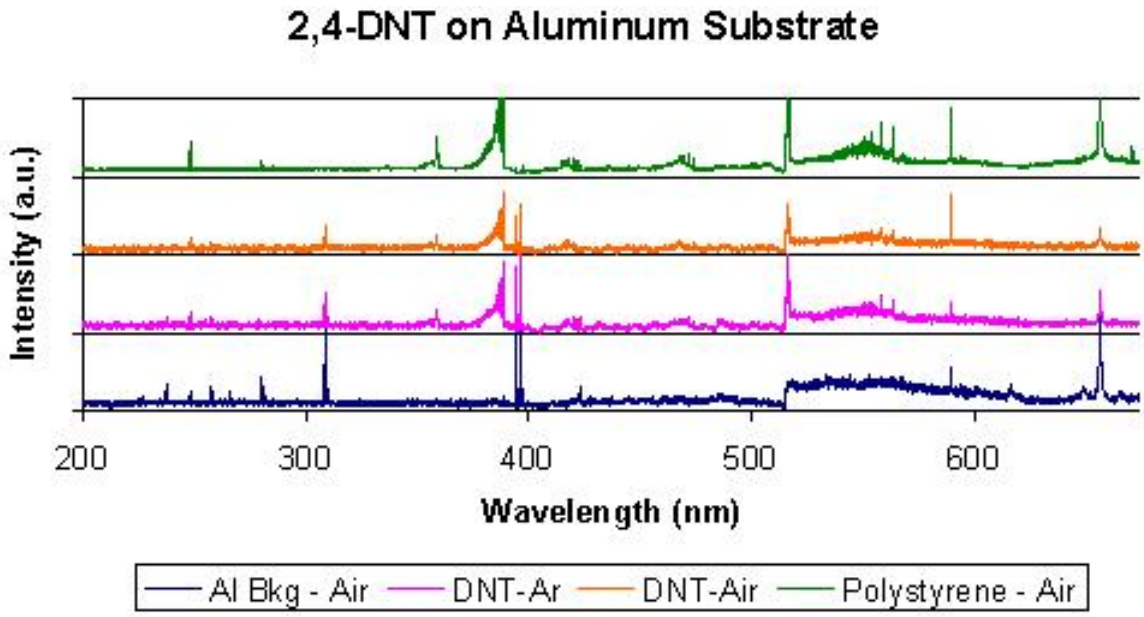

Figure 42: LIBS spectra of 2,4-DNT collected on aluminum foil under a flow of argon and in an air atmosphere

Borosilicate Glass Substrate

The analysis of 2,4-DNT on a borosilicate glass microscope slide produced similar results to the aluminum support, refer Figure 43; however, due to the nature of the glass sample, the diameter of the 2,4-DNT residue was twice as large as those on the aluminum and the copper substrates (Table 26), resulting in a factor of four decrease in 2,4-DNT surface concentration.

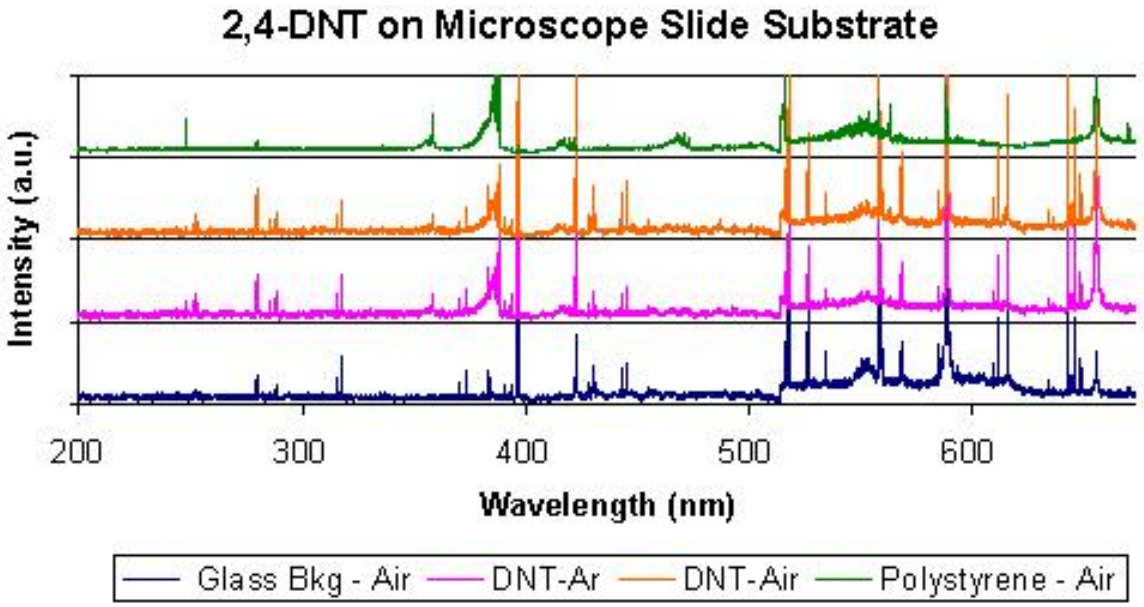

Figure 43: LIBS spectra of 2,4-DNT collected on a microscope slide in argon and air atmosphere

Table 26: Surface concentrations of 2,4-DNT on different substrates

	Copper	Aluminum	Microscope Slide
Soln. Conc. (ppm)	1000	1000	1000
Vol. Delivered (μL)	100	100	100
Wt Delivered (μg)	100	100	100
Drop Diameter (cm)	1.5	1.5	3.0
Area (cm^2)	1.77	1.77	7.07
Surface Conc. ($\mu g/cm^2$)	56.6	56.6	14.2

Lead Substrate

Lead was also examined as a substrate for this analysis, refer to Figure 44. This substrate provided few background peaks which did not overlap any of the diatomic species emissions that were being examined. Emission from atomic carbon and the

diatomic species were not observed during this analysis and lead was removed as a substrate.

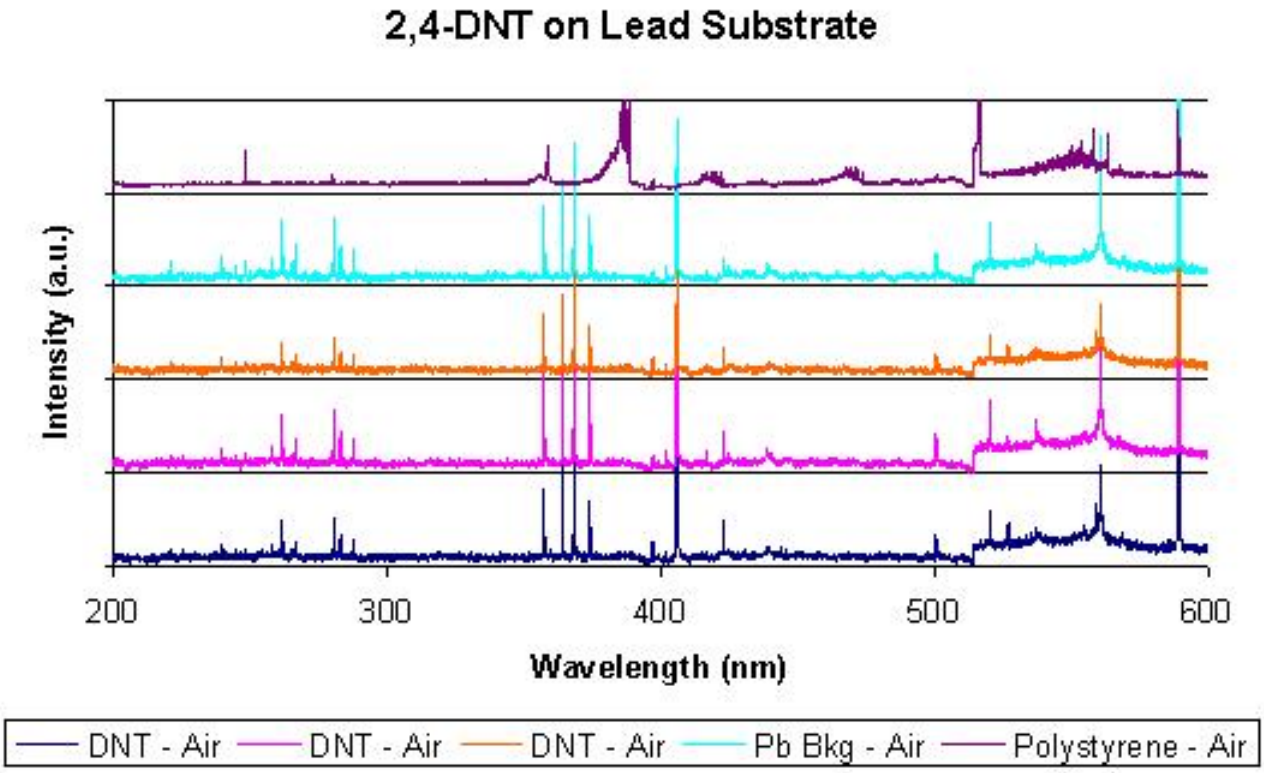

Figure 44: LIBS spectra of 2,4-DNT collected on a lead substrate in air and under argon atmosphere

Analysis of Nitrogen Containing Molecules

Analysis in Atmospheric Air

Portnov's groups explored the use of LIBS in an air atmosphere to characterize organic compounds, including energetic materials and polycyclic aromatic hydrocarbons (PAHs), by C_2/CN and O/N emission ratios. Their study also investigated the relationship between the diatomic emission ratio and the structure of the molecule.[91] Recent

literature has followed similar methods of analysis for detecting and characterizing explosives and energetic materials.[18, 108, 110]

The study presented here was to determine if an increasing number of carbons in the analyte can affect the emission intensity of the diatomic species and if any molecular structural information about the analyte can be discerned from the intensity of these vibronic band emissions.

LIBS Experimental Method

1000 ppm solutions were prepared in ACN. Samples analyzed in this study included: PAHs and nitroaromatics with various number of nitro substitutions on the ring. 100 μL of each solution was deposited onto a copper support. The ACN solvent was allowed to evaporate in the face of a chemical fume hood and the residue was immediately analyzed by single shot analysis. Five (5) single shot spectra were collected in an air atmosphere at a spectrometer delay of 2.5 μs. The diatomic emission intensities were averaged and the %RSD was calculated for each peak. The samples analyzed in this study are presented in Table 27.

Table 27: Structures of samples analysis in the study of nitrogen containing materials in an argon atmosphere

Samples	Structure
p-Nitrotoluene (p-NT)	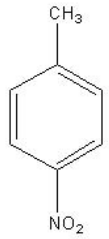
1,4-Dinitrobenzene (1,4-DNB)	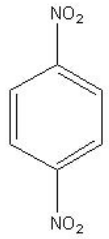
2,4-Dinitrotoluene (2,4-DNT)	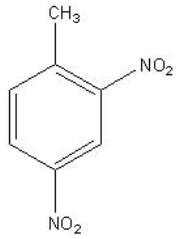
1,2,4-Trimethylbenzene (1,2,4-TMB)	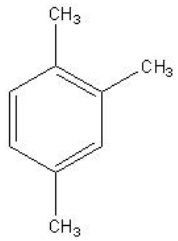
2,4,6-Trinitrotoluene	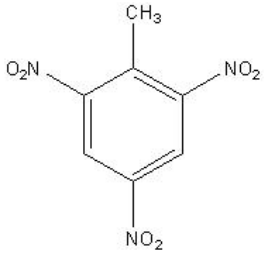

Table 27: Structures of samples analysis in the study of nitrogen containing materials in an argon atmosphere continued

Samples	Structure
Cyclotrimethylenetrinitramine (RDX)	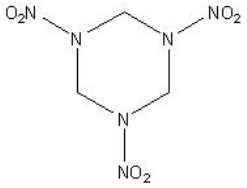
Anthracene (Anth)	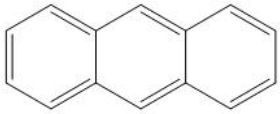
9-Methylanthracene (9-MA)	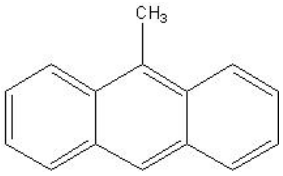
Flouranthene (Flour)	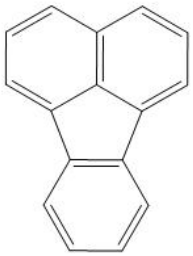
Naphthalene (Naph)	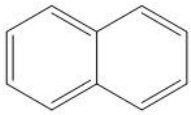
1-Cyanonaphthalene (1-CN)	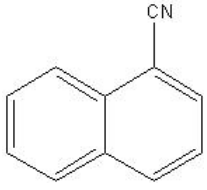
1-Nitronapthalene (1-NN)	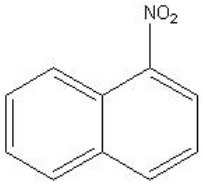

Table 27: Structures of samples analysis in the study of nitrogen containing materials in an argon atmosphere continued

Samples	Structure
2-Methylnaphthalene (2-MN)	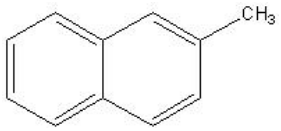
1,5-Dimethylnaphthalene (1,5-DMN)	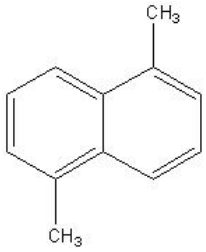
Poly(acrylic acid) (PAA)	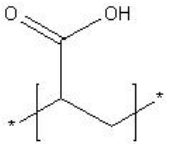
Polyacrylonitrile (PAN)	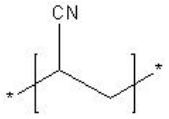
Polyethylene (PE)	
Polypropylene (PP)	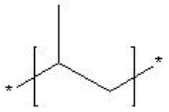
Polystyrene (PS)	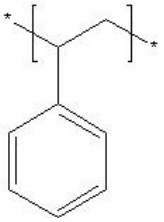
Graphite Carbon	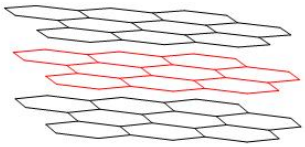

Results and Discussion

Analysis in an Air Atmosphere

Residues of nitrogen containing samples and polycyclic aromatic hydrocarbon (PAH) samples were analyzed in air on a copper support. The single shot spectra were averaged and the C_2/CN ratio was calculated for each sample. This ratio was plotted against the moles of carbon/cm^2 to determine how the nitrogen in the sample affects the resulting spectra, refer to Figure 45. Similar sample types are presented in the same color.

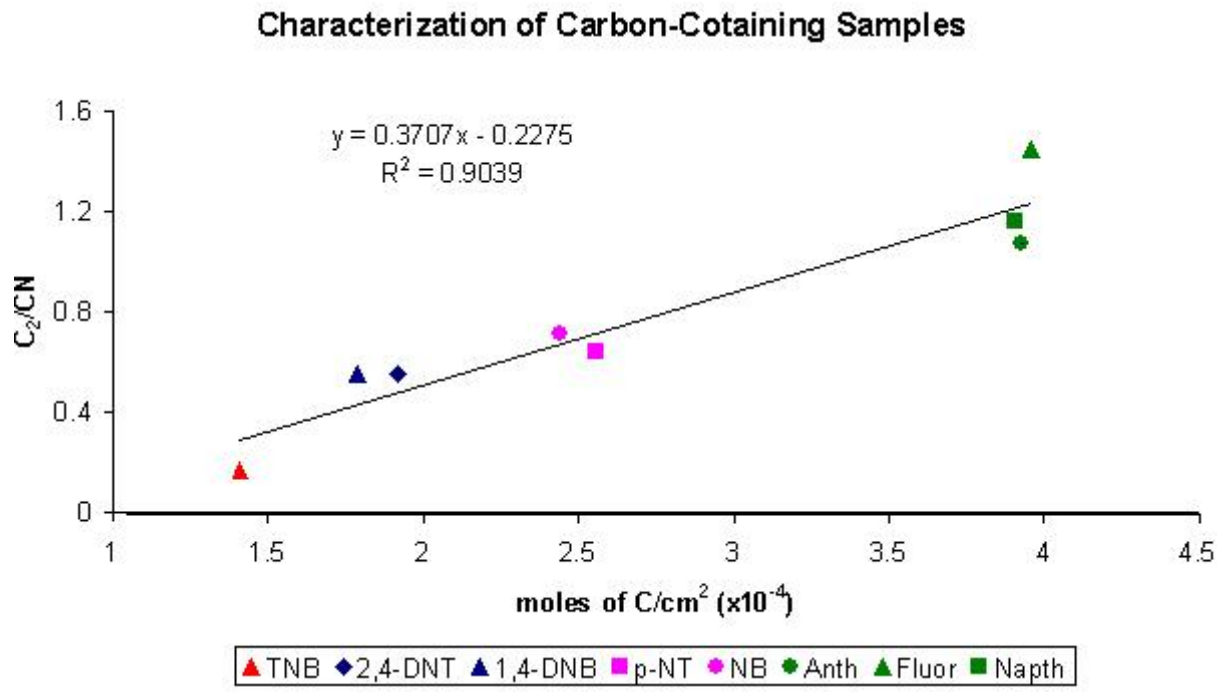

Figure 45: Characterization of carbon-containing samples by C_2/CN ratio obtained from LIBS analysis in an air atmosphere

There is significant grouping observed in the plot, which is based on the number of nitro functional group substituents and one group which is comprised of only PAHs. The C_2 (0-0) band was the most intense band for the PAHs, this led to these samples having a C_2/CN ratio greater than one. These results suggest a connection between the emission ratios and the moles of carbon for each sample. The oxygen atomic emission line, the nitrogen atomic emission line and the hydrogen α line were not used in this analysis because of the possibility of these emissions coming from molecules in the air atmosphere and not the sample.

There are two different effects that are can be observed from this plot. The first effect is that the C_2/CN ratio decreases with the decreasing surface concentration of the moles of carbon in the residue. The CN intensity observed was also affected by the nitrogen in the atmosphere. As the number of carbons increased in the sample, the more carbons there were to scavenge for nitrogen ions within the plasma. The amount of atmospheric nitrogen entering the plasma may be the same for each sample analyzed based on the high linearity of the points in Figure 45. The second effect is that the C_2/CN ratio increases as the number of NO_2 moieties attached to the sample decreases. As the number of nitrogen atoms in the analyte increases, so does the number of CN radicals that can be created, resulting in more intense CN bands and a decrease in the C_2/CN ratio. However, this emission generated from carbon and nitrogen atoms in the sample is affected by the nitrogen from the atmosphere.

Analysis in an Argon Atmosphere

To remove atmospheric nitrogen and determine which effect is the basis of the plot in Figure 45, 1000 ppm solutions of the samples were analyzed in an argon atmosphere using the capped cuvette setup (Figure 38.c). It will be shown that the air can be removed from the analysis with argon, refer to Figure 47. This effect will be addressed further in the next chapter. Unfortunately, CN and C_2 emissions were not observed in this study.

Analysis in an Atmosphere of Argon

Spectra collected under an Ar atmosphere suggest that experimental conditions may be found wherein atmospheric nitrogen contributions to CN emissions can be eliminated. Under those conditions it may be possible to determine if CN emissions originate from C and N atoms from the analyte. It is the objective of this study to determine information of the molecular structure without the influence of atmospheric elements.

Sample Preparation

Most of the samples used in this experiment were solids: either crystals or powders. Crystalline samples with single particle sizes exceeding the laser focal spot size were analyzed without pressing into a pellet form.

For the powdered samples, a method was developed for analysis that would minimize that amount of particles scattered. Two methods were created to analyze these types of samples in a solid form. The first method consisted of using a KBr pellet press to obtain samples. The second method consisted of preparing explosive samples inspired from composition C-4, which is a composite of RDX and binders at a ratio of 9:1. One hundred microliters (100 µL) of a highly concentrated polyisobutylene:hexane solution was weighed out and the hexane was allowed to evaporate in a fume hood. The polyisobutylene that remained in the mold was used to determine the amount of sample necessary to form a 9:1 ratio by weight. The samples were weighed out and covered with 100 µL solution of polyisobutylene:hexane. When the hexane evaporates from the isobutylene mixture the final ratio of the sample to isobutylene was approximately 9:1 by weight. Some samples had a low density and when these samples were weighted out in the mold, the polyisobutylene solution did not cover the entire sample volume and the resulting ratios for these samples was not 9:1.

Isobutylene was chosen as the binder because it is not observed to produce a LIBS spectrum of that is representative of its chemical makeup, refer to Figure 46. The only peaks present in the spectrum are calcium, sodium and the alpha hydrogen line. All of which can be acquired from the surrounding air atmosphere or contaminants located on the surface of the polyisobutylene sample.

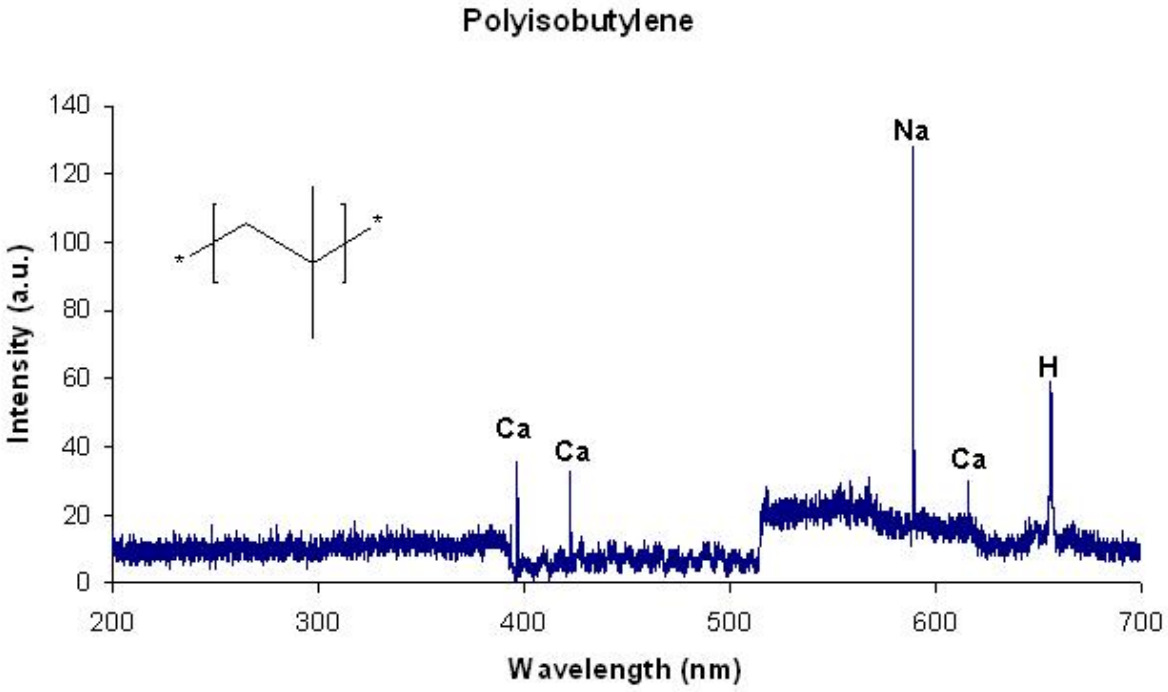

Figure 46: A representative spectrum of polyisobutylene analyzed in air. Only Ca, Na and hydrogen (α) peaks are present in this spectra.

LIBS Experimental Method

The samples were removed from the mold and placed in a quartz absorption/fluorescence cell. To ensure that the atmosphere surrounding the LIBS event was argon, a cap was placed over the cuvette to prevent argon from leaving the cuvette (Figure 38.c). The laser was focused to analyze the sample's surface. The spectrometer delay was set to 2.5 μs and the laser was set to approximately 50 mJ. Ten (10) single-shots spectra were obtained per sample and subsequently averaged.

Results and Discussion

Removal of Atmospheric Air

Figure 47 illustrated the affect of an air atmosphere on the analysis of graphite. Violet CN bands are present in spectrum of graphite analyzed in air. Under an argon atmosphere these bands are not observed and the spectra are dominated by the atomic carbon peak and the Swan C_2 bands. This demonstrates the experimental removal of atmospheric N_2 and therefore CN species formed in the plasma. The spectra illustrated in Figure 47 and Figure 48 are normalized to the C_2 peak.

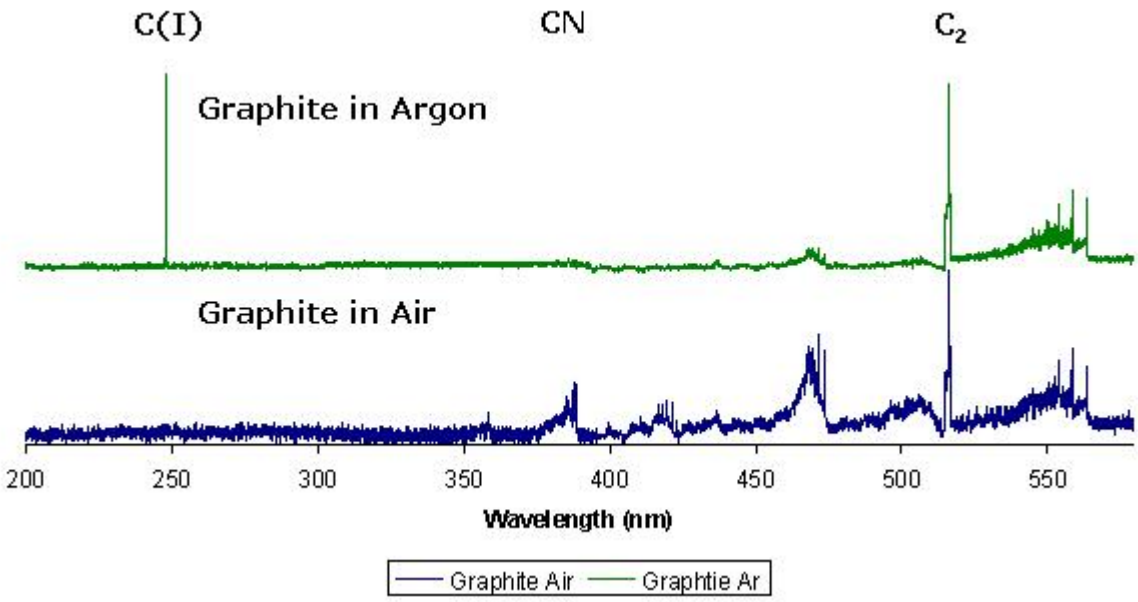

Figure 47: LIBS spectra of graphite analyzed in an air and an argon atmosphere

Illustrated in Figure 48 is the analysis of polyacrylonitrile (refer to Table 27) in air and argon atmospheres. This sample contains a cyano group ($C \equiv N$) and the violet CN

bands are present in both the air atmosphere and the argon atmosphere (Figure 48). The CN bands observed under the argon atmosphere are less intense than those in the air atmosphere, which may be due to the limiting amount of nitrogen in the sample compared to the excess amount of nitrogen from air.

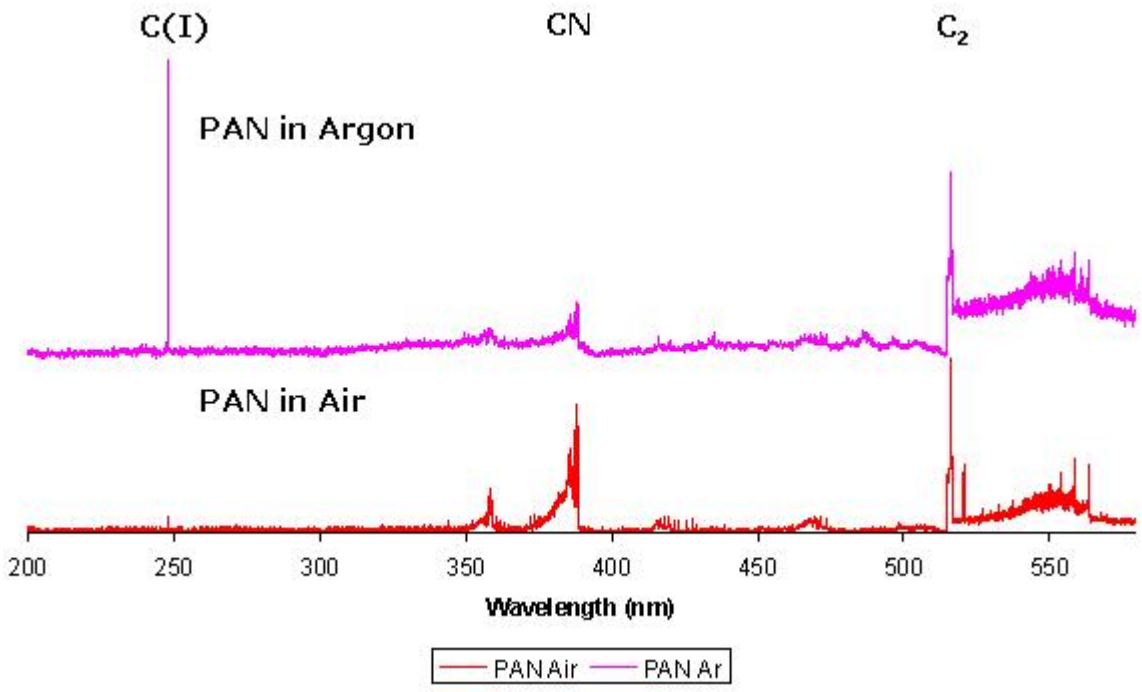

Figure 48: LIBS spectra of polyacrylonitrile (PAN) analyzed in an air and an argon atmosphere

Atmospheric Effects on Characterizing Nitrogen Containing Samples

To observe the effects of atmospheric oxygen on the resulting LIBS spectra, PCA analysis were performed to identify groupings of organic molecules with and without nitrogen atoms. The samples analyzed in this study included: trinitrobenzene, 2,4-

dinitrotoluene, 1,4-dinitrobenzene, p-nitrotoluene, nitrobenzene, anthracene, flouranthene and naphthalene (refer to Table 27). These samples were analyzed in an air atmosphere and an argon atmosphere.

Principal component analysis was performed on the emission intensities of C (I), CN, C_2 and O (I). The intensities of these peaks were required to have a S:N greater than 3:1 to be included in the analysis. The data set containing the C (I), CN and C_2 emission intensities were normalized such that each set of emissions comprised a unit vector. Unit vectors were calculated for the data set containing C (I), CN, C_2 and O (I) emission intensities as well to determine the influence of oxygen on characterizing organic materials. To calculate unit vectors, each emission intensity for a single analyte was divided by the square root of the sum of squares of all the included intensities, refer to equation 35.

$$\frac{X_i}{\sqrt{\sum_{i=1} (x_i)^2}} \qquad \textbf{(35)}$$

Principal component analysis was performed on the unit vector values calculated for each sample. The samples were assembled into four main groups: samples with three nitro groups, samples with two nitro groups, samples with one nitro group and polycyclic aromatic hydrocarbons (PAHs) with no nitrogen or oxygen atoms. Principal components PC1, PC2 and PC3 were used for grouping based on the scree plot. Illustrated in Figure 49 are 3-D PC plots that demonstrate the effects of atmospheric

oxygen. Plots A and B are based on the unit vectors calculated from the intensities of the C (I), CN and the C_2 bands. Whether analyzed in argon (A) or in air (B), groupings can be observed based on the number of nitro groups located in the sample. When the intensity of the atomic oxygen peak (777 nm) is included in the unit vectors for analysis in the air atmosphere (refer to plot D), the groupings previously observed in plot B are not present in plot D. This may be based on the influence of oxygen peak intensity, since the intensity is mostly acquired from the atomization of the atmosphere. Under an argon atmosphere, when oxygen was incorporated groupings were still observed; refer to plot C in Figure 49. Incorporating the oxygen intensity did not seem to adversely affect the groupings observed when analysis was performed in an argon atmosphere. The oxygen emission intensity observed under an argon atmosphere is a result of only the oxygen atoms present in the sample itself. Therefore, it should not adversely affect the groupings, but could potentially enhance groupings.

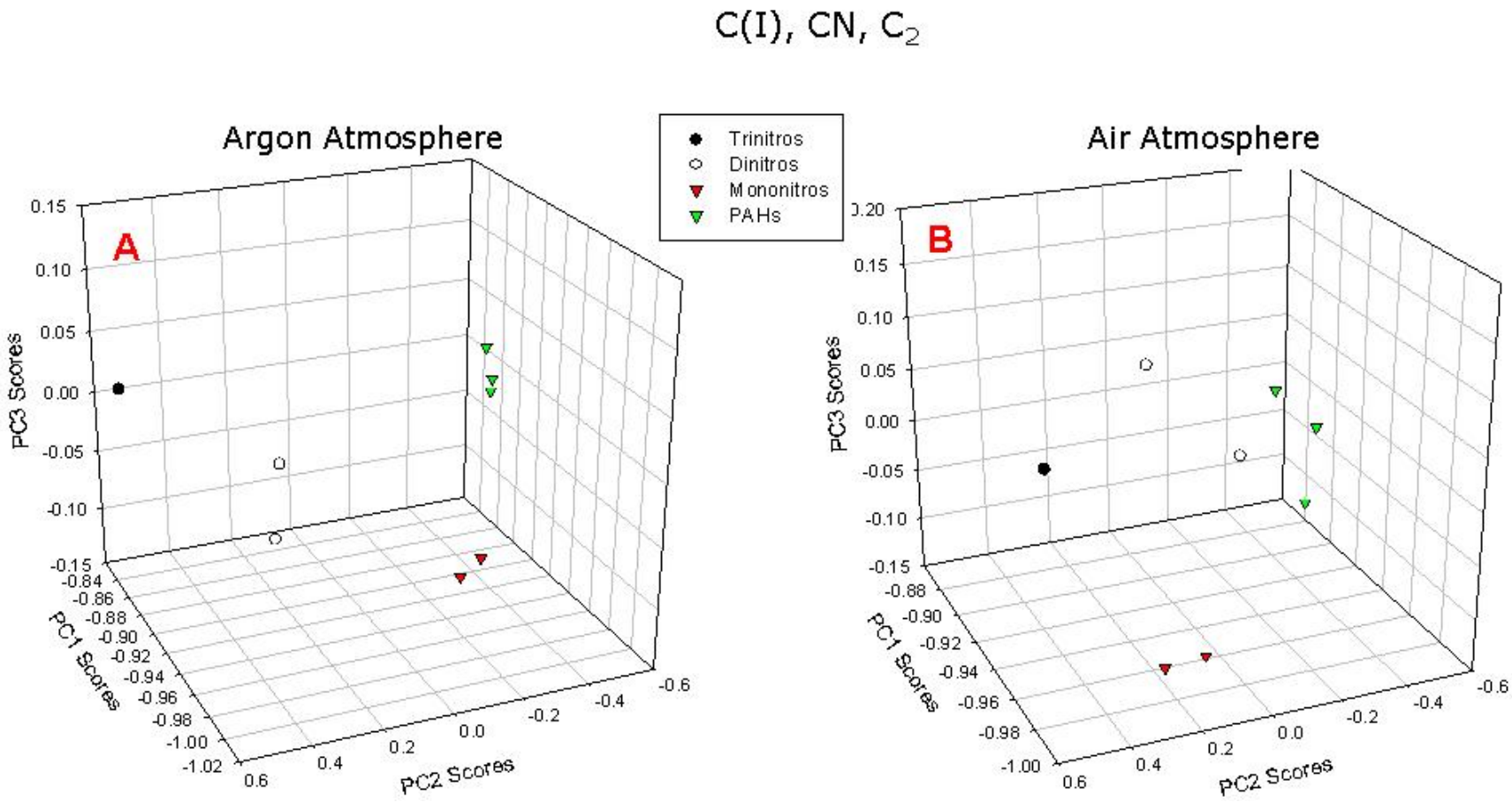

Figure 49: Effects of atmospheric oxygen on characterizing organic samples from resulting LIBS spectra. (a) PCA plot based on the intensities of C (I), CN and C_2 in an argon atmosphere. (b) PCA plot based on the intensities of C (I), CN and C_2 in an air atmosphere. (c) PCA plot based on the intensities of C (I), CN, C_2 and O (I) in an argon atmosphere. (d) PCA plot based on the intensities of C (I), CN, C_2 and O (I) in an air atmosphere.

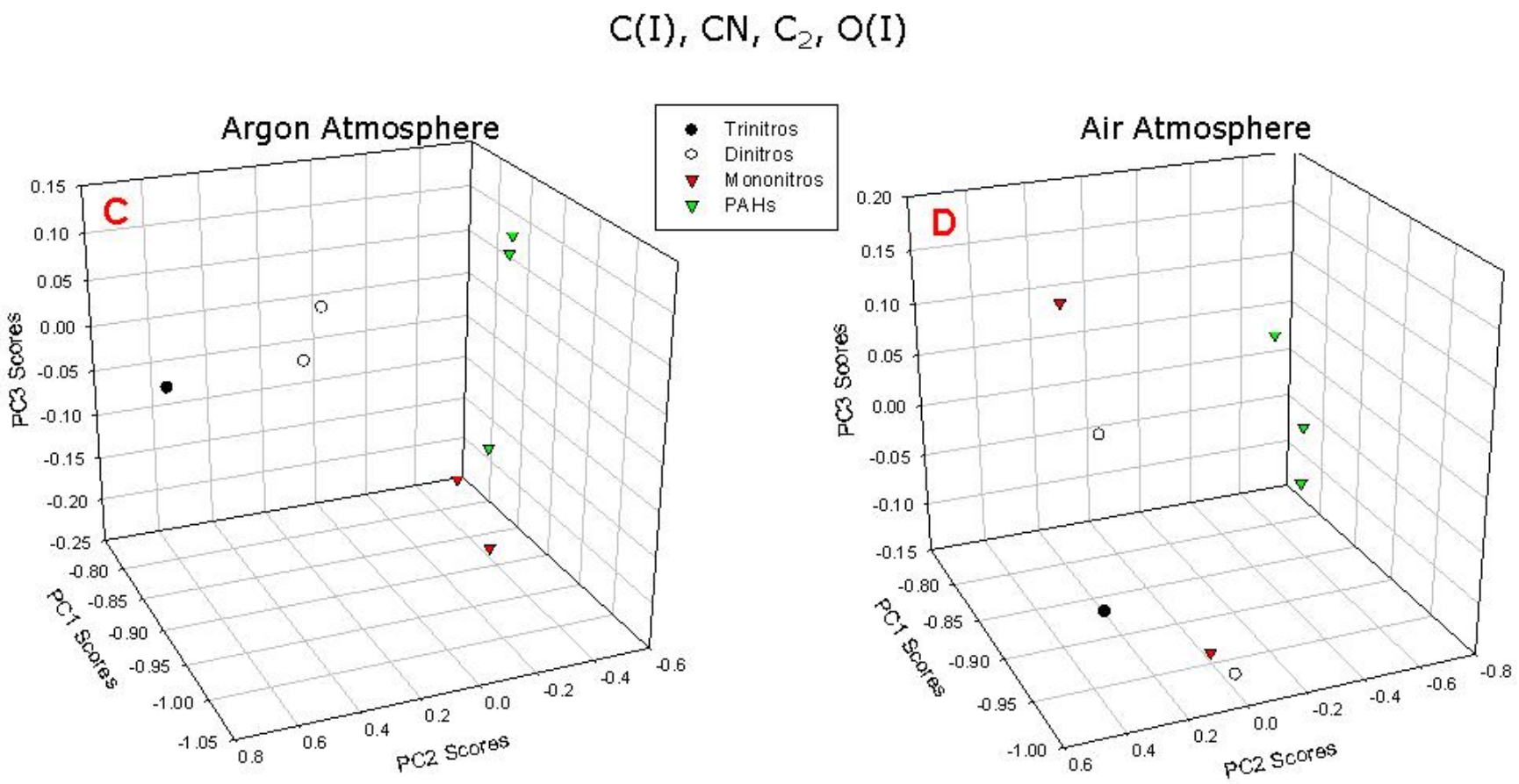

Figure 49: Effects of atmospheric oxygen on characterizing organic samples from resulting LIBS spectra

Study of Explosive Materials in Argon Atmosphere

This study included energetic materials, polymers and oxygen rich materials. Samples analyzed in this study are listed in Table 27. In the absence of atmospheric air, the presence of hydrogen, nitrogen and oxygen emissions can be included with atomic carbon and the diatomic species emissions in the overall analysis and characterization of these molecules. The intensities of these peaks were required to have a S:N greater than 3:1 to be included in the analysis. Samples containing oxygen atoms and nitro moieties (NO_2) produced spectra with atomic oxygen (777 nm) emissions. Atomic nitrogen peaks (746 nm) were not present in most of the spectra collected. The only sample in this study that showed any atomic nitrogen in the resulting spectrum was 2,4-DNT, which may be evidence of how the CN radicals are generated in the plasma. The data set containing the C (I), CN and C_2 emission intensities was normalized such that each set of emission comprised a unit vector. The unit vectors were also calculated for the data set comprised of the C (I), CN, C_2 and O (I) emission intensities.

Cyclotrimethylenetrinitramine (RDX) was included in this study to determine if N_2 diatomic vibrations are evident in emission spectra. RDX is a nitramine which contains N-N bonds in its structure (Table 27). The most intense N_2 vibronic emissions are located at 635 – 655 nm for the $B^3\Pi \rightarrow A^3\Sigma$ where $\Delta\upsilon = +3$ and at 372 nm – 382 nm for the $C^3\Pi \rightarrow B^3\Pi$ where $\Delta\upsilon = +2$.[112, 113] These emissions were not observed in the

spectra acquired for RDX. This is possibly due to either poor intensity of these emissions or N_2 was not generated in the plasma.

Principal component analysis was performed on the set of unit vectors constructed from each sample. The samples were assembled into three main groups: nitro (NO_2) containing, cyano (CN) containing and carbon only compounds. Principal components PC1, PC2 and PC3 were used for grouping based on the scree plot. Illustrated in Figure 50, are the groupings of the three types of organic materials based on all three PCs.

There is some grouping of the samples in plot A of Figure 50; however, more distinct groupings are observed in plot B with the incorporation of the oxygen atomic peak. Samples with nitro groups in the structure cluster close to other nitro containing samples. Carbon only samples cluster apart from the samples with nitrogen atoms. Samples with cyano groups cluster close to one another and as a group, closer to the nitro containing group. In plot B, a few outliers are observed. The first outlier is a carbon sample that grouped with the nitro samples. This sample was poly(acrylic acid) (PAA) and contains carbon and oxygen (refer to Table 27). In plot A, PAA was grouped with the carbon only samples, because characterization was based on only the C (I) and the C_2 emission; the CN band was not used for characterization because there were no CN bands observed in the resulting spectra. Referring to plot B, the intensity of the oxygen peak was able to separate this sample from the other carbon only samples. While using the C (I), CN and C_2 peak provides some characterizing information about

the sample, it is evident from the plots in Figure 49 and Figure 50 that using the oxygen atomic peak is important in accurately characterizing the type of organic molecule as long as the oxygen emission occurs from oxygen atoms in the sample and not from the atmosphere.

Similar studies incorporating the emission intensity of the nitrogen atomic peaks was examined. However, LIBS analysis of these organic materials under an argon atmosphere produced little to no N (I) peaks (746 nm) at a S:N ratio greater than 3. It is possible that if nitrogen was present in the sample, nitrogen ions would recombine with carbon ions at a greater probability producing CN bands rather than recombining with ions to produce atomic nitrogen bands. Based on the little or no N (I) intensities observed in the resulting LIBS spectra, using the atomic nitrogen band did not affect the overall results of the PC analysis of these organic molecules.

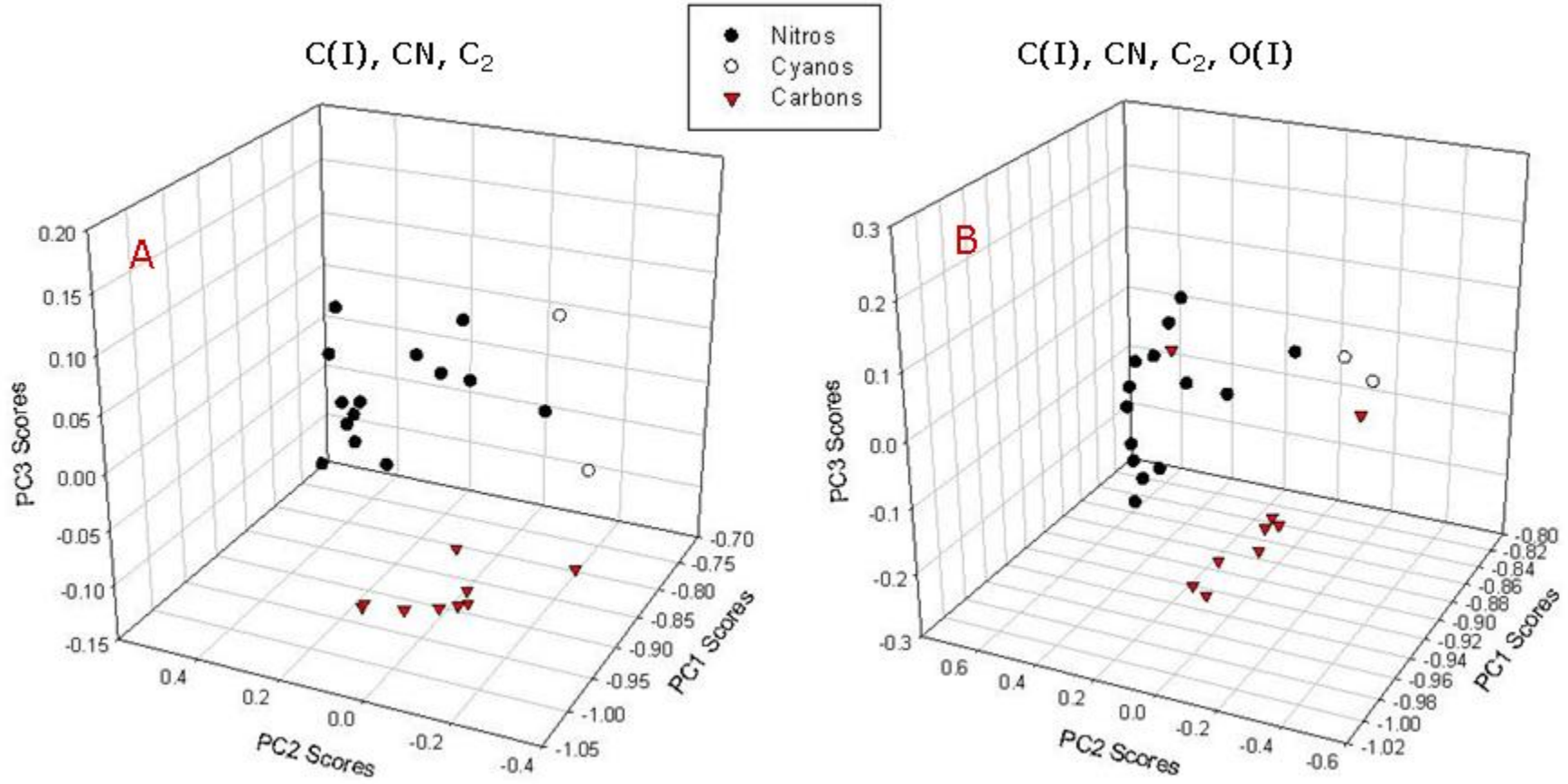

Figure 50: 3-D PCA plot of organic materials containing cyano, nitro and carbon only moieties analyzed in an argon atmosphere. (a) PCA plot based on the unit vectors of the C (I), CN, and C_2 peaks. (b) PCA plot based on the unit vectors of the C (I), CN, C_2 and O (I) peaks.

Analysis of 2,4-DNT at Different Concentrations

The intensities of the CN and the C_2 vibronic bands from 2,4-DNT were examined on copper at three surface loadings, resulting from the deposition of 100 μL of 1000 ppm, 16.7 ppm and 0.278 ppm solutions. The 2,4-DNT surface loadings are given in Table 28. LIBS spectra were recorded in air with an argon flow directed over the sampling area. The presence of air during this study allows for the incorporation of atmospheric nitrogen which alters the CN emission intensity from the sample itself; however, the amount of carbon remains the same.

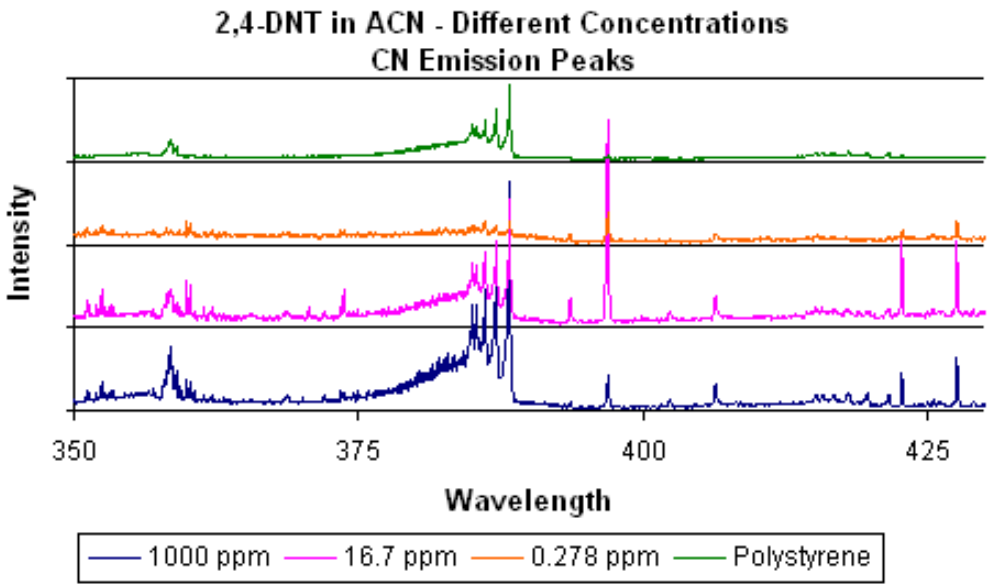

Figure 51: Spectra of 2,4-DNT at different concentrations analyzed in an air atmosphere

The area around the C_2 (0-0) peak is expanded in Figure 52 to show how this peak disappears as the surface loading decreases. While, the CN peaks are still visible in the

spectra resulting from the analysis at a surface concentration of 18.1 ng/cm^2, the C_2 (0-0) emission is not observed, refer to Figure 52.

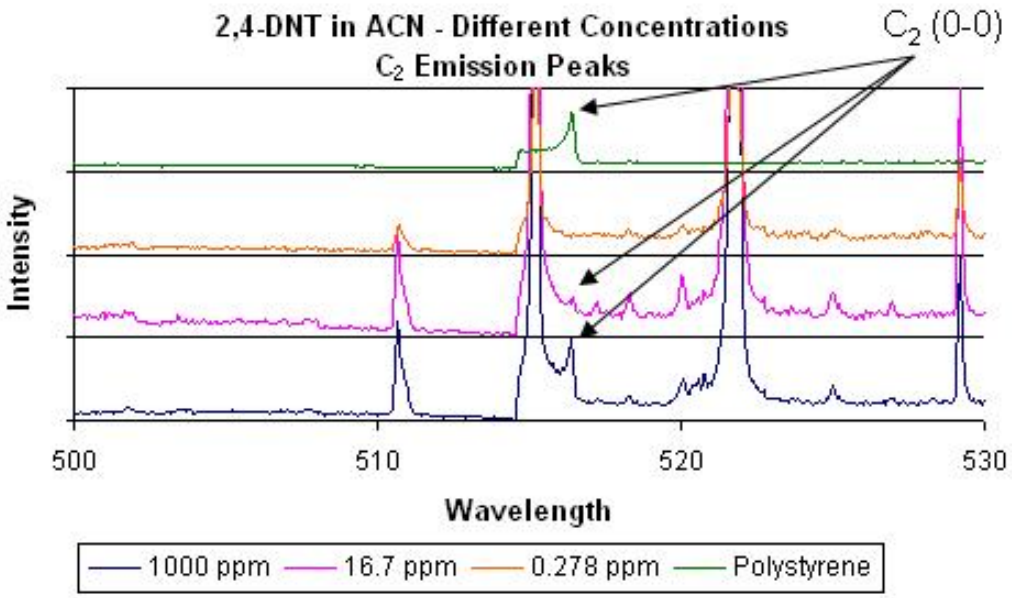

Figure 52: C_2 (0-0) bands of 2,4-DNT at different concentrations analyzed in an air atmosphere

A non-linear relationship between the surface concentration of 2,4-DNT and the intensity of the CN (0-0) peak was observed, Figure 53. This curve shows a detection limit of 2,4-DNT at the surface concentration of 18.1 ng/cm^3 in the presence of air. A similar plot was created for the C_2 (0-0) emission band at 516.50 nm, where R^2 = 0.95.

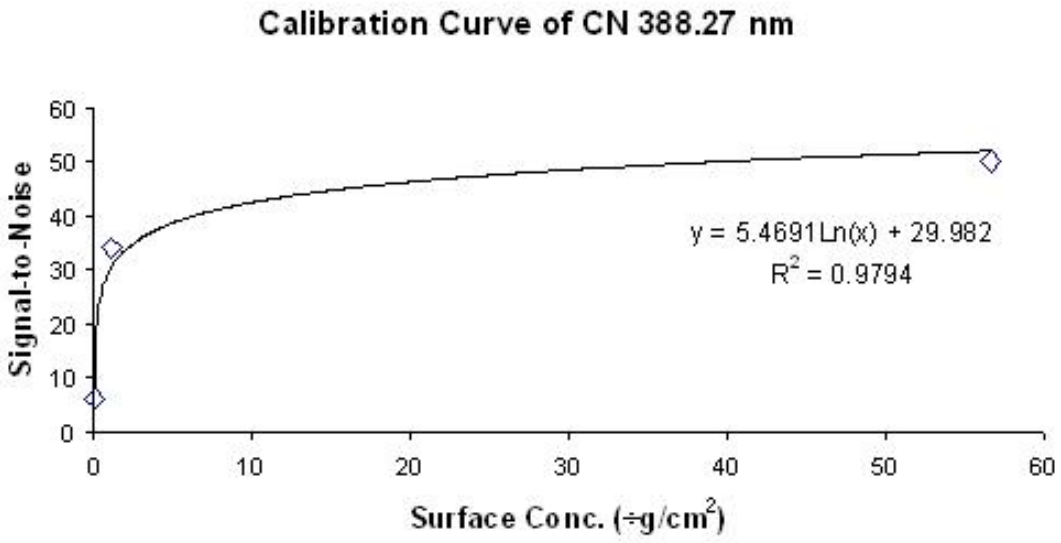

Figure 53: Calibration curve of the CN (0-0) peak of 2,4-DNT analyzed in air on a copper support

Table 28: Surface concentrations of the 2,4-DNT on a copper substrate at different concentrations in an air atmosphere

2,4-DNT/ACN Conc. (ppm)	Surface Conc. (μg/cm^3)	Intensity
1000	56.6	552
16.7	1.085	307
0.278	0.018	56

A similar study was conducted for samples under argon, using the apparatus in Figure 38.c. Samples of 2,4-DNT in ACN solutions were prepared at three concentrations: 1000 ppm, 33.3 ppm and 1.1 ppm. 40 μL of 2,4-DNT in ACN at each concentration was deposited onto a copper support and the solvent was allowed to evaporate in the face

of a chemical fume hood. CN and C_2 diatomic emissions were recorded only from the analysis of a residue with a surface concentration of 56.6 μg/cm^2; therefore, calibration curves could not be created. With the removal of atmospheric nitrogen the CN bands are created solely from the nitrogen atoms present in the sample which will significantly decreased the intensity of the CN bands and thereby increase the detection limits. A decrease in the intensity of the C_2 bands is also observed under an argon atmosphere; however, it is unclear at this time why this occurs.

Argon has been shown to increase the spectral emission intensity with respect to other gases, such as helium. With the increase of the spectral intensity, argon also increases the background noise. The density of argon and air, 1.78 g/L and 1.23 g/L, are similar; therefore, the "confinement effects" from the atmosphere should be approximately the same leading to similarly intense spectral emission of diatomic species.[114] Confinement effects are defined as the effect that the surround gas has on the expanding plasma. Dense gases have more of an effect because it is more difficult for the plasma to expand in this atmosphere versus a less dense gas or in a vacuum. It is not understood at this time why the intensities between the 2,4-DNT emission obtained in the two atmospheres are significantly different.

Conclusion

It is possible to identify explosive or energetic material based on LIBS spectra; however, appropriate parameters should be identified prior to analysis. While it has been previously reported that explosives can be identified based on violet bands, swan bands, atomic carbon peaks, hydrogen α peak, atomic oxygen peaks and/or atomic nitrogen peaks, these studies were all done in an air atmosphere.[108-111] However, to garner more information about the molecular structure of the explosive or organic material for identification purposes the atmosphere at the time of analysis should be that of an inert gas. This would remove any interferences of the air atmosphere on the resulting spectrum. In this study, it has been shown that sampling in an inert atmosphere may be important because this provides information on the molecular chemical structure by exciting only the atoms in the sample. While this approach might not be practical for long distance sampling with LIBS, it is important for general identification of explosives and organic materials in addition to developing a relationship between the LIBS spectrum and the molecular structure.

CHAPTER NINE:
AUTOMOBILE PAINT DISCRIMINATION

Automobile paints are a common physical evidence submitted in automobile accidents.[115] Automobile paints are comprised of many layers. Generally, sedan automobiles have three coats: a clear top coat, a color coat and a primer coat. Some samples may contain more than one primer layer.[116] Trucks, SUVs and bumpers usually have two layers: a clear top coat and a color coat. Automobiles that have been repainted are more unique because there are more than four paint layers present. Repainted layers are generally thinner than the original factory paint layers. In the sample set examined here, paint samples from repainted vehicles had a maximum of 12 layers of paint. Not only is the number of observed layers a comparison point, the thickness of each individual layer can be another point of comparison between known and unknown samples. However, it is important to note that due to weathering or improper after-market painting, the layer thickness can be inconsistent from point to point on the same sample. Therefore, other methods of analysis are necessary. For this type of multi-layer sample, each layer of paint must be compared to the same layer from the other paint sample.

The Royal Canadian Mounted Police (RCMP) and the Federal Bureau of Investigation (FBI) have developed an FTIR library of automobile paint samples for a wide range of manufactures, models, colors and years which is available to any forensic laboratory.

Each layer is analyzed by FTIR and the resulting spectra are run against this library for a match. While the top clear coat may not provide much discriminatory information, the color coat does. This is because the color used is specific to a particular manufacture and even make of car. This can provide a source of the paint sample in cases were there is no automobile in question. Ryland et al. studied using FTIR to discriminate the non discriminating clear and primer coats.[117, 118]

One hundred and three samples were collected from local salvage yards (Orlando, FL and Columbia, SC). This set of samples represents a range of automobile makers, models, colors and year manufactured (1987 - 2006). One paint sample was analyzed twice and to give a total number of samples analyzed of 104 samples which allowed for 5,356 unique pairwise comparisons.

FTIR-ATR

The Fourier transform infrared – attenuated total reflectance method is usually the instrumentation used to identify the type of polymeric based clear coat of an automobile paint sample. There are eleven major types of clear coats: epoxy, alkyd, nitrocellulose, acrylic-alkyd, urethane modified acrylic-alkyd, acrylic lacquer, acrylic-urethane, alkyd-melamine, epoxy-melamine, acrylic-melamine, and polyester-melamine. A standard flow chart, developed by Ryland, is employed to identify the type of clear coat finish. Based on the presence and/or absence of vibrational peaks, the type of

clear coat can be identified and even separated into an original finish or a repainted finish.[116]

FTIR-ATR Experimental Method

Spectra were collected at three different locations of the clear coat for each automobile paint sample. Without any further sample preparation, only the clear coat of the sample was analyzed by this method. Paint samples still affixed to the original automotive substrate the sample was considered a "hard" sample. This was true for repainted paint chips because the increased number of paint layers increased the rigidity of the sample itself. Chips of original paint samples were considered a "soft" sample. Each sample was placed on a pressure sensor plate and the ^{32}Si crystal attachment was set on top of the sample until the contact registered between 2 – 4 mA for soft samples and 5 – 9 mA for harder samples. The interferrogram had a really low intensity initially; therefore, the gain was set for automatic adjustment. Thirty-two (32) scans were taken per sample acquisition and the resolution was set to 4 cm^{-1}. Background samples of the air atmosphere were acquired after the sample spectra and subsequently subtracted to give the actual IR spectra of the sample. Fifty-one (51) samples were analyzed on two different days, approximately one week apart.

Typical FTIR-ATR spectra are illustrated in Figure 54, where there are many similarities such as the C-O stretch ~ 1200 cm^{-1}. The unique stretches in the fingerprint region are the significant differences that aid in differentiation of the clear coat. The Ryland IR classification flowchart[116] was used to identify the clear coat on each sample.

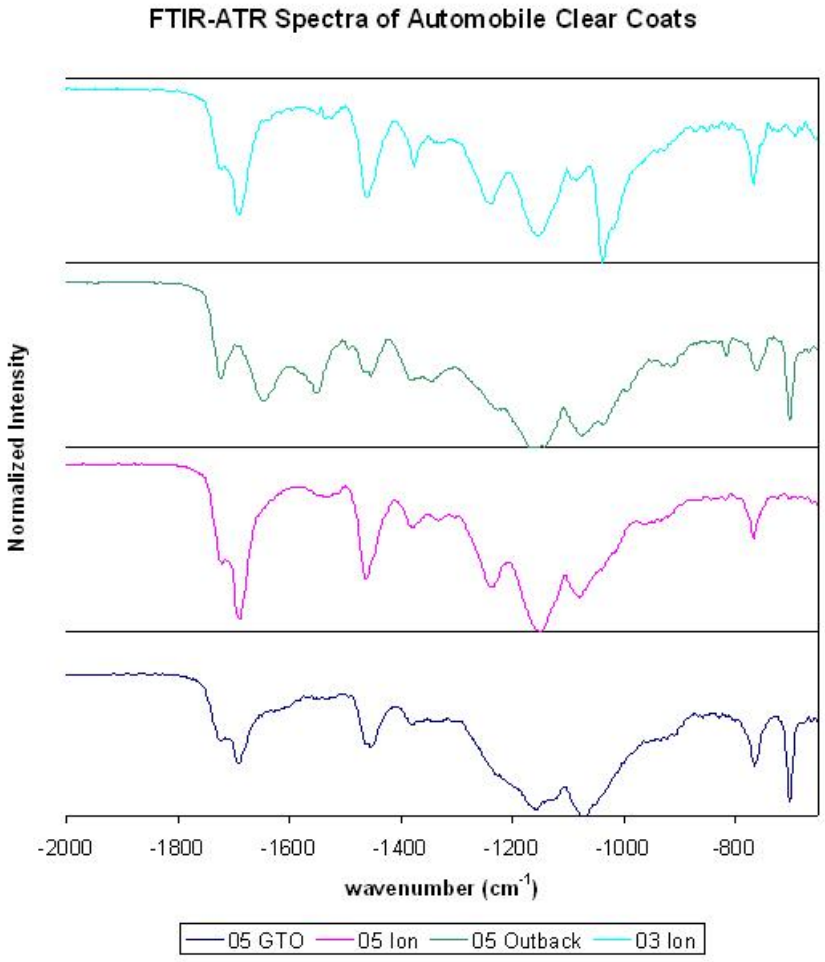

Figure 54: FTIR-ATR spectra of automobile paint clear coat

PCA Analysis

Principal component analysis was performed on the FTIR spectra collected for each automobile clear coat sample. Each FTIR spectra was normalized to the most intense peak prior to PCA analysis. Cluster analysis based on single Euclidean linkage was used to identify samples that were similar based on the scores of the first three principal components, refer to Figure 55. Based on the 3-D PC plots illustrated in Figure 56, the groupings obtained from the cluster analysis are not comparable to the grouping based on the Ryland classification.

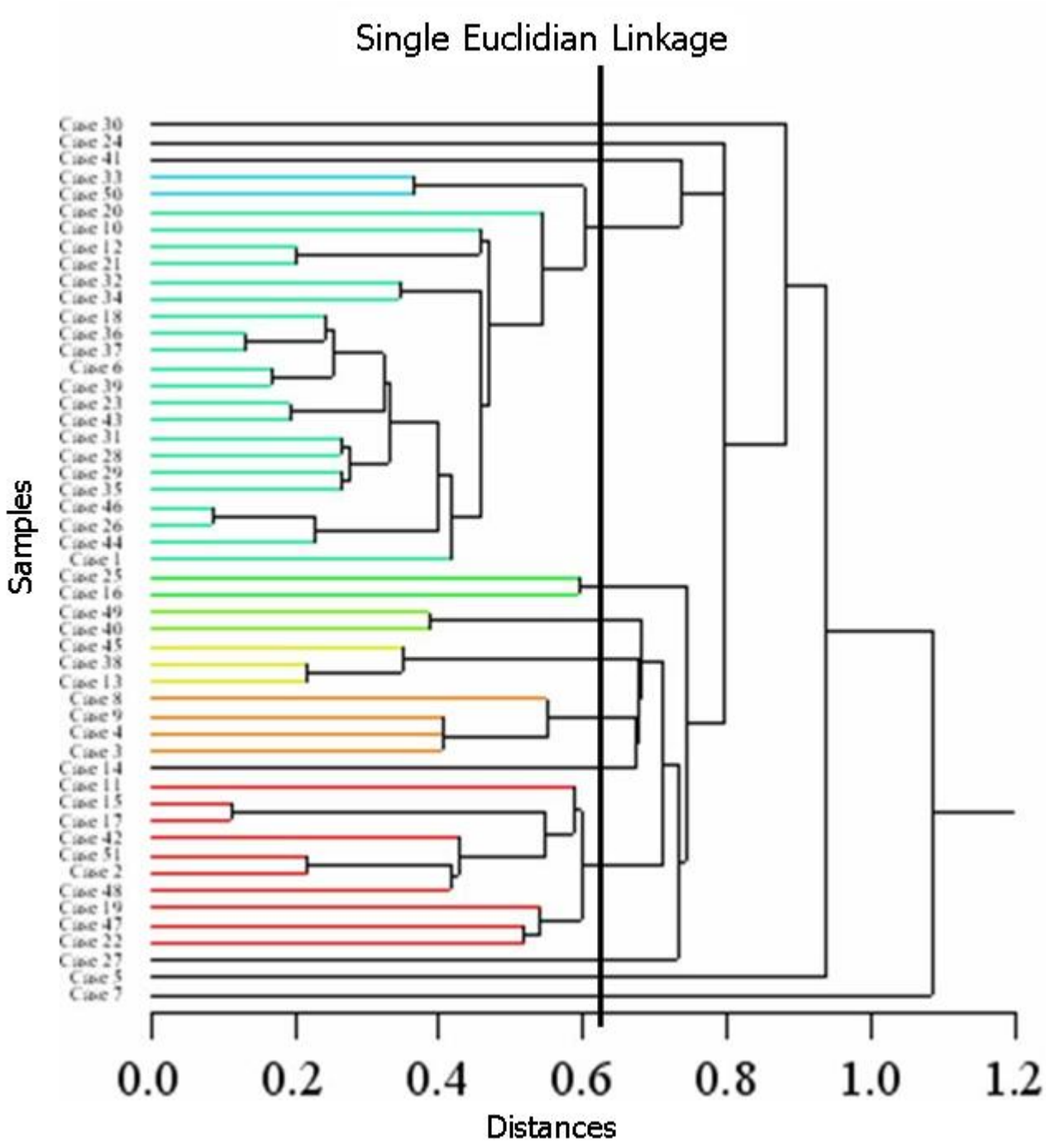

Figure 55: Single Euclidean linkage cluster analysis of normalized FTIR spectra of automobile clear coats

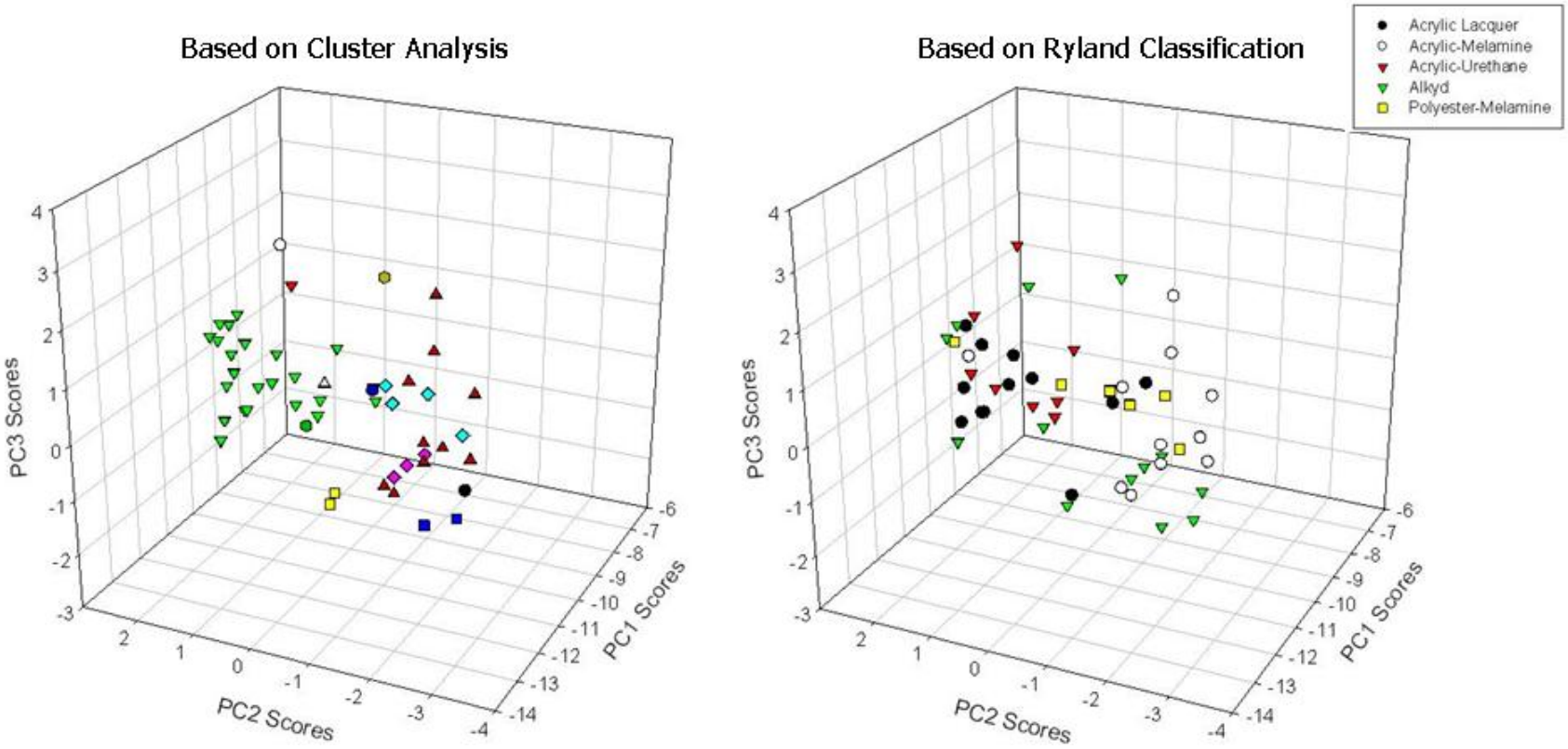

Figure 56: Principal component analysis of normalized FTIR spectra of automobile clear coats. The groups are identified based on cluster analysis and Ryland Classification.

Student's *t*-Test/HQI Library Search

The Euclidean distance was used to determine the potential of using a library search to correctly identify ATR spectra. Three FTIR-ATR spectra were collected for each of the 51 samples. The first spectrum collected was placed into a library and the other two replicate spectra were run against the library to search. The pairwise comparison between replicate spectrum and the library spectra with the lowest HQI value was deemed to be the most similar. Based on this comparative method only 70 replicate spectra were identified correctly out of a total possible 102 (68.6%).

Data Retrival based on the HQI Calculation

To determine if the FTIR-ATR spectra would be useful for creating a searchable library the HQI values were calculated for each pairwise comparison. Each spectrum discriminated was comprised of an average of three individual ATR spectra. The HQI values calculated for all sample with a sample classification based on the Ryland IR classification flowchart were deemed a true correct value. True incorrect values were HQI values between samples of different classifications. Twenty-three (23) samples were used for this analysis, which leads to 253 pairwise comparisons.

The ROC plot calculated for the ATR comparison of automobile clear coat samples is given Figure 57. The area under the curve for this comparison is 0.70 which is not good value if an area = 0.5 depict randomness. This area means that there is a 70%

probability of recovering the correct match at a lower HQI than an incorrect match. The dot histogram also illustrated in Figure 57, provides a histogram of the HQI values obtained for the correctly and incorrectly identified comparisons.

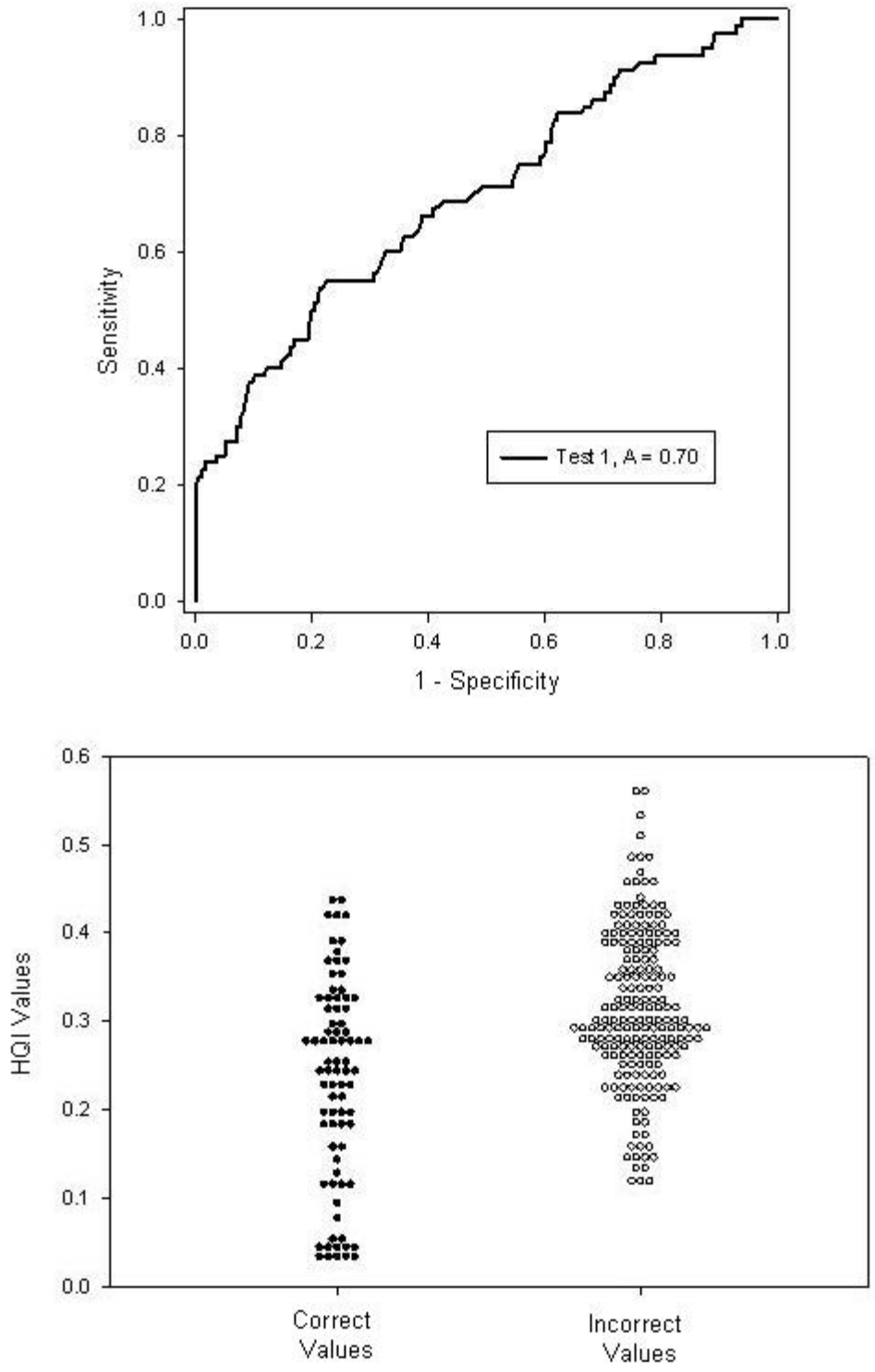

Figure 57: ROC plot and a dot histogram of the XRF comparison of the automobile paint clear coat samples based on HQI values

In comparison to the percentage correctly identified in the first library search, approximately 69%, the ROC plot seems to provide comparable information. While most of the samples are correctly identified, it does not seem to be sensitive enough at this time to create a library search based on these results from the automotive clear coat.

LIBS

Chapter eight discussed using diatomic species to determine the differences between organic samples. This approach was used to examine the possible discrimination of automobile samples based on identifying the nature of the top clear coat. The clear coat is polymer based and mostly comprised of carbon, oxygen and hydrogen. Most instrumental methods do not focus on analyzing these elements and consequently, the clear coat is hardly used for sample comparison or discrimination. In this study, the clear coat was interrogated with LIBS to use diatomic species to classify the type of polymer based clear coat used for the sampled automobile paints. This method is compared to the FTIR-ATR method described above.

LIBS Experimental Method

Seventeen samples were collected and grouped based on their FTIR-ATR spectra and the Ryland classification scheme.[116] To determine the structure of the clear coat, five

single-shot spectra were collected in a cuvette under an argon atmosphere (refer to Figure 38.c). Argon was allowed to flow for approximately two minutes before the first analysis at a flow of 145 mL/min. Most of the samples were analyzed on their original substrate and cut to fit into a 1 cm quartz absorption/fluorescence cell. The samples that were collected as a paint chip, without a substrate, were affixed to a copper substrate by double sided tape and subsequently placed into the absorption/fluorescence cell.

Results and Discussion

Student's *t*-test/HQI Discrimination

Representative LIBS spectra of automobile paint clear coats are presented in Figure 58. Violet, swan and atomic carbon emissions are present in these spectra, but there are other peaks present which may differentiate these samples.

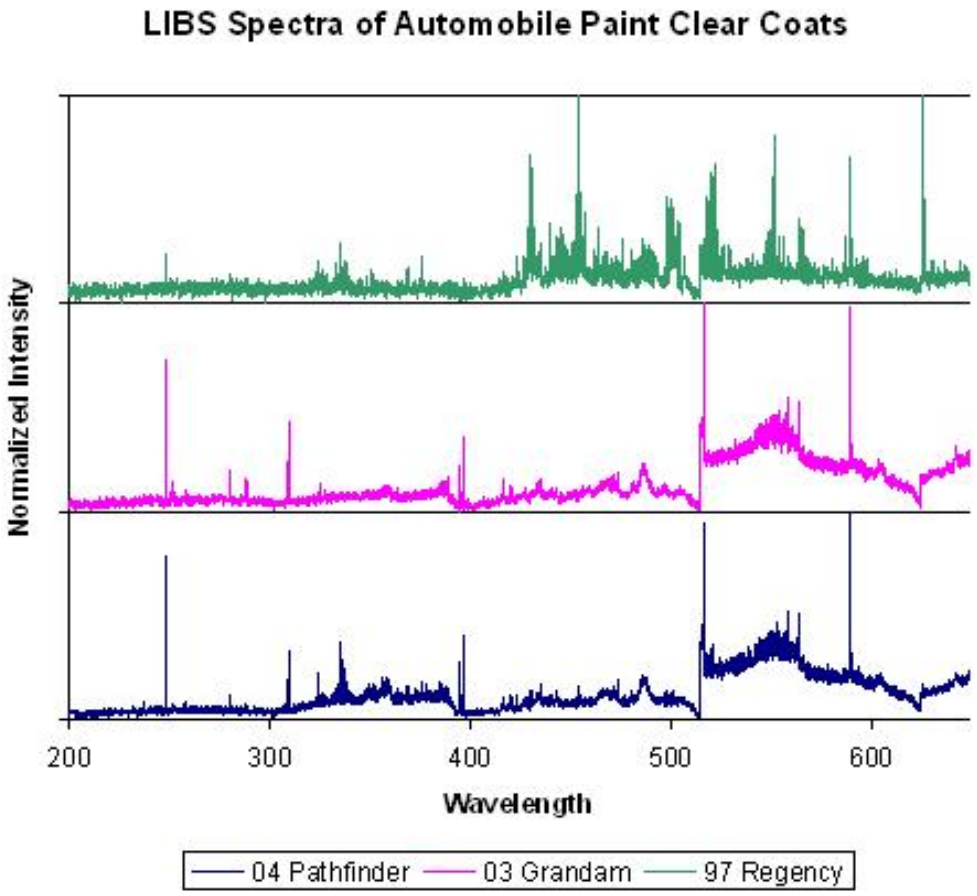

Figure 58: LIBS spectra of automobile paint clear coats

The full spectrum of the clear coat LIBS spectra were analyzed by the Student's *t*-test/HQI analysis. Even though the samples were collected under an argon atmosphere, the range of analysis was limited to 200 – 650 nm to prevent argon emission peaks from affecting the full spectral comparison. At a 95% CL, of the 17 samples (136 pairwise comparisons) 73.5 % of the samples were discriminated.

The Ryland IR classification flowchart[116] was used to classify the top clear coat for each sample which was used as a standard to compare the results of this technique. It was the purpose of this study to determine if two samples from the same Ryland classification group would be grouped similarly based on an analysis of their full LIBS emission spectrum. Samples classified correctly were identified as: (1) those of the same Ryland classification group that were not discriminated by the LIBS full spectral analysis and (2) those of different Ryland classification groups that were discriminated by the LIBS full spectral analysis. Samples classified incorrectly were identified as: (1) those of the same Ryland classification group that were discriminated (type I error) by the LIBS spectra and (2) those of different Ryland classification groups that was not discriminated (type II error) by the full LIBS spectral analysis. While 73.5% of the samples were differentiated from the others based on the full spectra, 66.9% were deemed as correct matches. Type I errors consisted of 13.2% of the comparisons made and type II errors consisted of 19.8% of the comparisons made. The poor correlation between the LIBS spectra and the Ryland classification of the automobile clear coats illustrated in this analysis was observed in the following principal component analyses of the LIBS spectra.

PCA Grouping

Full Spectral Analysis

Principal component analysis of the full LIBS emission spectrum of the paint clear coat was used to determine any groupings of similar clear coat samples. The samples were initially classified based on the Ryland IR classification flowchart and where subsequently plotted based on PC1, PC2 and PC3 to identify any grouping of samples from the same classification. An illustration of the 3-D PC plot is presented in Figure 59 and based on this method of analysis, there is no grouping observed. These samples were analyzed under an atmosphere of argon; therefore, the area of analysis ranged from 200 nm – 650 nm which would omit argon atmospheric peaks present in the spectra.

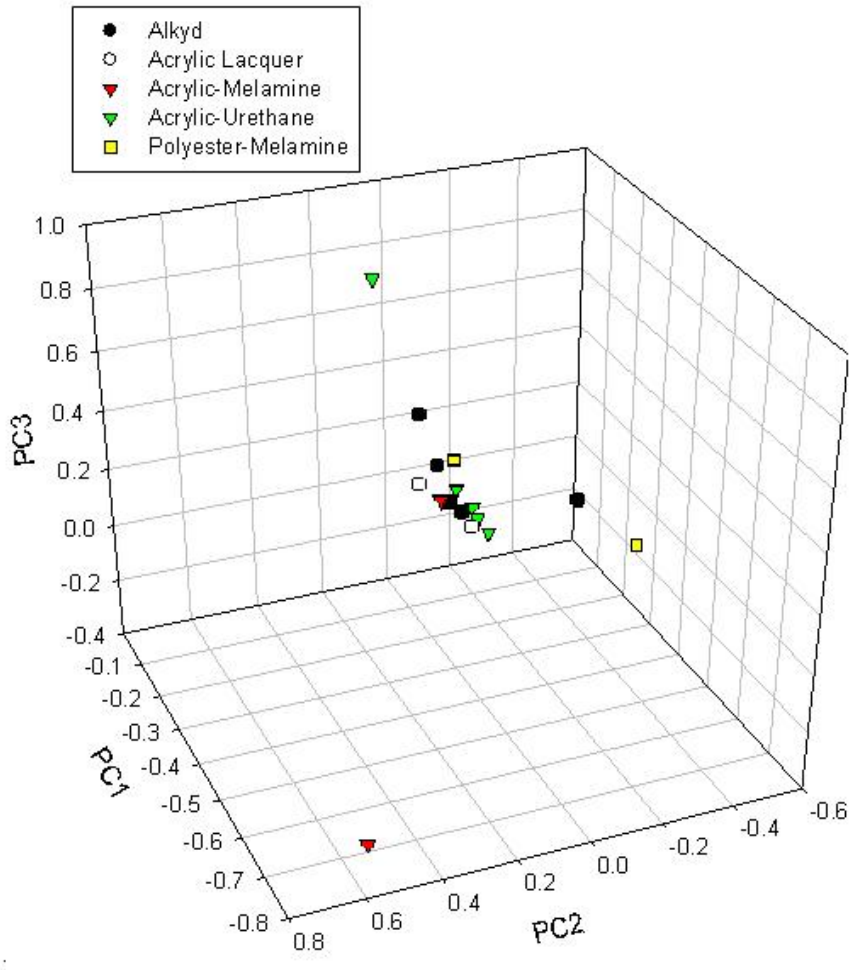

Figure 59: 3-D PC plot of automobile paint clear coat based on the full spectrum

Isolated Peak Analysis

There were no distinct groupings based on the full emission spectra, therefore, the intensities of isolated peaks was explored to determine if more distinct groupings could be observed based on the results of chapter eight. The intensities of the C (I), CN, C_2 and O (I) emissions were used for structural classification of the automobile paint clear coats. Peaks were only included in the analysis if the S:N was greater than 3:1. The

intensities collected were normalized to a unit vector of one. The five spectra collected per sample were averaged and the variance was calculated to determine the %RSD of each peak. From the representative LIBS spectra of clear coats illustrated in Figure 58, the diatomic species, CN and C_2, are clearly visible for two of the spectra. These peaks are still present in the third spectra (Regency) but have been obscured by other emission peaks which may be emissions from the color coat in addition to the clear coat.

PCA of isolated peaks was utilized to provide more distinct groupings of these LIBS emission spectra. Cluster analysis of the PCA scores using centroid Euclidian linkage was used to identify groups of similar clear coat samples, refer to Figure 60. From the cluster analysis, three groups could be identified and are illustrated in the 3-D PC plot in Figure 60. In addition to this analysis, samples were previously classified by the Ryland classification flowchart and samples are separated based on classifications as illustrated in Figure 60. A similar classification of the samples based on PCA of LIBS and Ryland classifications was not achieved. This may be due to the different type of information garnered from each technique. However, based on the grouping of similar samples that was observed in chapter eight, LIBS analysis of clear coat samples may be used to identify samples with similar clear coats without the used of the Ryland classification flowchart.

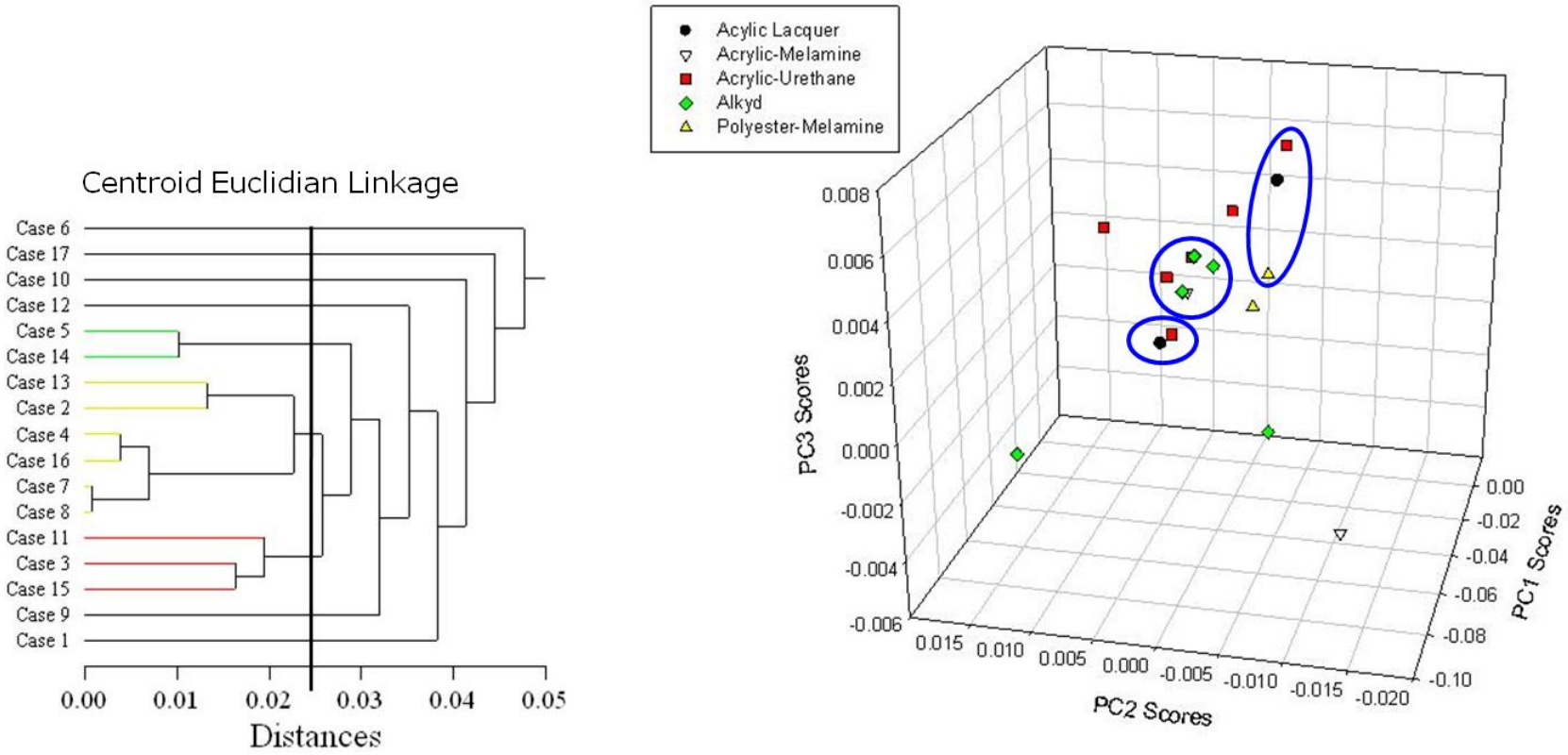

Figure 60: Cluster analysis of the PCA scores 1,2 and 3 based on the intensities of C (I), CN, C_2 and O (I) to determine groupings of automobile paint clear coat samples based on LIBS spectra. In the 3-D PCA plot, groupings from the cluster analysis are identified by the blue ellipses versus groupings based on the Ryland classification. The ellipses illustrated are not probability ellipses.

SEM-EDX

SEM-EDX Experimental Method

For this analytical technique, each layer of the cross section of each sample was analyzed. To obtain a viable cross-section, a thin layer of the cross section was removed with a scalpel, parallel to the direction of the layers. In the event that this method created curled, thin cross-sections, the ends were cut off to give flat cross section samples. Two to three cross-sections were cut per paint sample. Each thin layer of the cross section was placed on a carbon SEM dot for analysis. The samples were lightly coated in carbon to reduce electronic charging of the samples. For this reason, elements carbon and oxygen were removed from the analysis. Three measurements were collected per layer per sample.

SEM images of three automobile paint cross sections are shown below. The cross section depicted in Figure 61 shows a minimum of three layers: a clear coat, a color coat and the primer coat (from right to left). This image was obtained with a backscatter detector; refer the SEM-EDX section in chapter four. Based on the brightness and the contrast of the layers, three layers can easily be differentiated and subsequently analyzed by EDX.

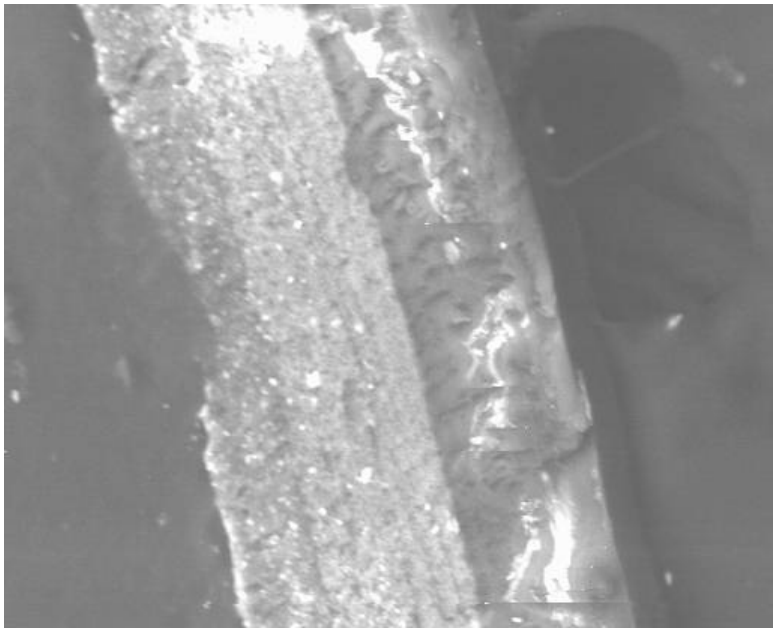

Figure 61: SEM image of the cross-section of 2005 Ford Excursion (3 layers observed)

The EDX spectra collected from this sample are illustrated in Figure 62. There is a significant difference between the clear layer spectrum and the color layer spectrum and the primer layer spectrum. The initial difference observed is the titanium peak at 4.5 keV present in the color and the primer layer but not in the clear coat. There are a few peaks that differentiate the color and the primer, i.e. sulfur (2.4 keV) and tin (3.7 keV). The first two peaks should be disregarded because these peaks represent the intensities of carbon and oxygen.

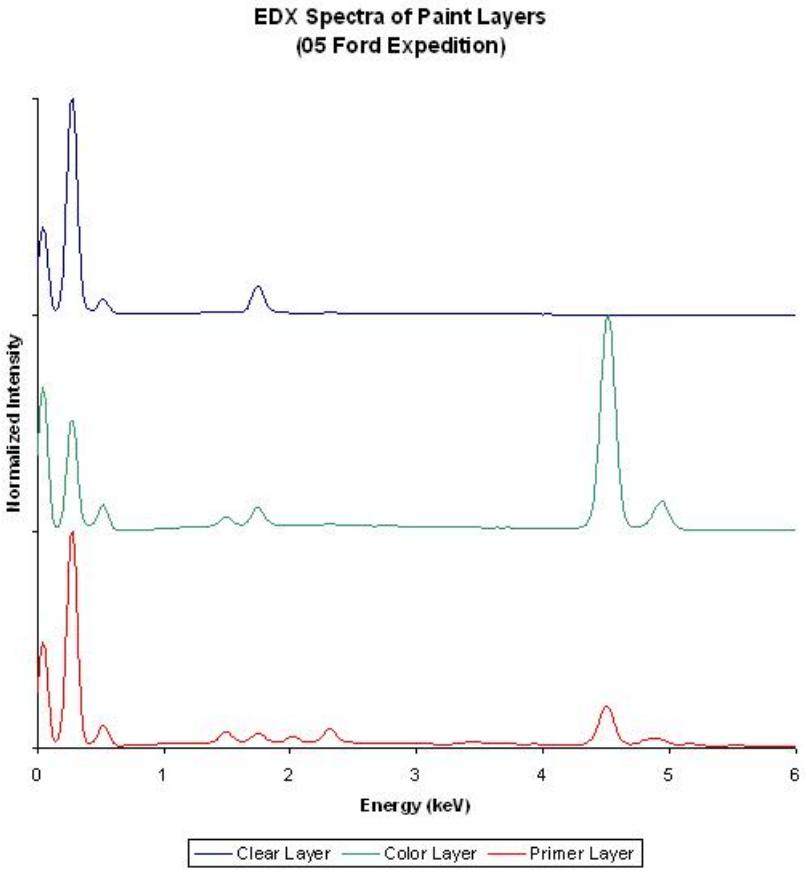

Figure 62: EDX spectra of 2005 Ford Expedition paint layers

From the sample cross section imaged in Figure 63, five layers can be differentiated. The clear coat is shown to be on the left, followed by the color layer, two primer layers and a metallic layer. The metallic layer is residual metal from the metallic substrate of the automobile. The sample was imaged under a backscatter detector to provide to most discriminatory information of the layers.

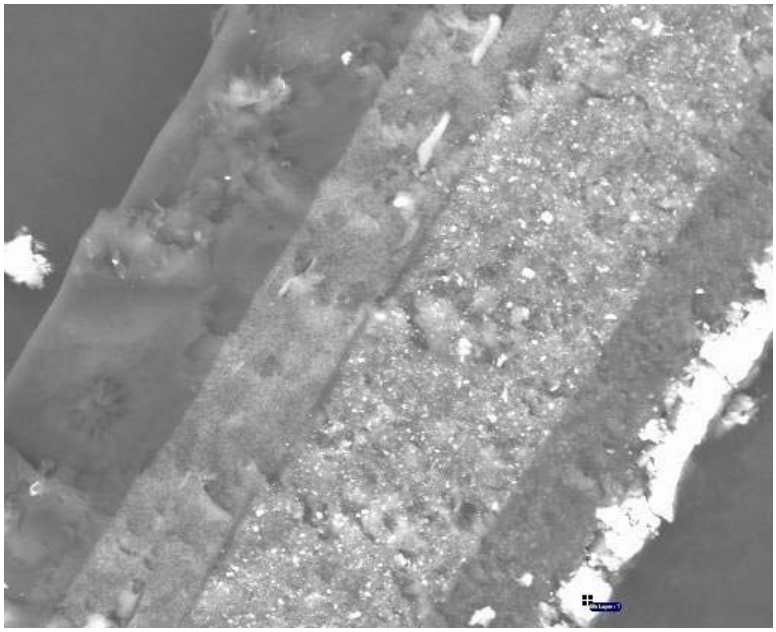

Figure 63: SEM image of the cross-section of 2005 Toyota Sienna (5 layers observed)

Figure 64 illustrates the EDX spectra from the 2005 Toyota Sienna. The clear coat shows for this sample is relatively flat in comparison to the '05 Ford Expedition clear coat in Figure 62 which had a silicon peak around 1.7 keV. The color and the first primer layer are similar except for the iron peak (6.4 keV) present in the primer layer. The first primer layer and the second primer layer are differentiated by the sulfur peak (2.4 keV) and the barium (4.9 keV) both of which are located in the first primer layer.

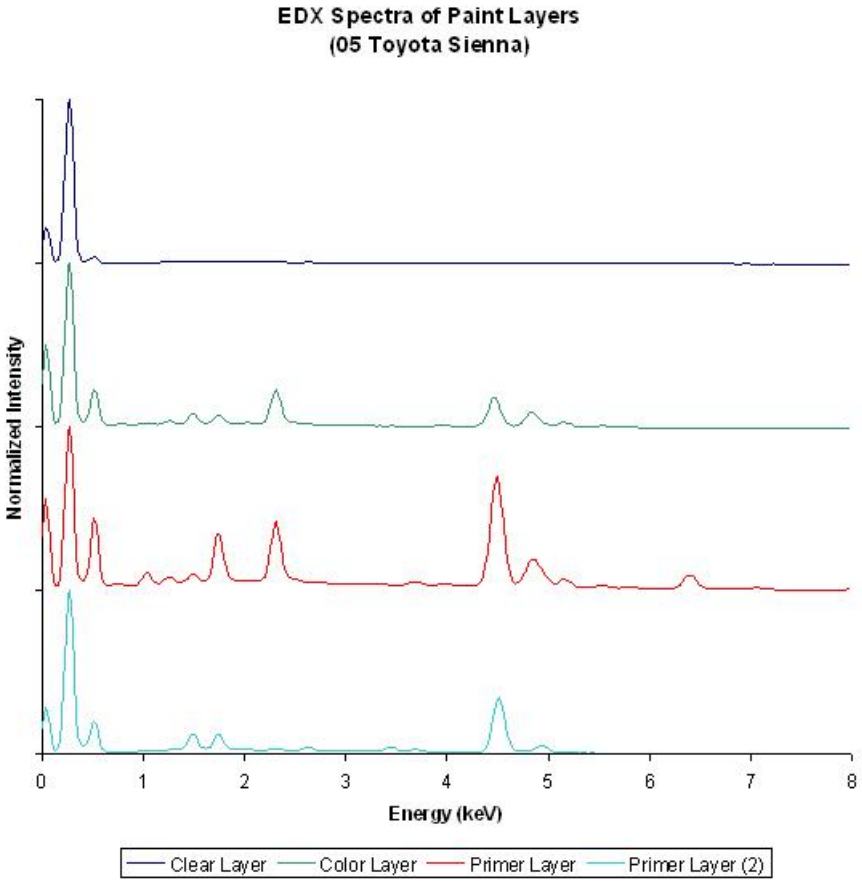

Figure 64: EDX spectra of 2005 Toyota Sienna paint layers

The SEM image shown in Figure 65 shows an example of a repainted automobile sample. The left-most layer is the original primer from the manufacture. The first layer on the right is a repainted clear coat. This sample was imaged under a backscatter detector and a minimum of 10 layers can be observed.

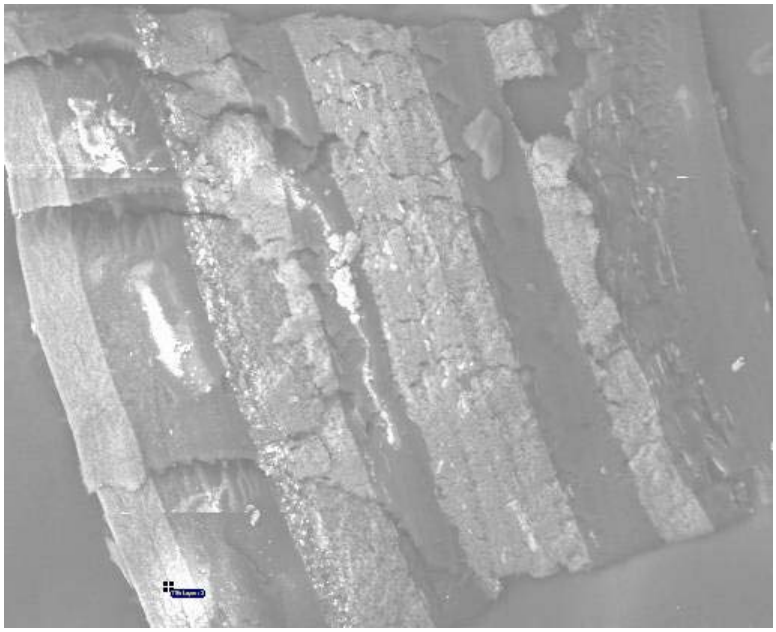

Figure 65: SEM image of the cross-section of 1987 Toyota Truck (10 layers observed)

Results and Discussion

ANOVA/Tukey HSD Data Analysis

One hundred and four samples (104 samples, 5,356 unique pairwise comparisons) were analyzed by SEM-EDX. Three measurements were obtained per layer per sample. The discrimination ratios were analyzed by the ANOVA/Tukey test explained in chapter five. Analysis was performed at a 95% confidence level (Table 29).

Table 29: SEM-EDX discrimination of automobile paint samples by ANOVA/Tukey HSD method

Clear Layer	Color Layer	Primer Layer	Sum of 3 Layers
29.4	39.6	28.7	70.2

Student's t-test/HQI Discrimination

The full spectra (0 to 10 keV) of each layer were discriminated at a confidence level of 95%. The Bonferonni correction was employed for the full spectral comparison. Each layer was analyzed at a 99% confidence level. 25.0% of the samples could be discriminated by the clear layer, the color layer discriminated 47.2% and 67.0% was discriminated based on the comparison of the primer layer. The overall discrimination of the paint samples, utilizing all three layers, was 84.6% (Table 30).

Table 30: Full spectral discrimination of SEM-EDX automobile paint spectra by Student's *t*-test/ HQI method

Clear Layer	Color Layer	Primer Layer	Sum of 3 Layers
25.0	47.2	67.0	85.6

XRF

XRF Experimental Method

To prepare the samples for the XRF measurement, the layers of each sample had to be exposed. Analysis on the edge of a sample was not practical since the width of the sample's edge was much smaller than the beam's diameter of 300 µm. To expose the layers, each layer was removed by hand with a diamond straight knife (Thermo Electron Corp.: Madison, WI). Each layer was scraped off to expose the layer below until the last layer was uncovered. If the bottom layer was too brittle to scrape off the preceding layers, then the back of the sample was measured instead. Each layer was

analyzed in triplicate. In the case of repainted automobile samples, it was difficult to expose every layer since some repainted layers tend to be much too thin to expose without destroying the layer itself. In the case of repainted automobile sample, great care was taken to ensure that only the original layers of paint were used for discrimination (i.e. the layers closest to the automobile substrate) even though every layer of the paint sample was exposed and analyzed. In the case that there was more than one original primer layer, the first primer layer deposited onto the substrate was used for sample discrimination.

Results and Discussion

ANOVA/Tukey HSD Data Analysis

Each layer of the 104 automobile paint samples were analyzed individually, XRF spectra are for each layer analyzed is illustrated in Figure 66. The most intense peak observed in each spectrum was titanium (Ti). Discrimination of the paint samples based on the clear coat alone yielded 52.2% discrimination at a 95% CL. The color layer differentiated 42.9% of the paint samples and 63.6% of the samples could be discriminated by the first primer layer at the 95% CL. Overall, 83.4% of the samples were discriminated based on XRF elemental ratios. There were no type I errors made during this analysis. The discriminating ratios are present in Table 31, along with the percentage of samples discriminated at a 95% CL.

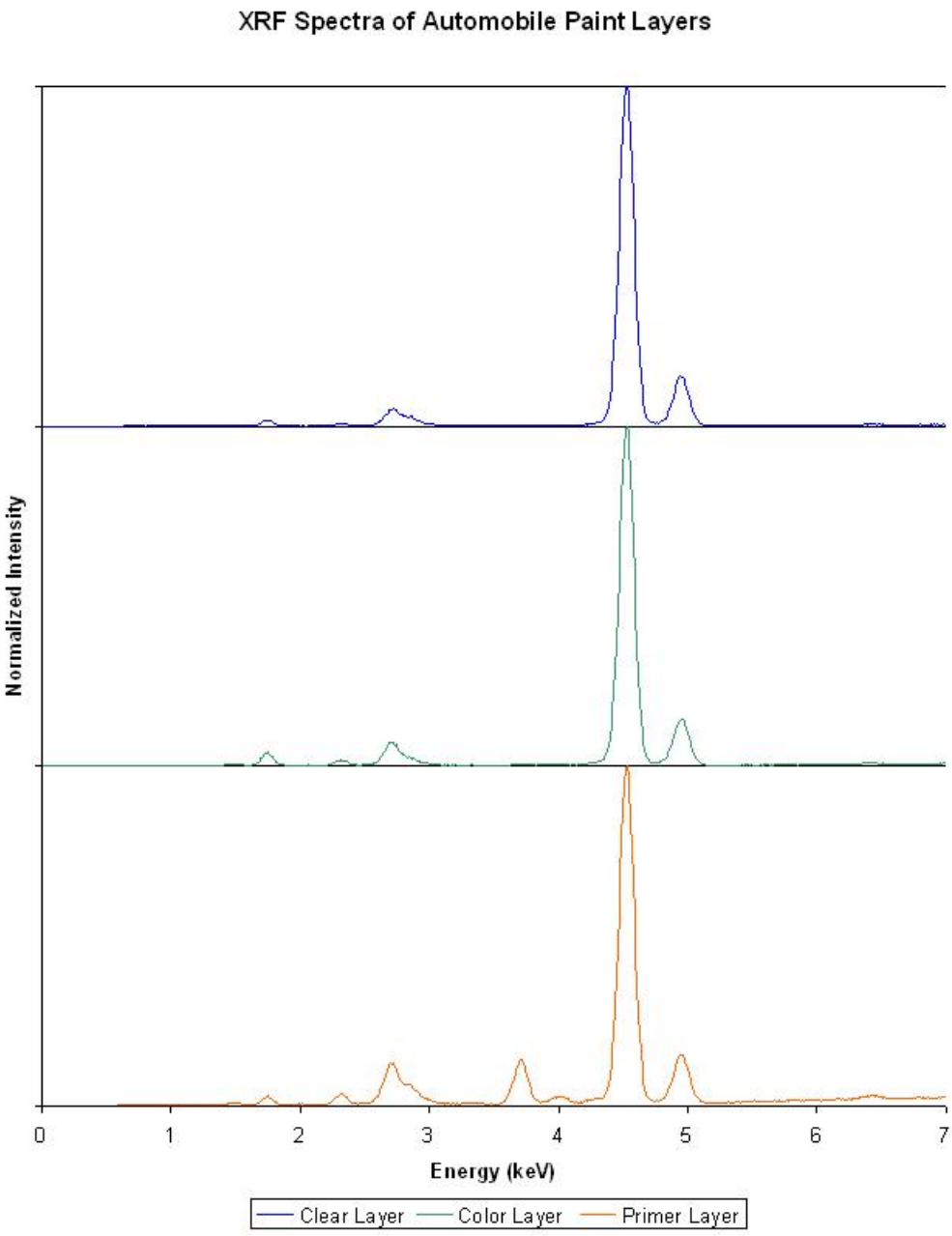

Figure 66: XRF spectra of the clear, color and primer layer of a paint sample

Table 31: SEM-EDX discriminating ratios for automobile paint samples at a 95% CL (only K lines included)

Emission Ratios	Clear Layer		Color Layer		Primer Layer	
	F-Statistic	% Discrim	F-Statistic	% Discrim	F-Statistic	% Discrim
Mg/Al	2.0	1.9	10.4	10.8		
Na/Mg					1.4	1.9
Si/Mo	4.0	5.1	2.7	3.7	3.0	2.6
S/P	10.8	9.5	2.2	1.7	3.8	5.6
Cl/K	6.2	6.2	2.6	6.2	2.2	1.3
Ti/Fe	11.6	11.7	19.7	31.7	16.12	28.0
Cr/Mn	8.4	5.7	44.4	10.6		
Ni/Co	3.4	3.5	2.4	5.4	3.0	3.6
Cu/Zn	2.1	3.3	10.3	6.9	62.1	9.3
Rb/Zn	6.4	9.8			8.1	8.7
Ti/Al	5.25	8.0	13.0	10.8	5.62	6.8
Ca/V			6.8	5.6		
Total Discrimination		52.2		42.9		63.6

Student's t-test/HQI Discrimination

In the full spectral comparison, the Student's *t*-test method described in chapter five, was used for calculating the discrimination percentage based on each paint layer. The Bonferonni correction was used in order to minimize the type I error for the overall discrimination since each paint layer is considered to be a separate parameter. Therefore, the individual matrices for each paint layer had to be analyzed at a confidence level of 99% to obtain an overall confidence level α = 97%. At 99% CL, 87.4% could be discriminated based on the clear layer, 99.4% was discriminated by the color layer and the primer layer discriminated 80.6% of the 5,356 pair-wise comparisons (Table 32). Therefore, based on all three layers at the overall confidence level of 97%, 100% of the samples could be discriminated. Although 100% discrimination was obtained from this sample set, a type I error was made. One sample that was analyzed two separate times was determined to be of different sources, which constitutes a type I error.

Table 32: XRF discrimination of automobile paint samples (confidence levels)

Clear Layer (99%)	Color Layer (99%)	Primer Layer (99%)	Overall Discrimination (97%)
87.4	99.4	80.6	100

Jackknife Analysis

As described above, a type I error was made during the full spectral analysis. The objective of using the jackknife analysis was to investigate the probability of making a type I error when using the full XRF spectrum for analysis. Jackknifing is a statistical method used to estimate the standard error of a random set of observations.[119] This method is based on recalculating the comparison after omitting one observation at a time.

Ten samples from different sources were chosen at random from the complete sample set. Only the spectra from the color layer were used for this comparison. Three spectra were obtained for each sample and one spectrum was omitted at a time. The following spectra sets, which contain two of the three spectra, were analyzed using the Student's *t-test* method described in chapter four. The spectra were analyzed from 1 to 15 keV at a 95% confidence level.

Based on this comparative method, no type I errors were committed. The replicate spectra could not be discriminated from one another when one spectrum was omitted. This was true for all of ten samples compared. Of the comparisons made between samples, 82.2% of the pair-wise comparisons could be discriminated; therefore, 17.8% were type II errors made during this analysis.

LA-ICP-MS

LA-ICP-MS Experimental Method

The method used to sample the automobile paints is similar to the drill down method described for automobile glass samples in chapter six. Instead of just examining the clear coat, as was done in the previous analysis, all layers were incorporated into this analysis. Each sample was analyzed at eight positions. To prevent carryover of each position's analysis the first position was discarded. The sampling at each position was comprised of seven acquisitions, in order to follow elemental trends through the sample. The method described above was developed from previous literature where LA-ICP-MS was used in a drill down method through the paint layers.[88, 89] A time-resolved analytical method was selected for this procedure to identify paint layers based on elemental trends through the sample. The time-resolved analytical method provides the instrumental responses to the elemental concentration in the sample without any further data processing. Therefore, the elemental responses can be followed in time and can identify "pockets" of excess elements through the analysis. Samples that were repainted, the analysis time had to be adjusted to account for the additional layers. The instrumental parameters for this analysis are present in Table 33.

Table 33: Instrumental parameters for LA-ICP-MS drill-down method – automobile paint analysis

Parameter	Value
Laser Output Energy	6 mJ/pulse
Laser Output Wavelength	213 nm
Sampling Energy	0.13 mJ (75%)
Raster Spacing	250 μm
Spot Size	50 μm
Ablation Depth	1 μm
Frequency	10 Hz
RF Power	1500 W
RF Matching	1.84 V
Carrier Gas	0.73 L/min
Ablation Cell Vol.	22 mL
Ablation Mode	Spot Drill Down
Sampling Time	10 minutes
Pre-ablation	No
Integration Time	0.1 sec/isotope
Dwell Time	61 sec

Three elements (Li, Y, and Tl) were used to check background counts of the instrument and to check the system parameters for maximum intensity. These elements were chosen to optimize the system for light, medium and heavy weighed samples. NIST standard SRM 612 was used to optimize the parameters of the system. Fifteen samples were analyzed by this method and all samples were analyzed in one day which reduces any system drifts.

Results and Discussion

The method of analysis chosen for this sample set was the ANOVA/Tukey HSD data analysis. Seven acquisitions were collected per position to collect isotopic intensities

down through the sample. The first five acquisitions per position were used in the comparison of the paint samples. Paint layers could not be identified based on the repetitions alone. Hence, the intensities from each repetition were summed for each acquisition. It was the summed values that were used to create discriminating ratios per acquisition. Isotopes exhibiting a large response (> 100,000 counts) were ratioed to other isotopes with a large response, while isotopes with a smaller response (< 100,000 counts) were ratioed to other ratios with a smaller response. The ratios used for analysis were chosen based on their F-statistic values and their Pearson correlation values.

High discrimination, greater that 95%, is achieved for each acquisition and overall at each confidence level (Table 35). This is due to the high precision of this instrument which yielded high F-statistic values for each discriminating ratio. The F-statistic ranged from 2 – 2,256, refer to Table 34.

Table 34: LA-ICP-MS isotopic discrimination of automobile paint by ANOVA/Tukey HSD data analysis at the 90% CL

Isotopic Ratio	Acquisition 1		Acquisition 2		Acquisition 3		Acquisition 4		Acquisition 5		Total Discrimination	
	F-value	90% CL	F-value	90% CL	F-value	90% CL	F-value	90% CL	F-value	90% CL	F-value	90% CL
^{23}Na / ^{24}Mg	29.4	43.1	1.8	7.8	106.5	58.8	547.9	73.9	738.8	76.5	48.7	54.2
^{27}Al / ^{29}Si	88.0	32.0	47.6	47.7	135.4	34.6	184.5	49.7	98.5	45.1	157.1	62.7
^{208}Pb / ^{137}Ba	66.3	21.6	25.3	11.1					127.8	11.1	369.5	11.1
^{51}V / ^{53}Cr	121.1	11.1	342.7	11.1			379.6	11.1			2,255.7	11.1
^{90}Zr / ^{79}Br	16.8	23.5	124.6	45.8	58.6	11.1	270.7	49.7	205.3	50.3	146.6	27.5
^{34}S / ^{60}Ni	22.4	11.1	6.3	11.1	13.4	38.6	40.8	58.2	66.9	58.8	114.7	56.9
^{44}Ca / ^{35}Cl	13.1	34.0	17.2	42.5	180.4	74.5	394.3	36.6	426.0	53.6	430.2	61.4
^{47}Ti / ^{118}Sn	35.7	59.5										
^{56}Fe / ^{55}Mn	24.1	43.8	6.0	17.6	33.2	37.9	59.0	68.0	139.1	71.2	25.22	45.8
^{31}P / ^{34}S	68.9	47.7			1,547.8	38.6	223.9	30.1	172.9	45.8		
^{133}Cs / ^{59}Co			40.8	21.6	242.1	21.6	223.82	11.1				
^{90}Zr / ^{79}Br											146.7	27.5
Overall Discrimination		98.4		97.4		96.1		100.0		100.0		100.0

Table 35: LA-ICP-MS discrimination of automobile paint samples

	90% CL	95% CL	99% CL
Acquisition 1	98.0	98.0	98.0
Acquisition 2	97.4	97.4	97.4
Acquisition 3	96.1	96.1	95.4
Acquisition 4	100.0	100.0	100.0
Acquisition 5	100.0	100.0	100.0
Overall Discrimination	100.0	100.0	100.0

The time resolved analytical method was employed to allow identification of the layers of the paint sample by following the intensities of specified elements through the sample. This type of layer identification has previously reported with optimal results.[88] While this methodology worked for a few elements in a single paint sample, this method did not allow for layer identification.

Conclusion

FTIR-ATR spectral comparison has been the primary analytical method used in identifying the source of an automobile paint samples. Microscopic examination is another higher utilized technique which can identify the number of paint layers and even the thickness of each layer.[115] While these techniques are informative there are LIBS could provide elemental information about each paint layer in the sample that

could supplement information obtained from the FTIR. Of the techniques used to analyze the clear coat of the paint samples, XRF analysis provided the most discrimination (Table 36). Of the emission spectra examined in this study (i.e. XRF, EDX and LIBS) data analysis by full spectra HQI analysis provided the best discrimination. Analysis by LIBS provided similar discrimination as XRF analysis.

Correlation between the LIBS spectra and IR classification was poor. This may be due to the differences in the type of information that each technique provides. However, based on relationship of the molecular structure to the molecular emissions observed in the LIBS spectra that was observed in the previous chapter, classification of the automobile paint clear coats may be possible by LIBS analysis. Identifying a direct correlation of the LIBS spectra to the molecular structure of each type of clear coat is necessary.

Table 36: Overall discrimination of paint samples by various instrumental techniques

	FTIR-ATR	LIBS	SEM-EDX		XRF		LA-ICP-MS
Method	Full Spectral	Full Spectral	ANOVA/Tukey	Full Spectral	ANOVA/Tukey	Full Spectral	ANOVA/Tukey
CL	95%	95%	95%	97%	95%	97%	95%
Clear Layer	68.8	73.5	29.4	25.0	55.2	87.4	
Color Layer			39.6	47.2	42.9	99.4	
Primer Layer			28.7	67.0	63.6	80.6	
Overall Discrimination			70.2	85.6	83.4	100.0*	100.0

* A type I error made

CHAPTER TEN:
CONCLUSION

The purpose of this study was to evaluate LIBS as an alternative elemental emission instrument of current instruments that allows for rapid analysis and is within the limited budget faced by many forensic laboratories. While LIBS is desirable in terms of its cost, sample preparation time and analysis time, its major drawback is that the LIBS is not as precise as other instruments currently used. The poor precision of LIBS is due to inconsistent and techniques plasmas generated for each analysis. Day-to-day plasma inconsistencies have been shown to be a limitation for spectral analysis by LIBS; however, LIBS is not ruled out as a reliable instrument that can provide discriminatory information for back-to-back sample comparisons. LIBS has demonstrated that it can provide discrimination results that are comparable to currently used instrumentations in forensic laboratories, i.e. LA-ICP-MS and SEM-EDX. However, if a type II error occurs then other instrumentation is necessary for further discrimination. This was observed by incorporating RI data for glass discrimination and was also observed in paint analysis by utilizing all layers observed in the sample.

Automobile Glass Analysis

Various statistical techniques were investigated for spectral analysis of LIBS. Of these statistical techniques examined, ANOVA followed by the Tukey HSD post-test provided

the highest discrimination for the analysis of trace glass samples. Using this analysis for refractive index in conjunction with the LIBS elemental ratios provided comparable results to those achieved by the LA-ICP-MS discrimination of the same sample set. However, discriminating using ANOVA/Tukey can be tedious in terms of identifying and creating ratios that have a high F-statistic and are not highly correlated with the other discriminating ratios.

As an alternative, methods of full spectral analysis were examined. These types of data analyses were more conducive to rapid analysis than the ANOVA/Tukey HSD analytical method. Full spectral analysis (baseline included) provided less discrimination than using the isolated peaks method. Analyzing isolated peaks with a S:N greater than 3 that are present in both the known and unknown spectra, data analysis methods (i.e. Sorenson, Rank and Pearson) provides discriminating powers that are comparable to the ANOVA/Tukey HSD data analysis method. Of the analysis methods explored for the comparison of isolated peaks, the Student's *t*-test/rank correlation method provided the highest discrimination percentage of automobile float glass (float side) samples.

Principal component analysis allowed classes of glasses (i.e. borosilicate vs. soda-lime silicate) to grouped accordingly with other samples of that class. The float glasses were grouped together based on using full spectra; however, discriminating ratios were able to provide further separation of the different types (i.e. automobile float vs. automobile side mirror). This type of analysis can be a screening process of sample class and

further individual discrimination can then be obtained by using other discrimination techniques and/or instrumentation.

Organic Material Analysis

Energetic and organic materials were analyzed in a crystalline form and as a residue. Residue samples were used to determine if it was possible to accurately detect these materials via atomic and diatomic bands in the resulting LIBS spectra. Calibration curves were attempted, but due to the nature of some of the analytes, detection of these materials was not achieved at surface concentrations below 50 $\mu g/cm^2$. Classification of solid explosive materials was attempted through principal component analysis of LIBS spectra collected under an argon atmosphere. Groupings based on the atomic structure of the explosives were observed but there was some overlap of these groups. Classifying explosive based on the intensity of atomic carbon, swan bands, violet bands, atomic nitrogen and atomic oxygen in the presence of an argon atmosphere may be possible. However, more accurate groupings of the organic materials was observed under an inert atmosphere (argon), which was achieved by incorporating the oxygen bands into the overall analysis. Based on the this study it may be possible to identify a correlation between the LIBS spectra to the molecular structure of an organic material.

Automobile Paint Analysis

Currently, the top clear coat layer of automobile paint samples provides little discriminatory information. Techniques used in forensic laboratories classify the type of clear coat layer based on the Ryland IR classification flowchart.[116] It has been demonstrated in this research that more information may be available through other analytical methods (i.e. SEM-EDX, LIBS and XRF). Of these techniques used for analysis, XRF provided the greatest discrimination. LIBS provided a high discrimination of the samples based on full spectral analysis using the Student's *t*-test/HQI method; however, nearly 20% of the comparisons made were a type II error which should be avoided in forensic science. The grouping observed from the principal component analysis of the LIBS spectra does not seem to match the classifications offered by the Ryland IR flowchart. SEM offered images of the paint cross sections which provided information regarding the number of different layers; however, the discriminating power of EDX was not has high as the other discriminating techniques explored. It is possible that this low discrimination is due to the analytical procedure chosen. Other techniques should be investigated to determine if there is an increase in the overall discrimination of these paint samples. LIBS seems to provide comparable results to other techniques in regards to the clear coat analysis.

LIBS has potential of being a useful technique for elemental analysis for trace evidence commonly encountered in forensic laboratories. The interpretation and data processing

of required for LIBS spectra can be a potential concern. In this study, many instrumental techniques and various types of data analysis were examined to determine how comparable LIBS can be to other accepted instrumental methods currently used for discrimination.

Future Work

Organic Materials Analysis

Two-dimensional correlation spectroscopy was used to identify relationships between the atomic carbon peak, the swan band set and the violet band set. Due to the limitations of this LIBS spectrometer, the relationship between the growths of these species was not possible. With a higher resolution spectrometer and a shorter spectrometer gate time, it may be possible to accurately identify the relationships that form these diatomic species with reference to the carbon atomic emission under an argon atmosphere. This may also lead to information about how the CN bands are formed when the nitrogen comes from the sample in comparison to atmospheric nitrogen. While it was demonstrated that classifications of organic materials can be achieved based on LIBS spectra; a method for accurate identification of organic materials for long range analysis using an inert atmosphere should be examined.

Automobile Paint Analysis

Additional work needs to be done to identify an accurate relationship between the Ryland IR classification of automobile paint clear coats and the results obtained from other analytical methods. The results presented in this study do not provide a clear relationship between the grouping of clear coat LIBS spectra and the Ryland groupings of the same samples. If known samples of the clear coat can be obtained, then accurate determination of these layers would provide a clear relationship between the IR classification and LIBS spectra.

Layer identification of paint samples should also be explored more thoroughly, especially in the case of repainted samples which would offer elemental information in addition to microscopic analyses. Further examination of the color and the primer coat of automobile paint samples by LIBS is necessary for a complete comparison of this technique in comparison to other more established instrumental methods.

REFERENCES

1. Xu, L., Bulatov, V., Gridin, V. V.,Schechter, I., Absolute Analysis of Particulate Materials by Laser-Induced Breakdown Spectroscopy. *Anal. Chem.* **1997,** 69, 2103-2108.
2. Menut, D., Fichet, P., Lacour, J-L., Rivoallen, A., Mauchien, P., Micro-laser-induced breakdown spectroscopy technique: a powerful technique for performing quantitative surface mapping on conductive and nonconductive samples. *Applied Optics* **2003,** 42, (30), 6063-6071.
3. Borgia, I., Burgio,L. M. F., Corsi, M., Fantoni, R., Palleschi, V., Salvetti, A., Squarcialup, M. C., Tognoni, E., Self-calibrated quantitative elemental analysis by laser-induced plasma spectrscopy: application to pigment analysis. *J. Cult. Heritage* **2000,** 1, S281-S286.
4. Chaléard, C., Mauchien, P., Andre, N., Uebbing, J., Lacour, J. L., Geertsen, C., Correction of Matrix Effects in Quantitative Elemental Analysis with Laser Ablation Optical Emission Spectrometry. *J. Anal. At. Spectrom.* **1997,** 12, 183-188.
5. Mohamed, W. T. Y., Improved LIBS limit of detection of Be, Mg, Si, Mn, Fe, and Cu in aluminum allow samples using a portable Echelle spectrometer with ICCD camera. *Optics & Laser Technology* **2008,** 40, 30-38.
6. Hohreiter, V., Hahn, D. W., Calibration Effects for Laser-Induced Breakdown Spectroscopy of Gaseous Sample Streams: Analyte Response of Gas-Phase Species versus Solid-Phase Species. *Analytical Chemistry* **2005,** 77, 1118-1124.
7. Sneddon, J., Lee, Y., Laser-Induced Breakdown Spectrometry. In *The Chemical Educator [Electronic Publication]* [Online] 6 ed.; Schimph, M., Ed. Springer-Verlag: New York, 1998.
8. Lee, Y., Sneddon, J., Recent Developments in Laser Induced Breakdown Spectrometry. *ISIJ International* **2002,** 42, S129-S136.
9. Lee, W., Wu, J., Lee, Y., Sneddon, J., Recent Applications of Laser-Induced Breakdown Spectrometry: A Review of Material Approaches. *Applied Spectroscopy Reviews* **2004,** 39, 27-97.

10. Hahn, D. W., Miziolek, A. W., Palleschi, V., Laser-induced breakdown spectroscopy: an introduction to the feature issue. *Applied Optics* **2004,** 42, 5937.

11. Rusak, D. A., Castle, B. C., Smith, B. W., Winefordner, J.D., Recent trends and the future of laser-induced breakdown spectroscopy. *Trends in Analytical Chemistry* **1998,** 17, 453-461.

12. Samuels, A. C., DeLucia, F. C., McNesby, K. L., Miziolek, A. W., Laser-induced breakdown spectroscopy of bacterial spores, molds, pollens, and protein: initial studies of discrimination potential. *Applied Optics* **2003,** 42, 6025-6029.

13. Sun, Q., Tran, M., Smith, B. W., Winefordner, J. D., Zinc analysis in human skin by laser induced-breakdown spectroscopy. *Talanta* **2000,** 52, 293-300.

14. Corsi, M., Cristoforetti, G., Hidalgo, M., Legnaioli, S., Palleschi, V., Salvetti, A., Tognoni, E., Vallebona, C., Application of laser-induced breakdown spectroscopy technique to hair tissue mineral analysis. *Applied Optics* **2003,** 42, (30), 6133-6137.

15. Kumar, A., Yueh, F-Y., Singh, J. P., Burgess, S., Charaterization of malignant tissue cells by laser-induced breakdown spectroscopy. *Applied Optics* **2004,** 43, 5399-5403.

16. Kuzuya, M., Murakami, M., Maruyama, N., Quantitative Analysis of ceramics by laser-induced breakdown spectroscopy. *Spectrochimica Acta Part B: Atomic Spectroscopy* **2003,** 58B, 957-965.

17. Cremers, D. A., Radziemski L. J., History and fundamentals of LIBS. In *Laser-Induced Breakdown Spectroscopy (LIBS): Fundamentals and Applications*, Miziolek, A., Palleschi, V., Schechter, I., Ed. Cambridge University Press: New York, 2006; pp 1-39.

18. DeLucia Jr., F. C., Harmon, R. S., McNesby, K. L., Winkel Jr., R. J., Miziolek, A. W., Laser-induced breakdown spectroscopy analysis of energetic materials. *Applied Optics* **2003,** 42, 6148-6152.

19. Ciucci, A., Corsi, M., Palleschi, V., Rastelli, S., Tognoni, E., New Procedure for Quantitative Elemental Analysis by Laser-Induced Plasma Spectroscopy. *Applied Spectroscopy* **1999,** 53, 960-964.

20. Russo, R. E., Mao, X. M., Liu, H. Gonzalez, J., Mao, S. S., Laser ablation in analytical chemistry - a review. *Talanta* **2002,** 57, 425-451.

21. Corsi, M., Cristoforetti, G., Hidalgo, M., Iriarte, D., Legnaioli, S., Palleschi, V., Salvetti, A., Tognoni, E., Effect of Laser-Induced Crater Depth in Laser-Induced Breakdown Spectroscopy Emission Features. *Applied Spectroscopy* **2005,** 59, (7), 853-860.

22. Mao, S. S., Zeng, X., Mao, X., Russo, R. E., Laser-induced breakdown spectroscopy: flat surface vs. cavity structures. *J. Anal. At. Spectrom.* **2004,** 19, 495-498.

23. Fu Su, C., Feng, S., Singh, J. P., Yueh, F., Rigsby III, J. T., Monts, D. L., Cook, R. L., Glass composition measurement using laser induced breakdown spectroscopy. *Glass Technology* **2000,** 41, 16-21.

24. Ismail, M. A., Imam, H., Elhassan, A., Youniss, W. T., Harith, M. A., LIBS limit of detection and plasma parameters of some elements in two different metallic matrices. *J. Anal. At. Spectrom.* **2004,** 19, 489-494.

25. Koons, R. D., Buscaglia, J., Interpretation of Glass Composition Measurements: The Effects of Match Criteria on Discrimination Capability. *J. Forensic Sci.* **2002,** 47, 505-511.

26. Sachs, L., *Applied Statistics: A Handbook of Techniques,*. 2nd ed.; Springer-Verlag: New York, 1984.

27. Miller, J. N., Miller, J. C., *Statistics and Chemometrics for Analytical Chemistry*. 4th ed.; Pearson Prentice Hall: New York, 2000.

28. Duckworth, D. C., Morton, S. J., Bayne, C. K., Koons, R. D., Montero, S., Almirall, J. R., Forensic glass analysis by ICP-MS: a multi-element assessment of discriminating power *via* analysis of variance and pairwise comparisons. *J. Anal. At. Spectrom.* **2002,** 17, 662-669.

29. Sigman, M. E., Williams, M. R., Ivy, R. G., Individualization of Gasoline Samples by Covariance Mapping and Gas Chromatography/Mass Spectrometry. *Analytical Chemistry* **2007,** 79, (9), 3463-3468.

30. O'Rourke, N. R., Hatcher, L., Stepanski, E., Principle Component Analysis. In *A Step-by-Step Approach to Using SAS® for Univariante and Multivariate Statistics, 2nd ed.*, SAS Institute Inc.: 2005.

31. Coombes, K. R., Fritsche Jr., H. A., Clarke, C., Chen, J-N., Baggerly, K. A., Morris, J. S., Xiao, L-C., Hung, M-C., Kuerer, Quality Control and Peak Finding for Proteomics Data Collected from Nipple Aspirate Fluid by Surface-Enhanced Laser Desorption and Ionization. *Clinical Chemistry* **2003,** 49, 1615-1623.

32. Gribskov, M., Robinson, N. L., *Computers Chem.* **1996,** 20, (1), 25-33.

33. Griem, H. R., Validity of Local Thermal Equilibrium in Plasma Spectroscopy. *Phys. Review* **1963,** 131, (3), 1170-1176.

34. Griem, H. R., *Plasma Spectroscopy*. McGraw-Hill Book Company: New York, 1964.

35. Simeonsson, J. B., Miziolek, A. W., Time-resolved emission studies of ArF-laser-produced microplasmas. *Applied Optics* **1993,** 32, (6), 939-937.

36. Sabsabi, M., Cielo, P., Quantitative Analysis of Aluminum Alloys by Laser-Induced Breakdown Spectroscopy and Plasma Characterization. *Applied Spectroscopy* **1995,** 49, (4), 499-507.

37. Atkins, P., de Paula, J, *Physical Chemistry*. 7th ed.; W. H. Freeman and Company: New York, 2002.

38. Pine, A. S., Looney, J. P., Self-broadening and line mixing in HCN *Q* branches. *J. Chem. Phys.* **1992,** 96, (3), 1704-1714.

39. Busquet, M., Klapisch, M., Bar-Shalom, A., Absorption and emission profiles of unresolved arrays near local thermodynamic equilibrium. *Quant. Spectrosc. Radia. Transfer* **2003,** 81, 255-263.

40. Schechter, I., Bulatov, V, Plasma Morphology. In *Laser-Induced Breakdown Spectroscopy (LIBS): Fundamentals and Applications*, Miziolek, A., Palleschi, V., Schechter, I., Ed. Cambridge University Press: New York, 2006; pp 40-121.

41. Ramendik, G. I., Fatyushina, E. V., Stepanov, A. I., Sevast'yanov, V. S., New Approach to the Calculation of Relative Sensitivity Factors in Inductively Coupled Plasma Mass Spectrometry. *Journal of Analytical Chemistry* **2001,** 56, 500-506.

42. Riascos, H., Zambrano, G., Prieto, P., Spectroscopic Analysis of a Pulsed-laser Deposition System for Fullerene-like Cn_x Film Production. *Plasma Chem Plasma Process* **2006,** 26, 277-291.

43. van der Mullen, J. A. M., Benoy, D. A., Fey, F. H. A. G., van der Sijde, B., Vlcek, J, Saha equation for two-temperature plasmas: Theories, experimental evidence, and interpretation. *Phys. Rev. E* **1994,** 50, (5), 3925-3934.

44. Rego, G. M., Marques P. V. S., Santos, J. L., Salgado, H. M., Estimation of the fibre temperature during the inscription of arc-induced long-period gratings. *Optics Communications* **2006,** 259, 620-625.

45. Caughlin, B. L., Blades, M. W., An evaluation of ion-atom emission intensity ratios and local thermodynamic equilibrium in an argon inductively couple plasma. *Spectrochimica Acta Part B: Atomic Spectroscopy* **1984,** 398, (12), 1583-1602.

46. Burton, L. L., Blades, M. W., A simple method for calculating deviations from local thermodynamic equilibrium in the inductively coupled plasma. *Spectrochimica Acta Part B: Atomic Spectroscopy* **1990,** 45B, 139-144.

47. Eland, K. L., Stratis, D. N., Lai, T., Berg, M. A., Goode, S. R., Angel, S. M., Some Comparisons of LIBS Measurements Using Nanosecond and Picosecond Laser Pulses. *Applied Spectroscopy* **2001,** 55, (3), 279-285.

48. Rohwetter, P., Yu, J., Méjean, G., Stelmaszczyk, K., Salmon, E., Kasparian, J.-P., Wöste, L., Remote LIBS with ultrashort pulses: characteristics in picosecond and femtosecond regimes. *J. Anal. At. Spectrom.* **2004,** 19, 437-444.

49. Taschuk, M. T., Kirkwood, S. E., Tsui, Y. Y., Fedosejevs, R., Quantitative emission from femtosecond microplasmas for laser-induced breakdown spectroscopy. *Journal of Physics: Conference Series* **2007,** 59, 328-332.

50. Gornushkin, I. B., Omenetto, N., Smith, B. W., Winefordner, J. D., Determination of the Maximum Temperature at the Center of an Optically Thick Laser-Induced Plasma Using Self-Reversed Spectral Lines. *Applied Spectroscopy* **2004,** 58, (9), 1023-1031.

51. Russo, R. E., Wen, S., Mao, W. In *Experimental and Theoretical Studies of Energy and Mass in Laser Ablation Plumes*, FACSS, Lake Buena Vista, FL., 2006; Lake Buena Vista, FL., 2006.

52. Omenetto, O., Morre, G., Gornushkin, I., Smith, B., Winefordner, J. In *Diagnostic Measurements in Laser Induced Plasmas: a Critical Look*, FACSS, Lake Buena Vista, FL., 2006; Lake Buena Vista, FL., 2006.

53. Measures, R. M., Drewell, N., Kwong, H. S., Atomic lifetime measurements obtained by the use of laser ablation and selective excitation spectroscopy. *Phys. Rev. A* **1977,** 16, (3), 1093-1097.

54. Sirven, J.-B. Détection de Métaux Lourds dans les Sols par Spectroscopie d'émission sur Plasma Induit par laser (LIBS) [Detection of Heavy Metals in Soil by Laser Induced Breakdown Spectroscopy]. Université Bordeaux 1: Les Sciences et les Technologies au service de l'Homme et de l'environnement, Bordeaux, France, 2006.

55. Panne, U., Hahn, D., Analysis of aerosols by LIBS. In *Laser-Induced Breakdown Spectroscopy (LIBS): Fundamentals and Applications*, Miziolek, A., Palleschi, V., Schechter, I., Ed. Cambridge University Press: New York, 2006; pp 194-253.

56. Harilal, S. S., Issac, R. C., Bindhu, C. V., Gopinath, P., Nampoori, V. P. N., Vallabhan, C. P. G., Time resolved study of CN band emission from plasma generated by laser irradiation of graphite. *Spectrochimica Acta Part B: Atomic Spectroscopy* **1997,** 53A, 1527-1536.

57. Namba, S., Nozu, R., Takiyama, K., Oda, T., Spectroscopic Study of ablation and recombination processes in laser-produced ZnO plasma. *Journal of Applied Physics* **2006,** 99, 073302/1-073302/9.

58. Krall, N. A., Trivelpiece, A. W., *Principles of Plasma Physics*. McGraw-Hill Book Company: New York, 1973.

59. Bye, C. A., Scheeline, A., Saha-Boltzman statistics for determination of electron temperature and density in spark discharges using an echelle/CCD system. *Applied Spectroscopy* **1993,** 47, (12), 2022-2030.

60. Sung, Y.-i., Lim, H. B., Plasma temperature measurement of a low-pressure inductively coupled plasma using spectroscopic methods. *J. Anal. At. Spectrom.* **2003,** 18, 897-901.

61. Goddard, B. J., Materials analysis using laser-based spectroscopic techniques. *Trans. Inst. MC* **1991,** 13, (3), 128-139.

62. Walker, Z., Blades, M. W., Measurement of excited state level populations for atomic and ionic iron in the inductively coupled plasma. *Spectrochimica Acta Part B: Atomic Spectroscopy* **1986,** 41B, 761-775.

63. Batal, A., Jarosz, J., Mermet, J. M., A spectrometric study of a 40 MHz inductively coupled plasma-VII. Continuum of a binary mixture in the visible region of the spectrum. *Spectrochimica Acta Part B: Atomic Spectroscopy* **1982,** 37B, 511-516.

64. Nick, K.-P., Richter, J., Helbig, V., Non-LTE Diagnostic of an Argon Arc Plasma. *Quant. Spectrosc. Radia. Transfer* **1984,** 32, (1), 1-8.

65. Radziemski, L. J., Loree, T. R., Cremers, D. A., Hoffman, N. M., Time-Resolved Laser-Induced Breakdown Spectroscopy of Aerosols. *Analytical Chemistry* **1983,** 55, 1246-1252.

66. Chen, F. F., *Plasma Physics*. Plenum Press: New York, 1984; Vol. 1.

67. Zellner, M., *Comparison of Stark Broadening and Doppler Broadening of Spectral Lines in Dense Hot Plasmas*. Millersville University.

68. Feng, S. Quantitative Elemental Analysis of Vitrified Glass by Laser-Induced Breakdown Spectroscopy and Plasma Characterization. Mississippi State, MS, 1995.

69. Griem, H. R., *Spectral Line Broadening by Plasmas*. Pure and Applied Physics Academic Press: New York, 1974; Vol. 39.

70. Karabourniotis, D., Karras, C., Drakakis, M., Damelincourt, J. J., Plasma temperature determination from the total intensity of a self-reversed spectral line. *J. Appl. Phys.* **1982,** 52, (11), 7259-7264.

71. Cowan, R. D., Dieke, G. H., Self-Absorption of Spectrum Lines. *Reviews of Modern Physics* **1948,** 20, (2), 418-419.

72. Keszler, A. M., Nemes, L., Time averaged emission spectra of Nd:YAG laser induced carbon plasma. *Journal of Molecular Structure* **2004,** 695-696, 211-218.

73. Harrison, G. R., *M.I.T. Wavelength Tables*. 5th ed.; The M.I.T. Press: Cambridge, MA, 1991.

74. López-Moreno, C., Palance, S., Laserna, J. J., Calibration transfer method for the quantitative analysis of high-temperature materials with stand-off laser-induced breakdown spectroscopy. *J. Anal. At. Spectrom.* **2005,** 20, 1275-1279.

75. Bridge, C. M., Powell, J., Steele, K. L., Sigman, M. E., Forensic Comparative Glass Analysis by Laser-Induced Breakdown Spectroscopy. *Spectrochimica Acta Part B: Atomic Spectroscopy* **2007**.

76. Thornton, J. I., The Use of k-Values in the Interpretation of Glass Density and Refractive Index Data. *J. Forensic Sci.* **1989,** 34, 1323-1328.

77. Pitts, S. J., Kratochvil, B. J., Statistical Discrimination of Flat Glass Fragments by Instrumental Neutron Activation Analysis Methods for Forensic Science Applications. *J. Forensic Sci.* **1991,** 36, 122-135.

78. Parouchais, T., Warner, I. M., Palmer, L. T., Kobus, H., The Analysis of Small Glass Fragments Using Inductively Coupled Plasma Mass Spectrometry. *J. Forensic Sci.* **1996,** 41, 351-360.

79. Koons, R. D., Buscaglia, J., The Forensic Significance of Glass Composition and Refractive Index Measurements. *J. Forensic Sci.* **1999,** 44, (3), 496-503.

80. Montero, S., Hobbs, A. L., French, T. A., Almirall, J. R., Elemental analysis of glass fragments bt ICP-MS as evidence of association: analysis of a case. *J. Forensic Sci.* **2003,** 48, 1101-1107.

81. Collins, P., Coumbaros, J., Horsley, G., Lynch, B., Kirkbride, K. P., Skinner, W., Klass, G., Glass-containing gunshot residue particles: a new type of highly characteristic particle? *J. Forensic Sci.* **2003,** 48, (3), 1-16.

82. Trejos, T., Montero, S., Almirall, J. R., Analysis and comparison of glass fragments by laser ablation inductively coupled plasma mass spectrometry (LA-ICP-MS) and ICP-MS. *Anal. Bioanal. Chem.* **2003,** 376, 1255-1264.

83. Trejos, T., Almirall, J. R., Effect of Fractionation on the Forensic Elemental Analysis of glass Using Laser Ablation Inductively Coupled Plasma Mass Spectrometry. *Analytical Chemistry* **2004,** 76, 1236-1242.

84. Almirall, J. R., Umpierrez, S., Castro, W., Gornushkin, I., Winefordner, J., Forensic Elemental Analysis of Materical by Laser Induced Breakdown Spectroscopy (LIBS). *Sensors and Command, Control, Communications, and Intelligence (C3I) Technologies for Homeland Security and Homeland Defense IV; Carapezza, E. M. Ed. Proceedings of SPIE* **2006,** 5778, 657-666.

85. Nishiwaki, Y., Nakanishi, T., Tereda, Y., Ninomiya, T., Nakai, I., Nondestructive discrimination of small glass fragments for forensic examination using high energy synchrotron radiation x-ray fluorescence spectrometry. *X-Ray Spectrometry* **2006,** 35, (195-199).

86. Koons, R. D., Buscaglia, J., Bottrell, M., Miller, E. T., Forensic Glass Comparisons. In *Forensic Science Handbook*, 2nd ed.; Saferstein, R., Ed. Prentice Hall: Upper Saddle River, NJ, 2002; Vol. 1, pp 161-213.

87. Bridge, C. M., Powell, J., Steele, K. L., Williams, M., MacInnis, J. M., Sigman, M. E., Characterization of automobile float glass with laser-induced breakdown spectroscopy and laser ablation inductively coupled plasma mass spectrometry. *Appl. Spectros.* **2006,** 60, (10), 1181-1187.

88. Almirall, J. R., Trejos, T., Hobbs, A., Furton, K., Trace elemental analysis of glass and paint samples of forensic interest by ICP-MS using Laser Ablation solid sample introduction. *Sensors and Command, Control, Communications, and Intelligence (C3I) Technologies for Homeland Defense and Law Enforcement II, Carapezza, E. M. Ed. Proceedings of SPIE* **2003,** 5071, 193-204.

89. Hobbs, A. L., Almirall, J. R., Trace elemental analysis of automotive paints by laser ablation-inductively coupled plasma-mass spectrometry (LA-ICP-MS). *Anal. Bioanal. Chem.* **2003,** 376, 1265-1271.

90. Eller, A., Bertilsson, S., *Environmental Microbiology* **2004,** 6, (12), 1228-1243.

91. Portnov, A., Rosenwaks, S., Bar, I., Emission following laser-induced breakdown spectroscopy of organic compounds in ambient air. *Applied Optics* **2003,** 42, (15), 2835-2842.

92. Feroli, F., Puzinauskas, P. V., Laser-Induced Breakdown Spectroscopy for On-Line Engine Equivalence Ratio Measurements. *Appl. Spectros.* **2003,** 57, 1183-1189.

93. Boyain-Goitia, A. R., Beddows, D. C. S., Single Pollen Analysis by Laser-Induced Breakdown Spectroscopy. *Applied Optics* **2003,** 42, 6119-6132.

94. Német, B., Musiol, K., Sánta, I., Zachorowski, J., Time-resolved vibrational and rotational emission analysis of laser-produced plasma of carbon and polymers. *Journal of Molecular Structure* **1999,** 511-512, 259-270.

95. Seth, J., Padiyath, R., Babu, S. V., Optical emission from the laser-induced plasma during excimer laser etching of diamondlike carbon films. *Appl. Phys. Lett.* **1993,** 63, (2), 126-128.

96. Abdello-Messaci, S., Kerdja, T., Bendib, A., Malek, S., *Spectrochim. Acta* **2004,** 60B, 955-959.

97. Neogi, A., Narayanan, V., Thareja, R. K., Optical emission studies of laser ablation carbon plasma in a curve magnetic field. *Physics Letters A* **1999,** 258, 135-140.

98. Castillejo, M., Martín, M., de Nalda, R., Solís, J., Nanosecond versus picosecond near UV multiphoton dissociation of ketene. *J. Chem. Phys. Lett.* **1997,** 268, 465-470.

99. Acquaviva, S., Simualation of emission molecular spectra by a semi-automatic programme package: the case of C2 andcn diatomic molecules emitting during laser ablation of a graphite target in nitrogen environment. *Spectrochim. Acta Part A* **2004,** 60, 2079-2086.

100. Abdelli-Messaci, S., Kerdja, T., Bendib, A., Malek, S., Emission study of C_2 and CN in laser-created carbon plasma under nitrogen environment. *J. Phys. D: Appl. Phys.* **2002,** 35, 2772-2778.

101. Harilal, S. S., Issac, R. C., Bindhu, C. V., Nampoori, V. P. N., Vallabhan, C. P. G., Optical emission studies of C_2 species in laser-produced plasma from carbon. *J. Phys. D: Appl. Phys.* **1997,** 30, 1703-1709.

102. Kokai, F., Koga, Y, Time-of-flight mass spectrometric studies on the plume dynamics of laser ablation of graphite. *Nuclear Instruments and Methods in Physics Research B* **1997,** 121, 387-391.

103. Knowles, P. J., Werner H-J., Hay P. J., Cartwright, D. C., The $A^2\Pi$-$X^2\Sigma^+$ red and $B^2\Sigma$-$X^2\Sigma^+$ violet systems of the CN radical: Accurate multireference configuration interaction calculations of the radiative transition probabilities. *J. Chem. Phys.* **1988,** 89, (12), 7334 - 7343.

104. Li, L., Xiang, W., Stupp, S. I., Three-photon induced ultraviolet emissions from polymers. *J. Phys. D: Appl. Phys.* **2002,** 35, 451-453.

105. Silverstein, R. M., Webster, F. X., Kiemle, D., *Spectrometric Identification of Organic Compounds*. 7 ed.; John Wiley & Sons, Inc.: Hoboken, NJ, 2005.

106. Noda, I., Ozaki, Y., *Two-Dimensional Correlation Spectroscopy: Applications in Vibrational and Optical Spectroscopy*. John Wiley & Sons, Ltd: Hoboken, NJ, 2004.

107. Noda, I., Dowrey, A. E., Marcorr, C., Story, G. M., Ozaki, Y., Generalized Two-Dimensional Correlation spectroscopy. *Applied Spectroscopy* **2000,** 54, (7), 236A-248A.

108. López-Moreno, C., Palance, S., Laserna, J. J., DeLucia Jr., F., Miziolek, A. W., Rose, J. Walters, R. A., Whitehouse, A. I., Test of a stand-off laser-induced breakdown spectroscopy sensor for the detection of explosive residues on solid surfaces. *J. Anal. At. Spectrom.* **2006,** 21, 55-60.

109. Gottfried, J. L., De Lucia Jr., F. C., Harmon, R. S., Munson, C. A., Winkel Jr., R. J., Miziolek, A. W. *Detection of Energetic Materials and Explosive Residues with Laser-Induced Breakdown Spectroscopy: I. Laboratory Measurements*; Army Research Laboratory: Aberdeen Proving Ground, 2007.

110. Harmon, R. S., DeLucia Jr., F. C., Lapointe, A., Winkel Jr., R. J., Miziolek, A. W., LIBS for landmine detection and discrimination. *Anal. Bioanal. Chem.* **2006,** 385, 1140-1148.

111. DeLucia Jr., F. C., Samuels, A. C., Harmon, R. S., Walters, R. A., McNesby, K. L., LaPointe, A., Winkel, R. J., Miziolek, A. W., Laser-Induced Breakdown Spectroscopy (LIBS): A Promising Versatile Chemical Sensor Technology for Hazardous Material Detection. *IEEE Sensors J* **2005,** 5, 681-689.

112. Sakamoto, T., Matsuura, H., Akatsuka, H., Spectroscopic Study on Vibrational Distribution of N_2 $C^3\Pi$ and $B^3\Pi$ States in Microwave Nitrogen Discharge. *Japanese Journal of Applied Physics* **2006,** 45, (10A), 7905-7910.

113. Wagatsuma, K., Hirokawa, K., Characterization of Atomic Emission Lines from Argon, Neon, and Nitrogen Glow Discharge Plasmas. *Anal. Chem.* **1985,** 57, 2901-2907.

114. Kuzuya, M., Matsumoto, H., Takechi, H., Mikami, O., Effect of Laser Energy and Atmosphere on the Emission Characteristics of Laser-Induced Plasmas. *Applied Spectroscopy* **1993,** 47, (10), 1659-1664.

115. Thornton, J. I., Crim, D., Forensic Paint Examination. In *Forensic Science Handbook*, 2nd ed.; Saferstein, R., Ed. Prentice Hall: Upper Saddle River, NJ, 2002; Vol. 1, pp 427-478.

116. Ryland, S. G., Infrared Microspectroscopy of Forensic Paint Evidence. In *Practical Guide to Infrared Microspectroscopy*, Humecki, H. J., Ed. Marcel Dekker, Inc.: New York, 1995; Vol. 19, pp 163-243.

117. Ryland, S., Bishea, G., Brun-Conti, L., Eyring, M., Flanagan, B., Jergovich, T., MacDougall, D., Suzuki, E., Discrimination of 1990s original automotive paint systems: a collaborative study of black nonmetallic base coat/clear coat finishes using infrared spectrscopy. *Journal of Forensic Sciences* **2001,** 46, 31-45.

118. Buckle, J. L., MacDougall, D. A., Grant, R. R., PDQ - Paint Data Queries: The History and Technology behind the Development of the Royal Canadian Mounted Police Forensic Laboratory Services Automotive. *Canadian Society of Forensic Science* **1997,** 30.

119. Zarei, R., Arab, S., Sadeghi, M., A method for protein accessibility prediction based on residue types and conformational states. *Computational Biology and Chemistry* **2007,** 31, 384-388.